

# TECHNISCHE UNIVERSITÄT MÜNCHEN

Lehrstuhl für Statik

## A General Approach for Solving Inverse Problems in Geophysical Systems by Applying Finite Element Method and Metamodel Techniques

Hao Zhang

Vollständiger Abdruck der von der Ingenieur fakultät Bau Geo Umwelt der Technischen  
Universität München zur Erlangung des akademischen Grades eines

Doktor-Ingenieurs (Dr.-Ing.)

genehmigten Dissertation.

Vorsitzender: Univ.-Prof. Dr.-Ing. habil. Fabian Duddeck

Prüfer der Dissertation: 1. Univ.- Prof. Dr.-Ing. Kai-Uwe Bletzinger

2. Ass. Prof. Rocco Malservisi, Ph.D.  
University of South Florida, USA

Die Dissertation wurde am 19.01.2016 bei der Technischen Universität München  
eingereicht und durch die Ingenieur fakultät Bau Geo Umwelt am  
20.04.2016 angenommen.



## Abstract

The inverse problem also known as parameters estimation or parameters identification is a common but very important task in the world of science and engineering. Its applications can be found in many different fields such as geoscience, nondestructive material testing, aerodynamics, etc. Solving an inverse problem means to find a proper set of parameters of a model, to be well fitted, to a given data set. It can be quite tough and time-consuming if the model is complex and contains many parameters, especially when the relationships among the parameters are highly nonlinear. This research work is therefore dedicated to a general approach of efficiently solving inverse problems in complex systems by applying finite element method together with metamodel techniques. The approach is suitable for applications in the field of geoscience and remote sensing engineering.

In recent decades, thanks to the rapid development of geodetic techniques such as GPS and InSAR, the number of observations of ground deformation in volcanic areas increased drastically. The improvement of these datasets, both in term of spatial and temporal distribution, higher resolution and better accuracy, provides invaluable observations of the surface deformation that can be used to better understand volcanic processes and possibly improve our ability of forecasting the behavior and the hazards associated with a given volcano.

Usually, volcano deformation is modeled using simple analytical solutions. In reality, the complexity of volcanic areas, is highly oversimplified by these models, and the estimated sources of deformation could be significantly biased. The use of more complex models, as finite element method, allows a more realistic representation of the complex geophysical system and a more reliable simulation of a volcanic system more compatible with the improved observations. However, finite element models usually take long time to run and are not directly suitable to traditional inversion schemes.

During the parameter identification phase, solving the inverse problems requires running the underlying model a significant number of times. The long time needed to run finite element models makes this approach inefficient. To overcome this issue, the direct approach is modified by introducing the idea of metamodel.

A metamodel is a mathematical approximation of the underlying system, which is very efficient in computation and keeps relatively good accuracy compared to the original model. With the self-updating procedure, metamodels can greatly reduce the number of model runs needed for the parameter estimation. In this way, the efficiency of the optimization process is significantly improved.

The effectiveness and efficiency of the presented metamodel-based inversion approach has been verified by inverting synthetic examples and with the real case application to the deformation of the Long Valley Caldera, CA, USA.



# Zusammenfassung

Das Inverse Problem auch bekannt als Parameterschätzung oder Parameteridentifikation, ist eine übliche, aber sehr wichtige Aufgabe in der Welt der Wissenschaft und Technik. Die Anwendung des Inversen Problems kann man in vielen verschiedenen Bereichen vorfinden, wie z.B. in der Geowissenschaft, in der zerstörungsfreien Prüfung, in der Aerodynamik, usw. Ein Inverses Problem zu lösen, heißt einen richtigen Parametersatz eines Modells, das gut zu einem gegebenen Datensatz passt, zu finden. Es kann ziemlich schwierig und zeitaufwändig sein, wenn das Modell komplex ist und viele Parameter besitzt, vor allem wenn die Beziehung zwischen den Parametern stark nichtlinear ist. In dieser Dissertation wurde eine allgemeine Methode zur effizienten Lösung von Inversen Problemen in komplexen Systemen mit Hilfe der Finite-Elemente-Methode und der Metamodelltechnik entwickelt. Diese Methode wurde in der Geowissenschaft und in den Fernerkundungstechniken erprobt.

In den letzten Jahrzehnten hat man durch die schnelle Entwicklung der Fernerkundungstechniken, wie z.B. GPS und InSAR immer leichteren Zugang zu Beobachtungsdaten mit hoher Auflösung und Genauigkeit von Oberflächenverformungen in vulkanischen Gebieten.

Die Finite-Elemente-Methode, die eine der wichtigsten Werkzeuge der Computersimulation ist, liefert die Möglichkeit realistischer und anspruchsvollere numerische Modelle von komplexen geophysischen Systemen zu etablieren. Diese Modelle passen zuverlässiger zu den Beobachtungsdaten als einfache analytische Modelle. Die Finite-Elemente-Modelle benötigen jedoch mehr Zeit, um Ergebnisse zu liefern.

Da das Lösen von Inversen Problemen für gewöhnlich ein Optimierungsprozess ist, scheint das Finite-Elemente-Modell während der Parameteridentifizierungsphase ineffizient zu sein, um als Verformungsmodell zu dienen, weil es mehrmals durchgeführt werden müsste, um den passendsten Parametersatz zu finden. Um das Effizienzproblem zu lösen, wurde die direkte Methode durch die Einführung der Metamodelltechnik modifiziert.

Ein Metamodell ist eine mathematische Annäherung des vorliegenden Systems, das bei der Berechnung sehr effizient und im Vergleich zum Originalmodell relativ genau ist. Die selbstständige Aktualisierung des Metamodells bewirkt, dass die benötigte Anzahl der Durchläufe bei der Anwendung des Finite-Elemente-Modells stark reduziert wird. Auf diese Weise, wird die Gesamtberechnungszeit signifikant reduziert und die Effizienz des Optimierungsprozesses wird verbessert.

Der Erfolg und die Effizienz der vorgestellten metamodell-basierten Inversionsmethode wurde sowohl in synthetischen Testbeispielen als auch in einem realen Fall am Beispiel des Long Valley Caldera in Kalifornien überprüft.



# Table of Contents

<b>Abstract .....</b>	<b>I</b>
<b>Zusammenfassung .....</b>	<b>III</b>
<b>List of Figures .....</b>	<b>VII</b>
<b>List of Tables .....</b>	<b>XI</b>
<b>Chapter 1 Introduction.....</b>	<b>1</b>
1.1 Motivation.....	1
1.2 Goal of the work .....	3
1.3 Flowchart of the proposed approach.....	3
1.4 Structure of this thesis.....	5
<b>Chapter 2 Theoretical Background and the Inverse Problem .....</b>	<b>7</b>
2.1 The typical inverse problem .....	7
2.2 Inverse problems in geoscience .....	14
<b>Chapter 3 Data Acquisition and Selection .....</b>	<b>19</b>
3.1 Data acquisition techniques .....	19
3.1.1 <i>The Global Positioning System (GPS)</i> .....	19
3.1.2 <i>Interferometric Synthetic Aperture Radar (InSAR)</i> .....	21
3.2 Data selection.....	24
3.2.1 <i>The typical genetic algorithm</i> .....	24
3.2.2 <i>Combination genetic algorithm (CGA)</i> .....	31
3.2.3 <i>Weighted uniformly selection of Investigation points (IPs)</i> .....	38
<b>Chapter 4 Analytical Geophysical Models.....</b>	<b>43</b>
4.1 Volcano deformation source models .....	43
4.1.1 <i>Structure of Earth's interior</i> .....	43
4.1.2 <i>Elastic half-space</i> .....	44
4.1.3 <i>Spherical and spheroidal sources</i> .....	45

4.1.4	<i>Dipping point and finite rectangular tension cracks</i> .....	52
4.1.5	<i>Tradeoff between parameters</i> .....	58
<b>Chapter 5</b>	<b>Metamodels Substituting Computer Simulations</b> .....	<b>69</b>
5.1	Design of Experiments (DoE) .....	70
5.1.1	<i>Space-filling Latin Hypercube Designs (LHD)</i> .....	75
5.2	Metamodels .....	78
5.2.1	<i>Response surface models</i> .....	78
5.2.2	<i>Kriging model</i> .....	80
5.3	Update procedures to improve quality of the metamodel .....	82
<b>Chapter 6</b>	<b>Application Examples</b> .....	<b>85</b>
6.1	Synthetic examples .....	85
6.1.1	<i>FE model without topography</i> .....	85
6.1.2	<i>FE model with topography of caldera</i> .....	92
6.2	Long Valley Caldera in California .....	95
6.2.1	<i>Geological background</i> .....	96
6.2.2	<i>Metamodel based inversion</i> .....	97
<b>Chapter 7</b>	<b>Conclusions and Outlook</b> .....	<b>103</b>
7.1	Conclusions .....	103
7.2	Future work .....	104
<b>Appendix 1.</b>	<b>Further corrections to Yang et al. (1988)</b> .....	<b>105</b>
<b>Bibliography</b>	.....	<b>107</b>
<b>Acknowledgements</b>	.....	<b>119</b>
<b>Curriculum Vitae</b>	.....	<b>121</b>



# List of Figures

FIGURE 1.1	GENERAL FRAMEWORK OF PROPOSED METAMODEL-BASED APPROACH FOR SOLVING INVERSE PROBLEMS. ...	4
FIGURE 2.1	OBSERVED DATA AND TRAJECTORY OF THE BOMB EXAMPLE. ....	10
FIGURE 2.2	SEISMIC METHOD OF PROSPECTING FOR OIL AND GAS, CC-BY-SA-NC. ....	17
FIGURE 3.1	DIFFERENTIAL INTERFEROGRAM OF THE TEST SITE CENTERED AT THE CONVENTION CENTER IN LAS VEGAS (ZHU AND BAMLER 2011). IT CAN BE SEEN THAT THERE ARE MANY FRINGES IN THE FIGURE. EACH COMPLETE INTERFERENCE FRINGE IS SHOWN AS A SPECTRUM OF COLORS FROM VIOLET TO GREEN TO RED IN THE INTERFEROGRAM. EACH FRINGE RESULTS FROM A HALF-WAVELENGTH $\lambda/2$ RANGE CHANGE (I.E. THE SURFACE DISPLACEMENT) OCCURRED BETWEEN TWO IMAGE ACQUISITIONS. SO THE INTERFEROGRAM SHOWN HERE IS SIMILAR TO A DEFORMATION MAP WITH CONTOUR LINES. WE CAN GET THE TOTAL AMOUNT OF SURFACE DEFORMATION BY COUNTING THE NUMBER OF COMPLETE FRINGES. IN OUR CASE, SINCE THE WAVELENGTH OF THE INSAR WE USE IS 3.11 CM, EACH FRINGE CORRESPONDS TO A RANGE CHANGE OF $\lambda/2 = 1.55$ CM, WHICH IS QUITE A HIGH RESOLUTION. ....	23
FIGURE 3.2	ENCODING OF SINGLE POINT BINARY CROSSOVER. ....	29
FIGURE 3.3	ENCODING OF TWO POINTS BINARY CROSSOVER. ....	30
FIGURE 3.4	ENCODING OF UNIFORM BINARY CROSSOVER. ....	30
FIGURE 3.5	ENCODING OF ARITHMETIC BINARY CROSSOVER. ....	31
FIGURE 3.6	ENCODING OF BINARY MUTATION. ....	31
FIGURE 3.7	REPRESENTATION OF INDIVIDUALS IN BINARY FORM. ....	32
FIGURE 3.8	SIMPLE BINARY CROSSOVER FOR THE COMBINATION PROBLEM. ....	33
FIGURE 3.9	BINARY MUTATION FOR THE COMBINATION PROBLEM. ....	34
FIGURE 3.10	COMBINATION ENCODING OF SIMPLE CROSSOVER. ....	35
FIGURE 3.11	COMBINATION ENCODING OF TWO POINTS CROSSOVER. ....	36
FIGURE 3.12	COMBINATION ENCODING OF MIXING CROSSOVER. ....	37
FIGURE 3.13	COMBINATION ENCODING OF MUTATION. ....	37
FIGURE 3.14	THE WHOLE SET OF OBSERVATION DATA POINTS OF THE SYNTHETIC EXAMPLE. ....	40
FIGURE 3.15	THE CALCULATED WEIGHTS FOR EACH DATA POINTS OF THE SYNTHETIC EXAMPLE. ....	40
FIGURE 3.16	WEIGHTED UNIFORMLY SELECTED INVESTIGATION POINTS (BLUE CIRCLES) IN THE WHOLE SET OF DATA POINTS. ....	41

FIGURE 3.17	UNIFORMLY SELECTED INVESTIGATION POINTS (RED CIRCLES) WITHOUT CONSIDERING WEIGHTS IN THE WHOLE SET OF DATA POINTS.....	42
FIGURE 4.1	COORDINATE SYSTEM AND PARAMETER DEFINITION OF POINT PRESSURE SOURCE. (MOGI 1958).....	45
FIGURE 4.2	PROFILES OF NORMALIZED AXISYMMETRIC HORIZONTAL (RED) AND VERTICAL (BLUE) DISPLACEMENTS GENERATED BY MOGI AND MCTIGUE SOURCE. ....	47
FIGURE 4.3	COORDINATE SYSTEM AND PARAMETER DEFINITION OF YANG'S MODEL. (YANG ET AL. 1988).....	48
FIGURE 4.4	NORMALIZED SURFACE DISPLACEMENT FIELDS GENERATED BY THE YANG'S MODEL. (A). HORIZONTAL DISPLACEMENT; (B). VERTICAL DISPLACEMENT. ....	49
FIGURE 4.5	COORDINATE SYSTEM AND PARAMETER DEFINITION OF CIGAR-SHAPED SOURCE MODEL (DZURISIN 2007)	50
FIGURE 4.6	NORMALIZED SURFACE DISPLACEMENTS GENERATED BY A CLOSED PIPE MODEL WITH DIFFERENT POISSON'S RATIO. ....	51
FIGURE 4.7	CROSS-SECTIONAL VIEW OF SILLS AND DIKES. (PRESS AND SIEVER 1994).....	52
FIGURE 4.8	PARAMETER DEFINITION AND LOCAL COORDINATE SYSTEM OF DIPPING POINT AND FINITE RECTANGULAR TENSILE FAULTS. (OKADA 1992).....	53
FIGURE 4.9	NORMALIZED SURFACE DISPLACEMENT FIELDS GENERATED BY A POINT TENSILE CRACK. (A). SURFACE DISPLACEMENTS ALONG THE CRACK; (B). SURFACE DISPLACEMENTS ACROSS THE CRACK. ....	54
FIGURE 4.10	2D NORMALIZED SURFACE DEFORMATION OF OKADA MODEL INDUCED BY A POINT TENSILE CRACK WITH DIPPING ANGLE $\delta = 90^\circ$ .....	55
FIGURE 4.11	NORMALIZED SURFACE DISPLACEMENT FIELDS GENERATED BY A FINITE RECTANGULAR TENSILE CRACK. (A). SURFACE DISPLACEMENTS ALONG THE CRACK; (B). SURFACE DISPLACEMENTS ACROSS THE CRACK.....	57
FIGURE 4.12	2D NORMALIZED SURFACE DEFORMATION INDUCED BY A FINITE RECTANGULAR TENSILE CRACK WITH DIPPING ANGLE $\delta = 90^\circ$ .....	58
FIGURE 4.13	$\chi^2$ PLOT FOR THE GRID SEARCH OF PARAMETER $x_0$ AND $y_0$ .....	59
FIGURE 4.14	$\chi^2$ PLOT AND CONTOUR PLOT FOR THE GRID SEARCH OF PARAMETER $d$ AND $S$ (WITH A CONTOUR INTERVAL OF 2.1). ....	60
FIGURE 4.15	SURFACE DEFORMATIONS PRODUCED BY DIFFERENT PARAMETER SETTINGS A (LEFT) AND B (RIGHT). ...	60
FIGURE 4.16	(A)-(T) CONTOUR PLOT OF $\chi^2$ FOR THE GRID SEARCHES BETWEEN PARAMETERS OF THE YANG'S MODEL. THE PINK STAR INDICATES THE MINIMUM OF $\chi^2$ , I.E. THE $\chi^2$ OF THE REFERENCE MODEL. THE CONTOUR INTERVAL IS SET TO 1/400 OF THE MAXIMUM OF EACH PANEL IN ORDER TO SHOW THE PATTERN MORE CLEARLY. ....	64
FIGURE 4.17	(A)-(T) CONTOUR PLOT OF $\chi^2$ FOR GRID SEARCHES BETWEEN PARAMETERS OF THE OKADA MODEL. THE PINK STAR INDICATES THE MINIMUM OF $\chi^2$ , I.E. THE $\chi^2$ OF THE REFERENCE MODEL. THE CONTOUR INTERVAL IS SET TO 1/400 OF THE MAXIMUM OF EACH PANEL IN ORDER TO SHOW THE PATTERN MORE CLEARLY. ....	68
FIGURE 5.1	EXAMPLES OF FACTORIAL DESIGNS.....	72
FIGURE 5.2	EXAMPLE OF CENTRAL COMPOSITE DESIGN. ....	72

FIGURE 5.3	LATIN HYPERCUBE DESIGN FOR $K=5$ AND $N=2$ .	74
FIGURE 5.4	LATIN HYPERCUBE DESIGN FOR $K=5$ AND $N=3$ .	75
FIGURE 5.5	COMPARISON OF (A) RANDOM LHD TO (B) SPACE-FILLING LHD.	76
FIGURE 6.1	(A) THE SETUP OF THE FE MODEL FOR THE SPHERICAL SOURCE CASE. (B) THE SETUP OF FE MODEL FOR THE PROLATE SPHEROIDAL SOURCE CASE.	86
FIGURE 6.2	(A) SYNTHETIC OBSERVED VERTICAL SURFACE DEFORMATION. (B) NODAL RESULTS OF OBSERVED VERTICAL SURFACE DEFORMATION (DOTS) AND THE SELECTED IPS (BLUE CIRCLES) FOR 4 PARAMETERS SPHERICAL SOURCE.	87
FIGURE 6.3	(A) SYNTHETIC OBSERVED VERTICAL SURFACE DEFORMATION. (B) NODAL RESULTS OF THE OBSERVED VERTICAL SURFACE DEFORMATION (DOTS) AND THE SELECTED IPS (BLUE CIRCLES) FOR 8 PARAMETERS YANG'S MODEL.	88
FIGURE 6.4	(A) THE SYNTHETIC OBSERVATION DATA USED FOR THE SPHERICAL SOURCE CASE. (B) THE VERTICAL SURFACE DEFORMATION GENERATED BY THE FE MODEL WITH THE INVERSED PARAMETERS. (C) (D) ABSOLUTE AND RELATIVE RESIDUAL VERTICAL SURFACE DEFORMATION.	91
FIGURE 6.5	(A) THE SYNTHETIC OBSERVATION DATA USED FOR THE SPHEROIDAL SOURCE CASE. (B) THE VERTICAL SURFACE DEFORMATION GENERATED BY THE FE MODEL WITH THE INVERSED PARAMETERS. (C) (D) ABSOLUTE AND RELATIVE RESIDUAL VERTICAL SURFACE DEFORMATION.	92
FIGURE 6.6	SETUP OF THE FE MODEL WITH TOPOGRAPHY OF CALDERA.	93
FIGURE 6.7	(A) SYNTHETIC OBSERVED VERTICAL SURFACE DEFORMATION. (B) NODAL RESULTS OF THE OBSERVED VERTICAL SURFACE DEFORMATION (DOTS) AND THE SELECTED IPS (BLUE CIRCLES) FOR 4D SPHERICAL SOURCE.	94
FIGURE 6.8	(A) THE SYNTHETIC OBSERVATION DATA WITH TOPOGRAPHY OF CALDERA USED FOR THE SPHERICAL SOURCE CASE. (B) THE VERTICAL SURFACE DEFORMATION GENERATED BY THE FE MODEL WITH THE INVERSED PARAMETERS. (C) (D) ABSOLUTE AND RELATIVE RESIDUAL VERTICAL SURFACE DEFORMATION.	95
FIGURE 6.9	MAP OF LONG VALLEY CALDERA, EASTERN CALIFORNIA. (SECCIA ET AL. 2011)	96
FIGURE 6.10	CONTINUOUS GPS NETWORK IN AND NEAR THE LONG VALLEY CALDERA.	97
FIGURE 6.11	SETUP OF THE FE MODEL.	98
FIGURE 6.12	OBSERVED HORIZONTAL (LEFT) AND VERTICAL (RIGHT) DEFORMATION USED IN INVERSION. ELLIPSES AND BARS REPRESENT 95% CONFIDENCE ERROR.	98
FIGURE 6.13	OBSERVED (BLACK ARROWS) AND BEST FIT MODEL PREDICTED (RED ARROWS) (A) HORIZONTAL AND (B) VERTICAL SURFACE DEFORMATION. (C) (D) HORIZONTAL AND VERTICAL RESIDUALS OF THE BEST FIT MODEL.	100
FIGURE 6.14	(A) OBSERVED VERTICAL DEFORMATION ACQUIRED BY INSAR TECHNIQUE (UNWRAPPED). (B) WEIGHTED UNIFORMLY SELECTED INVESTIGATION POINTS (IPS).	100
FIGURE 6.15	(A) VERTICAL SURFACE DEFORMATION GENERATED BY THE FE MODEL WITH THE INVERSED PARAMETERS. (B) (C) ABSOLUTE AND RELATIVE RESIDUAL VERTICAL SURFACE DEFORMATION.	102



# List of Tables

TABLE 4-1 RANGE OF ALL THE PARAMETERS OF YANG'S MODEL USED IN THE GRID SEARCH. ....61

TABLE 4-2 RANGE OF ALL THE PARAMETERS OF OKADA MODEL USED IN THE GRID SEARCH. ....65

TABLE 6-1 PARAMETERS USED TO GENERATE THE SYNTHETIC SURFACE DEFORMATION DATA.....87

TABLE 6-2 SOURCE PARAMETERS AND THEIR RANGE.....89

TABLE 6-3 RESULTS OF INVERSED SOURCE PARAMETERS.....90

TABLE 6-4 PARAMETERS USED TO GENERATE THE SYNTHETIC SURFACE DEFORMATION DATA.....94

TABLE 6-5 RESULTS OF INVERSED SOURCE PARAMETERS.....94

TABLE 6-6 SOURCE PARAMETERS AND THEIR RANGE.....99

TABLE 6-7 RESULTS OF INVERSED SOURCE PARAMETERS BASED ON GPS DATA.....99

TABLE 6-8 RESULTS OF INVERSED SOURCE PARAMETERS BASED ON INSAR DATA..... 101



# Chapter 1

## Introduction

---

### 1.1 Motivation

A typical problem in scientific and engineering studies is the search of the best model that can explain a set of observations. In general, scientists and engineers have background knowledge of the process or system they want to study that can be expressed in some mathematic form such as ordinary differential equation (ODE), partial differential equation (PDE), and linear or nonlinear algebraic equations. While the mathematical formulation of the process controlling the observations is often well described, the key parameters governing the behavior of the system are generally unknown and need to be estimated. If we assume the underlying mechanism of the system is well understood, then, feeding the parameters to these mathematical models will provide some response that indicate the sensitivity of the system to those parameters. This way of analyze the problem is often referred as forward problem. Dealing with a forward problem may include solving analytically an ODE, PDE or a set of linear equations, or solving it approximately through the application of numerical algorithms. Still, the parameters controlling the system are fed to the solution and the response to the given parameters is analyzed independently by possible observations of the system. On the contrary, it is possible to focus on searching for the physical parameters that best represent some observation of the system behavior. Such kind of problem is called inverse problem. It was suggested by many famous scientists (e.g. Lagrange, Poisson, Galileo, etc.) and firstly formalized in a mathematical sense in 1929 by the Soviet-Armenian physicist, Viktor Hambardzumyan.

The inverse problem, also known as parameters estimation or parameters identification, is quite common and can be found in a variety of different fields, such as geoscience, computer vision, nondestructive testing, ocean acoustic tomography, aerodynamics, and rocketry, etc. It often allows to estimate physical parameters we are interested in but that are either impossible or too difficult to measure or observe directly. Let's take the nondestructive ultrasonic testing technique as an example. We can measure the reflected and refracted ultrasonic waves, however, the parameters we actually want to know are the location and size of possible cracks within a material. Inversion theory allows us to link the propagation of the ultrasonic waves to the location of internal cracks, thus identifying the possible failure point within the material without having to open it.

The inverse problem is typically ill-posed, meaning that due to its definition, mathe-

mathematical formulation, or limited set of observations the model parameters or the material properties are not univocally derived. The term "ill-posed" used here refers to the definition given by the French mathematician Jacques Hadamard (1902). To solve the inverse problem, many different methods have been developed. For simple linear inverse problems, often it is possible to solve the inversion problem analytically by directly inverting the observation matrix. However, in most cases such solution does not exist or, as in the case of a nonlinear inverse problem, is too complex. In those cases different optimization methods have to be applied (Aster et al. 2005).

In recent decades, the rapid developments of computer science and technology allows the use of computer simulations as a way to model the behavior of a simplified representation of complex physical systems in many different industries and scientific fields. While the widespread and commonly-used pure analytical models are forced to introduce significant simplifications, numerical computer simulations offer the possibility to consider more complicated factors such as time-dependent material behavior, real topography, real time temperature fields, as well as the heterogeneity of internal structures. Thus, despite also the numerical models are still only approximations of the real systems and still need to rely on a lot of assumptions and simplifications, computer simulations allow a better understanding of the characteristics of realistic physical systems. The finite element method is one of the powerful computer simulation tools, which has been widely used by scientists and engineers community since 1980s and is getting more and more popular with improving computers.

In spite of the advantages mentioned above, computer simulations have their own drawbacks. In particular, the increasing complexity of the studied problems, significantly increases the computational cost of the simulations. Although computer power is increased significantly in recent times, one single run of computer simulation may take significant time, from minutes to several hours (even days) to provide a result. The complexity of problems, the efficiency of algorithms, or different hardware, can significantly impact the running time. For optimization procedures, where a huge number of alternative designs have to be investigated and simulations need to be performed multiple times, can be significantly affected by the model performance. In other words, optimization with computer simulations is commonly a time-consuming task and improvement in the used algorithm can transform an impossibly long task in a powerful tool.

In this work, a metamodel-based approach is used to minimize the computational cost in computer simulation aided inverse problems. The metamodel is a mathematical approximation of the underlying computer simulation. In comparison with the original model, it is generally very efficient in computation and keeps relatively good accuracy. The metamodel can greatly reduce the needed number of runs of the computer simulation (e.g. finite element model), and in this way improve the optimization process significantly reducing the total computing time.

The range of possible applications for the presented approach is very broad, including mechanical engineering, electronic engineering, civil engineering, bio-medical engineering, material science, signal processing, metal forming, geosciences, etc. This work keeps its focus on solving practical inverse problems in geoscience and remote sensing engineering



and its application in hazards assessment in volcanic areas.

## **1.2 Goal of the work**

The main goal of the present work can be summarized as below:

- To develop a general, effective and economic approach for solving inverse problems by combining the metamodel technique together with the finite element technique. The proposed approach should be particularly suitable for geoscience applications.
- To evaluate and validate the performance and reliability of the proposed approach by means of numerical tests and real case studies.
- To obtain better understanding of the underlying mechanism behind the geodynamic processes such as earthquakes, volcanic eruptions, and ground subsidence. And to establish better and more realistic geophysical models so that we can provide more valuable and convincing information for related natural hazard assessments.

## **1.3 Flowchart of the proposed approach**

The flowchart illustrating the general framework of the proposed metamodel-based approach is shown in Figure 1.1. The whole approach consists of three main parts. The first part is about how to treat the observation data. The second part is regarding how to choose a suitable parameterized model candidate according to the specific problem under study. And the third part is the core part of the proposed approach, which is an optimization procedure based on finite-element-aided self-updating metamodels.

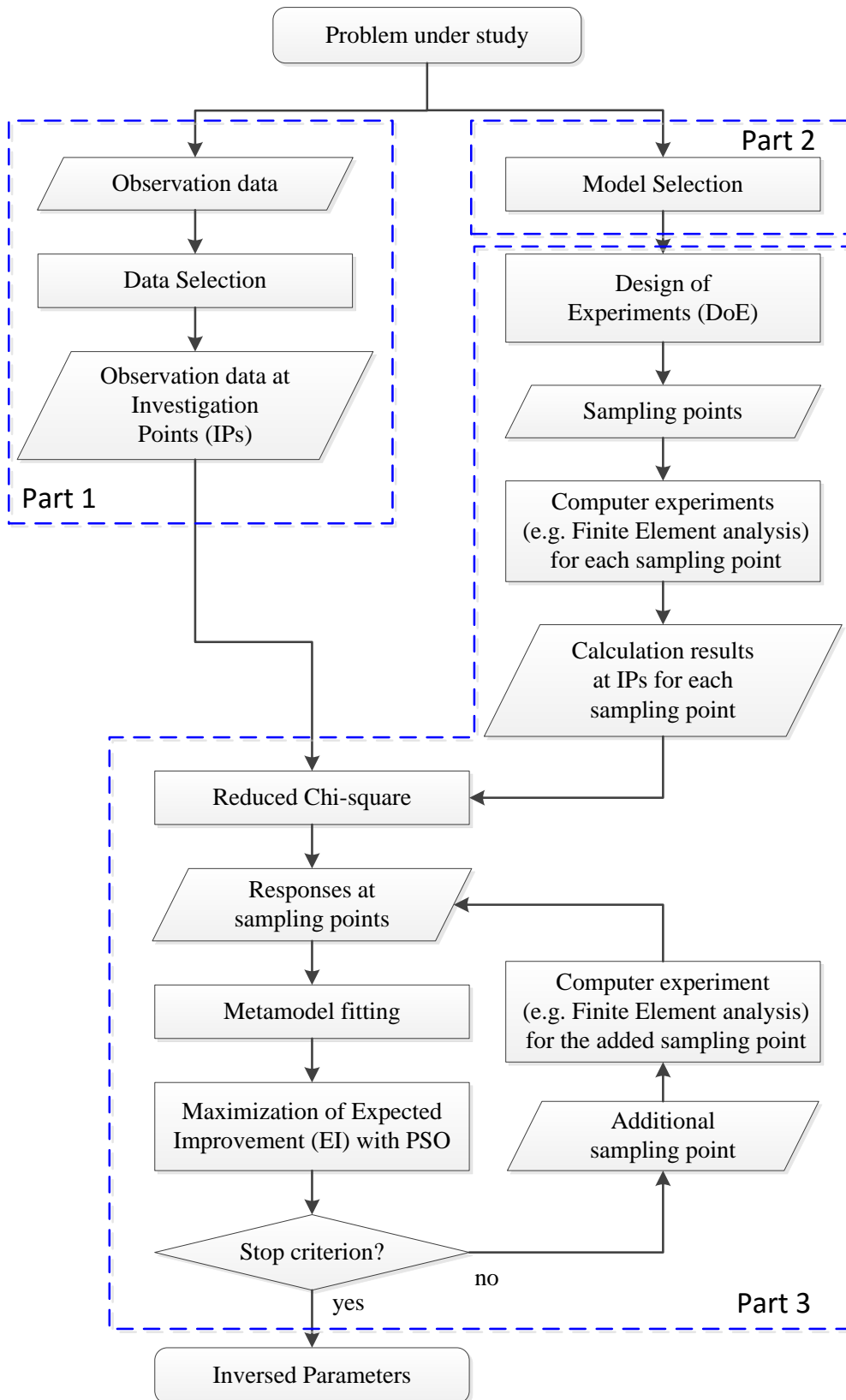


Figure 1.1 General framework of proposed metamodel-based approach for solving inverse problems.

## 1.4 Structure of this thesis

After this introductory chapter including the motivation and goal of the research, the rest of this thesis is organized as follows.

Chapter 2 provides an overview of the concept of inverse problem. It includes a short introduction to the definitions and terms used in the field of inverse problems. Then based on the mathematical formulations, the characteristics of typical inverse problems and related solution techniques are presented and discussed. Subsequently, a further discussion about inverse problems in the context of geosciences applications is presented. It focuses on the issues and difficulties of inverse problems related to the special conditions and requirements of geosciences. In addition, the theoretical and methodological fundamentals used for the work in this dissertation are also presented.

The modern techniques used in geodesy and remote sensing for acquiring observation data are generally introduced in Chapter 3. Among all the current geodetic techniques, two of the most commonly used tools are presented and discussed in more detail: Global Navigation Satellite System (in particular the Global Positioning System, GPS for short), and the interferometric synthetic aperture radar, normally abbreviated as InSAR. It is worth to mention that all the observed and measured data used in this work are obtained using these two techniques. In general, InSAR provides such large amount of observed data that would not be practical to invert. A weighted uniformly data selection approach based on the Combination Genetic Algorithm (CGA) is elaborated to smartly select a part of the data from the whole dataset without losing its overall characteristics. The selected data points are termed as Investigation Points (IPs) in this thesis.

The fourth chapter provides an overview of the analytical geophysical models used for describing volcanos. The commonly used volcano deformation source models including Mogi model, finite spherical source, prolate spheroidal source, dipping point and finite rectangular tension cracks are described. Further discussions include the problem of topographical effects on those models and tradeoff between different parameters.

The metamodel techniques are covered in Chapter 5. It starts with a general review of the basic concepts of metamodels. To create a metamodel, a set of training data needs to be collected from so called sampling points. The methods for getting these sampling points are known as "design of experiments (DoE)". Different layouts of DoE can significantly influence the predictive behavior and overall performance of metamodels, thus a detailed discussion of different DoE methods is given in this chapter. Thereafter, two types of commonly used metamodels are described in detail: the response surface model, and the Kriging model. Following, an approach for updating metamodels iteratively during the optimization process is presented. With this approach, the quality of the metamodel can be improved in an iterative way, ensuring the good performance of the metamodel-based approach for solving inverse problems.

In Chapter 6, the performance of proposed metamodel-based approach is tested applying the method to real life examples. Synthetic examples are studied to prove the usability

and reliability of the approach. An application to real data from Long Valley caldera, CA, USA will conclude the chapter.

The final chapter of this dissertation summarizes the main achievements of the current work, followed by an outlook about several topics for future research.

## Chapter 2

### Theoretical Background and the Inverse Problem

---

This chapter first reviews the theoretical background and basic concepts relating to inverse problems. Then it keeps the focus more specifically on the inverse problems and related applications emerged in the field of geoscience. In addition, relevant publications on this topic are also reviewed.

#### 2.1 The typical inverse problem

Mechanical and physical systems can often be represented in a mathematical formulation through the introduction of a generic operator  $G(\mathbf{m})$  ( $G$  also called forward operator) controlled by parameters described by a vector  $\mathbf{m}$ . We normally referred to this process as parameterization of the studied physical process. The operator  $G(\mathbf{m})$  is commonly linking the observed data set  $\mathbf{d}$  to the parameters  $\mathbf{m}$  through a general form expressed by:

$$G(\mathbf{m}) = \mathbf{d} \quad (1)$$

In general, given a set of parameters  $\mathbf{m}$ , expression (1) provides the expected value for the observations  $\mathbf{d}$ . This process is normally indicated as forward modeling and the set of parameters  $\mathbf{m}$  is indicated as the parametrized physical model of the studied system. The inverse problem aims at getting the best fit model  $\mathbf{m}$  from the observation data  $\mathbf{d}$ . It can be found in many different branches of science and engineering. Take the study of the Earth's gravity fields as an example, the governing equation of this specific problem is the Newton's law of universal gravitation  $\mathbf{g}_j = Gm_i/R_{ij}^2$ , where  $G$  is the gravitational constant,  $m_i$  indicates a series of anomalous masses within the planet,  $R_{ij}$  the distance of the anomalous mass  $i$  from the observation point  $j$ , and  $\mathbf{g}_j$  the expected gravity acceleration anomaly at the point  $j$ . In this case  $m_i$  is the parameterized physical model describing the distribution of mass anomalies within the Earth and the observed gravity anomaly is the data vector  $\mathbf{d}$ . Equation (1) can be expressed as

$$\mathbf{m} = \begin{pmatrix} m_1 \\ m_2 \\ \vdots \\ m_p \end{pmatrix}, \mathbf{d} = \begin{pmatrix} \mathbf{g}_1 \\ \mathbf{g}_2 \\ \vdots \\ \mathbf{g}_q \end{pmatrix}, \text{ and } \mathbf{G} = \begin{pmatrix} \frac{G}{R_{11}^2} & \frac{G}{R_{21}^2} & \cdots & \frac{G}{R_{p1}^2} \\ \frac{G}{R_{12}^2} & \frac{G}{R_{22}^2} & \cdots & \frac{G}{R_{p2}^2} \\ \vdots & \vdots & \ddots & \vdots \\ \frac{G}{R_{1q}^2} & \frac{G}{R_{2q}^2} & \cdots & \frac{G}{R_{pq}^2} \end{pmatrix} \quad (2)$$

If we know the distribution of anomalous masses  $m_i$ , we can compute the expected values of gravity anomaly at the place  $g_j$ . In general, we can observe the gravity anomalies (e.g. through a gravimeter or satellite observations) and we are interested in finding a possible distribution of masses that can cause the given gravity anomaly (e.g. we are interested in the location of a hydrocarbon reservoir). With the observed gravitational field at hand to get the density distribution of the Earth is a typical inverse problem. Of course it is a highly non-unique one. It is worth to mention that the way of parameterizing a physical model  $\mathbf{m}$  is not unique, which means that one can choose different kinds of model parameters to describe the same model. For instance, in seismic tomography, we can choose to parameterize the problem either through seismic wave velocity  $v$  or slowness  $s$  (the inverse of seismic wave). Physically both parameterizations would provide the same information we are looking for. In reality, the choice of the slowness parameterization simplifies significantly the mathematics of the inverse problem avoiding a singularity implicit in the velocity formulation.

Inverse problems can be classified according to many different criteria. (Aster et al. 2005) One common way of categorizing inverse problems is based on the form of the physical model and the measured data. If both the model  $\mathbf{m}$  and the observed data  $\mathbf{d}$  are continuous functions of time and space, this kind of inverse problems is called *continuous inverse problems*. The general form of a continuous inverse problem is expressed by Equation (1) with  $\mathbf{d} = d(x, t)$  and  $\mathbf{m} = m(x, t)$ .

However, in most cases both the model and the observed data are not continuous functions of time and space. In this case the operator  $G$  of Equation (1) can be expressed in matrix form (possibly dependent on  $\mathbf{m}$  and  $\mathbf{d}$ ), while the observations and model parameters are expressed as the vector  $\mathbf{d}$  and  $\mathbf{m}$  respectively. Such kind of inverse problems is called *discrete inverse problems*, or *parameter estimation problems*.

Since in many cases a continuous inverse problem can be discretized and well approximated by the resulting discrete inverse problem, so in some literatures, people also named problems with a small number of parameters as parameter estimation problems, and problems with a large number of parameters as inverse problems.

Furthermore, if the whole system under investigation satisfies the condition of linearity that is to say it obeys the rules of superposition (3) and scaling (4), then the problem is called a linear inverse problem.

$$G(m_1 + m_2) = G(m_1) + G(m_2) \quad (3)$$

$$G(\beta m) = \beta G(m) \quad (4)$$

In the circumstances, for a linear parameter estimation problem, the forward operator can be written in the form of a matrix, and so the general form (1) can be rewritten as follows.

$$\mathbf{G}\mathbf{m} = \mathbf{d} \quad (5)$$

where  $\mathbf{G}$  is often named as the observation matrix and is independent of  $\mathbf{m}$  and  $\mathbf{d}$ .

On the other hand, for a linear continuous inverse problem, generally speaking, the operator  $G$  can be represented by a linear integral operator, and the corresponding general form of such kind of problem is:

$$\int_a^b g(y, x) m(x) dx = d(y) \quad (6)$$

where  $g(y, x)$  is termed as the kernel function. An equation having the form of (6) is called a Fredholm integral equation of the first kind (IFK for short), which belongs to a famous set of equations in mathematics. The problem described by an IFK is to find the function  $m(x)$  by given the continuous kernel function  $g(y, x)$  and the function  $d(y)$ , which has exactly the same meaning as solving a continuous inverse problem.

If the kernel  $g(y, x)$  in an IFK is a function only of the difference of its two arguments, that is to say  $g(y, x) = g(y - x)$ , and the integral is over  $(-\infty, +\infty)$ , then the form of Equation (6) can be rewritten as follows

$$\int_{-\infty}^{\infty} g(y - x) m(x) dx = d(y) \quad (7)$$

which is the convolution of the functions  $g$  and  $m$ . Then by applying the Fourier transform, we can get the solution

$$m(y) = \mathcal{F}_f^{-1} \left[ \frac{\mathcal{F}_y[d(y)](f)}{\mathcal{F}_y[g(y)](f)} \right] = \int_{-\infty}^{\infty} \frac{\mathcal{F}_y[d(y)](f)}{\mathcal{F}_y[g(y)](f)} e^{i2\pi y f} df \quad (8)$$

where  $\mathcal{F}_f^{-1}$  and  $\mathcal{F}_y$  stand for the inverse and forward Fourier transform respectively.

As mentioned earlier in this section, in reality the model we use to describe the problem is usually characterized by a finite number of parameters. Some of them are discrete by nature, the others which have continuous parameters can be discretized if the continuous functions involved are smooth enough compared to the sampling interval. (Tarantola 2005, Aster et al. 2005) Besides, many time continuous data are discrete because of the sampling. Therefore, in the rest of the thesis we will deal only with discrete problems, since often continuous problems can be discretized. Let's take a look at the general procedure of solving a parameter estimation problem through some simple intuitive examples.

Imagine that there is a bomb dropped by a bomber falling in the sky. We can track the trajectory of the bomb using radar or other instruments. So the observation data  $\mathbf{d}$  we have are the altitude positions of the bomb measured at a series of time points. We denote the altitude positions as  $\mathbf{h}$ , and the series of time points as  $\mathbf{t}$ . The observation data are the blue points shown in Figure 2.1. What we want to know in this specific problem is when the bomb will land and where it will land. To answer these questions we need to understand how the bomb moves during its fall, in other words, the kinematic properties of the bomb's motion. Since the velocity in horizontal direction  $V_h$  is constant, it can be easily calculated via dividing the horizontal displacement by the time. So the physical model  $\mathbf{m}$  we want to solve should include the following three parameters ( $p = 3$ ): the effective local gravitational acceleration,  $m_1$ , the initial velocity in vertical direction at the time when the bomb and the

bomber separated,  $m_2$ , and the initial altitude of the bomb,  $m_3$ .

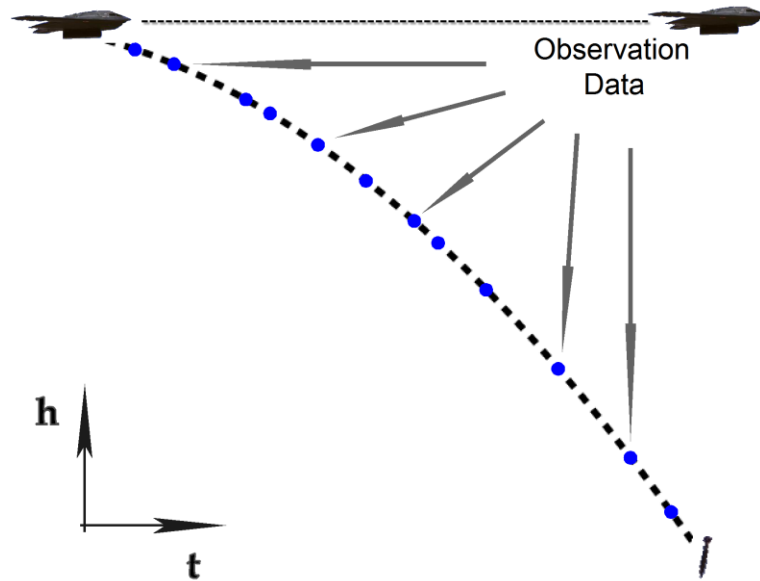


Figure 2.1 Observed data and trajectory of the bomb example.

Assuming that except for the gravity there are no other forces exerting on the bomb, then the falling trajectory of the bomb should have a parabolic shape. The corresponding governing equation of such problem is like:

$$\frac{1}{2}m_1t^2 + m_2t + m_3 = h(t) \quad (9)$$

Applying Equation (9) to all the observation data, we can get the following system of equations.

$$\begin{bmatrix} \frac{1}{2}t_1^2 & t_1 & 1 \\ \frac{1}{2}t_2^2 & t_2 & 1 \\ \frac{1}{2}t_3^2 & t_3 & 1 \\ \vdots & \vdots & \vdots \\ \frac{1}{2}t_q^2 & t_q & 1 \end{bmatrix} \begin{bmatrix} m_1 \\ m_2 \\ m_3 \end{bmatrix} = \begin{bmatrix} h_1 \\ h_2 \\ h_3 \\ \vdots \\ h_q \end{bmatrix} \quad (10)$$

where  $q$  is the number of observation points.

From Equation (10), it is clear to see that for solving  $\mathbf{m}$  the whole system satisfies the condition of linearity (i.e. Equation (3) and (4)), so this problem is a linear parameter estimation problem, and thus it can also be represented by the general form  $\mathbf{Gm} = \mathbf{d}$  introduced in Equation (5) with



$$\mathbf{m} = \begin{bmatrix} m_1 \\ m_2 \\ m_3 \end{bmatrix}, \mathbf{d} = \begin{bmatrix} h_1 \\ h_2 \\ h_3 \\ \vdots \\ h_q \end{bmatrix}, \text{ and } \mathbf{G} = \begin{bmatrix} \frac{1}{2}t_1^2 & t_1 & 1 \\ \frac{1}{2}t_2^2 & t_2 & 1 \\ \frac{1}{2}t_3^2 & t_3 & 1 \\ \vdots & \vdots & \vdots \\ \frac{1}{2}t_q^2 & t_q & 1 \end{bmatrix}.$$

Under the ideal circumstances, if both the model parameters and observation points have the same number ( $q = p = 3$ ) and all the observations are exact (i.e. without any uncertainties), then we can calculate  $\mathbf{m}$  by directly inverting the observation matrix  $\mathbf{G}$ , which gives

$$\mathbf{m} = \mathbf{G}^{-1}\mathbf{d} \quad (11)$$

However, we are not living in a perfect world. In almost all the cases, the observation matrix  $\mathbf{G}$  is not invertible, even if it is a square matrix, or the number of parameter is not the same of the number of observations. One reason why even a square matrix (i.e. same number of parameters and observation) is not giving a unique solution is the presence of uncertainties (i.e. noise) in the observation dataset. Another reason for which a unique solution is often not existing, is that generally we cannot ensure that we have enough information from independent observations. In mathematical words, the observation matrix  $\mathbf{G}$  is rank deficient. This kind of equation system is also known as the underestimated system, which means it has more than one solution.

There is another case where we have more observation data points than the model parameters ( $q > p, rank(\mathbf{G}) > p$ ), i.e. there are more equations than unknowns in the system as shown in Equation (10), and the rank of  $\mathbf{G}$  is larger than  $p$ . This kind of equation systems is termed as overestimated system in linear algebra.

For an overestimated problem, the observation matrix  $\mathbf{G}$  is no longer a square matrix, and so it cannot be directly inverted. Furthermore, the overestimated system has other issues like equation inconsistency, which means that it is impossible for us to find an exact solution which satisfies all the  $q$  equations perfectly.

The reason why the overestimated system has equation inconsistency is because the observation data  $\mathbf{d}$  always contain uncertainties. If we denote the theoretical predicted values determined by the underlying physical system as  $\hat{\mathbf{d}}$ , then we have the following relation

$$\begin{aligned} \mathbf{d} &= \hat{\mathbf{d}} + \varepsilon \\ \hat{\mathbf{d}} &= \mathbf{G}\mathbf{m} \end{aligned} \quad (12)$$

where  $\varepsilon$  represents the uncertainties.

Hence

$$\mathbf{G}\mathbf{m} + \varepsilon = \mathbf{d} \quad (13)$$

Generally speaking, the uncertainties contained in the observation data result from two main sources. (Tarantola 2005) One source is the measurement errors produced either by instruments or people who manipulate the instruments. This kind of uncertainty is inevitable and can only be reduced by applying more advanced techniques and more accurate measuring tools. The other source of uncertainties is due to the imperfection of physical models we use. That is because when we establish a physical model to describe a problem, we usually cannot take all the factors into account. Furthermore, often some less important factors or parameters need to be neglected because of the limit of computing power or just for the sake of the mathematical convenience.

For instance, in our bomb example, we have neglected the mass distribution of the bomb as well as the air drag experienced by the bomb during its falling. All these factors have some sort of influences to the bomb's trajectory, so the real trajectory is not a perfect parabola and the governing equation should have more complicated form than the simple quadratic equation shown in (9).

Thus we have

$$\varepsilon = \varepsilon_m + \varepsilon_i \quad (14)$$

where  $\varepsilon_m$  is the uncertainties resulted from measurement errors and  $\varepsilon_i$  the uncertainties due to model imperfection. If we assume that all the assumptions we did to parameterize the model to simplify the model are suitable, then the term  $\varepsilon_i$  can be considered as zero. In this case, the uncertainties of observation data are completely produced by the noise in the measurements or measurement biases.

$$\varepsilon = \varepsilon_m \quad (15)$$

In order to find the parameters that best represent the observed physical model, in the case that a formal inverted matrix  $\mathbf{G}^{-1}$  does not exist, we prefer to solve the equation system (13) in an approximate sense, which means we will try to find the model parameters  $\mathbf{m}$  which produce the predicted values  $\hat{\mathbf{d}}$  that best fit the observation data  $\mathbf{d}$ .

In order to describe how well the predicted values  $\hat{\mathbf{d}}$  determined by model parameters  $\mathbf{m}$  will fit the observation data  $\mathbf{d}$ , we need to define a measure of misfit. Generally speaking, in most cases, the smaller the misfit measure is, the better the corresponding approximate solution will be.

One of the commonly used misfit measures is the Euclidean norm (or the  $L_2$  norm) of the residuals, in other words, of the differences between the theoretical predicted values and the observation data.

$$\|\mathbf{d} - \mathbf{G}\mathbf{m}\|_2 = \sqrt{\sum_{i=1}^q (d_i - (\mathbf{G}\mathbf{m})_i)^2} \quad (16)$$

The traditional least squares method is based on this kind of misfit measure. In least squares, our goal of solving the inverse problem is identical to minimizing the squares of the  $L_2$  norm of the residuals.

$$\min_{\mathbf{m}} \|\mathbf{d} - \mathbf{Gm}\|_2^2 \implies \min_{\mathbf{m}} (\mathbf{d} - \mathbf{Gm})^T (\mathbf{d} - \mathbf{Gm}) \quad (17)$$

We can do it by applying the necessary condition at the minimum

$$\left. \frac{\partial((\mathbf{d} - \mathbf{Gm})^T (\mathbf{d} - \mathbf{Gm}))}{\partial \mathbf{m}} \right|_{\tilde{\mathbf{m}}} = 0 \quad (18)$$

which is

$$\left. \frac{\partial(\mathbf{d}^T \mathbf{d} - (\mathbf{Gm})^T \mathbf{d} - \mathbf{d}^T \mathbf{Gm} + (\mathbf{Gm})^T \mathbf{Gm})}{\partial \mathbf{m}} \right|_{\tilde{\mathbf{m}}} = 0 \quad (19)$$

which gives

$$\mathbf{G}^T \mathbf{G} \tilde{\mathbf{m}} - \mathbf{G}^T \mathbf{d} = 0 \quad (20)$$

And so the approximate solution is

$$\tilde{\mathbf{m}} = (\mathbf{G}^T \mathbf{G})^{-1} \mathbf{G}^T \mathbf{d} \quad (21)$$

if  $\mathbf{G}^T \mathbf{G}$  is invertible.

It can be proven that the approximate solution  $\tilde{\mathbf{m}}$  based on the  $L_2$  norm of residuals is statistically the most possible solution if the uncertainties of the data are Gaussian uncertainties; that is to say, the uncertainties of the data are normally distributed. For this reason parameter estimations based on  $L_2$  norms are often called Maximum Likelihood method. However, sometimes, it is possible to have to deal with noise not Gaussian distributed or the presence of large outliers. In such cases, the  $L_2$  norm may not be the best choice for misfit measure, since the influences of outliers will be amplified significantly. To overcome this drawback and maintain the quality of solution, often people introduce a weight term or use an alternative norm to measure the misfit (e.g. the  $L_1$  norm (also called Manhattan norm)) of the residuals

$$\|\mathbf{d} - \mathbf{Gm}\|_1 = \sum_{i=1}^q |d_i - (\mathbf{Gm})_i| \quad (22)$$

This norm is much less sensitive to outliers compared to the  $L_2$  norm.

The  $L_1$  norm has been widely used in the cases where outliers are present or suspected in the observation dataset. (Parker 1994, Scales et al. 2001, Aster et al. 2005) The method of trying to solve the inverse problem by minimizing the  $L_1$  norm of the residuals is named as the least absolute values method. It is worth to mention that because of the properties of the sum of absolute values the minimum solution of  $L_1$  norm of residuals may not be unique even just under linear constraints. (Tarantola 2005)

Besides the  $L_2$  and  $L_1$  norm, there are many other norms which can be used as the misfit measures, e.g. the  $L_\infty$  norm of the residuals

$$\|\mathbf{d} - \mathbf{Gm}\|_\infty = \max_{1 \leq i \leq q} |d_i - (\mathbf{Gm})_i| \quad (23)$$

which is also known as minimax norm or Chebyshev norm. It is often used in the cases where there are strict constraints on uncertainties.

The measure of misfit must be a norm in mathematical sense. Under this condition, one could choose any suitable forms of misfit measure according to the requirements of different problems.

Generally speaking, solving nonlinear parameter estimation or nonlinear inverse problems is much more difficult than solving the linear ones. It needs more time and computing power. In some cases, the nonlinear inverse problems can be converted to linear inverse problems via variable substitution, series expansion, or coordinate transformation. After linearization, this problem can be solved using traditional methods like maximum likelihood or least squares. In other cases it is not possible to linearize the problem, in this case nonlinear optimization techniques (e.g. the gradient-based Gauss-Newton (GN) and Levenberg-Marquardt (LM) methods) or evolutionary algorithms (such as genetic algorithm (GA) and simulated annealing algorithm (SA)) have to be used to obtain a solution. These methods often start with an arbitrary point in the space of the model parameters, called initial guess or initial solution, and then improve this initial guess in an iterative way until a suitable solution is found. It should be noted that iterative models can converge to a local minima and not to the global best parameter estimation. This means that a global optimization techniques (such as multi-start methods) should be careful and be sure it is not converging to a “wrong” solution. Further details on this topic can be found in (Parker 1994, Scales et al. 2001, Tarantola 2005).

Compared with the forward problems, there are several crucial issues that need to be considered, when solving inverse problems. Some issues like inexistence and nonuniqueness of the inversion solution have already been mentioned before. Another essential problem often encountered in inverse solution procedure is the instability of a solution, a tiny perturbation in the observation data will result in significant perturbation in the solution model parameters. In such cases, the so called regularization techniques have to be applied. By introducing additional information or constraints (e.g. prior knowledge) of the model, the ambiguity and instability of the solution will be reduced, and so the ill-posed inverse problems can be successfully solved. (Zhdanov 2002, Aster et al. 2005, Tarantola 2005)

## **2.2 Inverse problems in geoscience**

After talking about the typical inverse problems in general, we would like to restrict our scope to discuss the inverse problems in geoscience. The inverse problem is probably one kind of the most common problems that can be seen in nearly all the fields of geoscience. A number of inverse theories and methods have already been developed and successfully applied by previous researchers to deal with the problems arisen in many different geoscience as well as industrial applications. Typical examples include finding an ore deposits or oil field in mining and petroleum industries (Parker 1994, Menke 1989, Mani et al. 2006), understanding the internal structure of the planet using seismology or geophysical observations, or locating artifacts in archeological sites using geophysical observations.

In terms of geophysics, the observation data are usually the physical fields produced by natural or artificial sources and propagated through the Earth's interior (Zhdanov 2002). Generally we want to know the values of the parameters of those sources as well as the physical properties of the media through which the field is propagating. This inversion can provide information on things like the internal structures of the Earth or provide information on the processes that generated the observed field. Here we would like to take a look at some of the most important geophysical fields including the gravity field, the magnetic field, the electromagnetic field, the seismic wave field, as well as the surface deformation field. (Zhdanov 2002)

As already discussed previously at the beginning of the chapter, the gravity field, provides information on density or mass distribution beneath the ground from the measurement of anomalous acceleration at the Earth's surface. The governing equation is the Newton's law of gravity and the inverse problem has the general form

$$\rho = G_g^{-1}(\mathbf{g}) \quad (24)$$

where  $G_g^{-1}$  is the inverse gravity operator,  $\mathbf{g}$ , the observed gravity field, and  $\rho$ , the density distribution.

For the magnetic field, what we want to know is the intensity of magnetization underground or the magnetic susceptibility of subsurface structures, it is often used to locate ore deposits, since very high susceptibility minerals are often accompany with the ore deposits. It is typically used also to locate magmatic bodies or tectonic structures offsetting magmatic bodies. Another typical use is related with archeology since it is very sensitive to anthropogenic artifacts (like burying sites or walls). The general form of this kind of problem is

$$\mathbf{I} = G_H^{-1}(\mathbf{H}) \quad (25)$$

where  $G_H^{-1}$  represents the inverse magnetic operator,  $\mathbf{I}$ , the intensity of magnetization vector, and  $\mathbf{H}$ , the corresponding observed magnetic field.

For these two fields, since both the inverse operator  $G_g^{-1}$  and  $G_H^{-1}$  are linear operators, the related inverse problems are linear. (Note that both solutions are still highly not unique since different density distributions can produce the same gravity field).

For the electromagnetic field, the governing equation is the Maxwell's equations (Stratton 1941) and our purpose is to determine the values of the electromagnetic parameters of the examined media by measuring the electromagnetic fields at the ground surface. The general form of the related inverse problem is

$$[\sigma, \epsilon_r, \mu] = G_{em}^{-1}(\mathbf{E}, \mathbf{H}) \quad (26)$$

Where  $\sigma$ ,  $\epsilon_r$  and  $\mu$  present the electric conductivity, (some people prefer to use the re-

sistivity  $\rho$ , which is the inverse of the electric conductivity), the relative permittivity and the magnetic permeability, respectively,  $G_{em}^{-1}$ , the inverse electromagnetic operator,  $\mathbf{E}$ , the observed electric field, and  $\mathbf{H}$ , the corresponding observed magnetic field.

The three electromagnetic parameters are of great importance, since they can provide precious information regarding the mineral content and physical structure of the rocks, as well as material properties about the fluids in the rocks.

As last example let's look at seismic wave propagation. The dominant equation for the seismic wave field is the wave equation. The parameters of interest is generally velocity (or its inverse the slowness) distribution of the material inside the Earth. Seismic velocity depends on material properties typical for different rocks and/or rock status. What is generally measured is the arrival time of some kind of waves at a typical frequency or the polarity of the wave. From these observations one can solve for the source (if the velocity structure is known) or the velocity structure (if the source is known). Because of its high resolution, the seismic inversion method turns out to be one of the leading methods used especially in oil and gas prospecting applications (see Figure 2.2). The general form of the corresponding inverse problems is

$$\mathbf{v} = G_s^{-1}(\mathbf{t}, \mathbf{P}) \quad (27)$$

where  $G_s^{-1}$  is the inverse seismic operator,  $\mathbf{v}$ , the velocity of elastic seismic wave propagation,  $\mathbf{t}$ , the travel time of the seismic waves when they reach the receivers, and  $\mathbf{P}$ , the positions of seismic receivers.

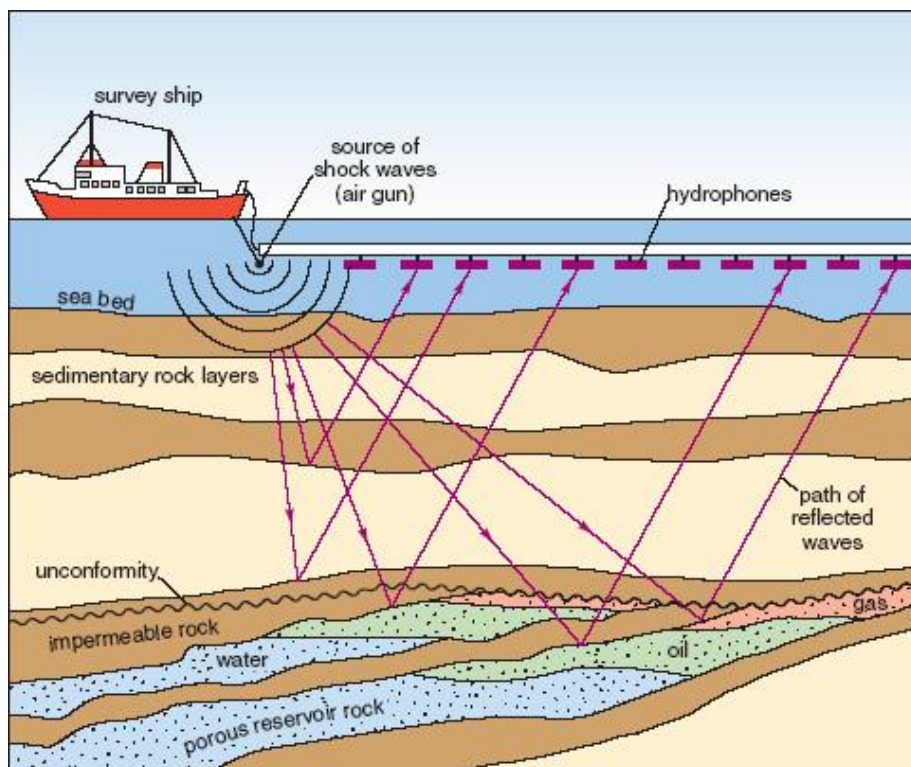


Figure 2.2 Seismic method of prospecting for oil and gas<sup>1</sup>, CC-BY-SA-NC.

Last but not least, we would like to talk about the surface deformation field, which is of great importance and very useful in hazard assessment, especially for some natural hazards like volcanic activity, landslide, ground subsidence, etc. (Fialko and Simons 2000, Hoffmann et al. 2001, Commend et al. 2004, Casagli et al. 2009, Liu et al. 2010, Zhang et al. 2010, Masterlark et al. 2012)

The inverse problems in surface deformation fields have a vast variety of different forms. Let's take the applications regarding volcanic activities as an example. For such problems, the observation data we have is the surface deformation fields of the volcanic area obtained by geodesic techniques, and our goal is to determine the values of parameters of the possible magma chamber such as its shape, dimensions, the change of its volume or inner pressure as well as where it locates. Based on all these information we can estimate and predict the possibility of, for example, volcanic eruptions in the future. The general form of inverse problems can be written as

$$\mathbf{m} = G_u^{-1}(\mathbf{u}) \quad (28)$$

where  $G_u^{-1}$  represents the inverse deformation operator,  $\mathbf{u}$ , the observed surface deformation field, and  $\mathbf{m}$ , the inversed model parameters of the source, such as magma chamber and fault.

Not like the first two kinds of fields, the operators of inverse problems arisen in the latter three fields are normally nonlinear operators since the governing equations of the related physical systems have highly nonlinear relations, and thus the involved problems are nonlinear inverse problems (Scales et al. 2001, Zhdanov 2002). As mentioned in the previous section, solving nonlinear inverse problems is much more difficult than the linear ones. In this work, we will focus on solving the inverse problems in the surface deformation fields.

As is well known, the structure of the Earth's interior is very complex. (Press and Siever 1994) Although there are many complicated mathematical models established by previous researchers in order to describe the geophysical phenomena, they are still so simplified compared with the reality. This is one reason why geophysical inverse problems are generally much more difficult to solve. (Hickey et al. 2015)

Another difficulty comes from the observation data. In the past, due to the limits of available geodesic tools and techniques, usually, we can only acquire data at a limited number of observation points, so the amount of observation data is insufficient. Nowadays, with several new developed techniques, we can get a huge amount of observation data on a wide scale in both time and space. However, as mentioned before, the observation data always contain a lot of noise. Moreover, due to the complicated geophysical system under

---

<sup>1</sup> <http://www.agilegeoscience.com/journal/2011/6/6/what-is-avo.html>

study, it is generally impossible to clarify each kind of noise, since there are too many known and unknown factors which may introduce some sort of noise into the observed data. (Dzurisin 2007) How to minimize the influence of existing unclear noises and obtain relatively good inversed solution is a quite challenging issue.

Because of the complexity and difficulty of the geophysical inverse problems, it has been suggested by many researchers (Nunnari et al. 2001, Newman et al. 2006, Liu et al. 2010) that using a combination of different kinds of observation data (e.g. using the surface deformation, gravity field and magnetic field together) or using the same kind of geophysical data acquired by multiple independent sources (such as using the surface deformation data obtained by both GPS and EDM techniques) will lead to a much better or more accurate solution than just using a single source of geophysical data. It is because a geophysical phenomenon usually causes observable changes in several different geophysical fields simultaneously, for instance, the intrusion of magma often results in significant changes in gravity, seismic wave, along with the surface deformation fields. Therefore, the more sources of observation data are considered, the better the final inversed solution is constrained. Given the increasing amount of observations (both in term of spatial coverage and type of observations) it is increasingly important to introduce more realistic modeling in our interpretation. Unfortunately, as already stated at the beginning of the chapter, using complex models in combination with traditional inverse theory is not always practical. Still in recent years it has become a very hot topics (in particular in volcano geodesy Hickey et al. 2013, Hickey and Gottsmann 2014). In the rest of the thesis we will discuss a novel approach to use FEM in the inversion for sources of deformations.



## Chapter 3

### Data Acquisition and Selection

---

In recent decades, with the help of great development occurred in computer science and related technologies, the geodetic and remote sensing techniques have taken a huge step forward. Many new techniques have been invented and successfully applied in a variety of different fields of geoscience applications. Their ability of continuously and remotely monitoring the 1-D or 3-D ground surface deformation fields on a large scale both in space and time as well as the quality and accuracy of observed data have been improved dramatically. Here, we would like to introduce two major geodetic tools, the Global Positioning System (GPS for short) and interferometric synthetic-aperture radar (often abbreviated as InSAR), which are getting more and more popular and becoming the standard ways of acquiring ground surface deformation data in many geophysical applications, especially for monitoring volcanic areas in volcanology (Poland et al. 2006, Currenti et al. 2008b, Palano et al. 2008, Ruch et al. 2008, Ruch and Walter 2010, Anderssohn et al. 2009, Casagli et al. 2009, Zhang et al. 2010). However, a thorough description about the technical details of them is beyond the scope of this thesis. More detailed information can be found in (Massonnet and Feigl 1998, Kampes 2006, Dzurisin 2007). It needs to be mentioned that all the real surface deformation data used in this work are acquired by applying these two techniques.

### 3.1 Data acquisition techniques

#### 3.1.1 The Global Positioning System (GPS)

The Global Positioning System, i.e. GPS, is a well-known term, which is familiar to many people through its usage in their daily life such as driving navigation or Google Maps services. It refers to the space-based satellite navigation system that freely provides twenty-four-hour location and timing information anywhere on the Earth, in all weather, to anyone who has a GPS receiver. The GPS was firstly developed by the US government in 1973. It was originally designed for military use and, later, it was opened to civil and commercial users as well. Besides GPS, there are other similar systems in use or being planned, such as the Russian global navigation satellite system (GLONASS), the European Union Galileo positioning system, and the Chinese compass navigation system. (Rip and Hasik 2002)

The reference surface commonly used for GPS calculations is the mean Earth ellipsoid,

which centers at the Earth's mass center and whose semi-major and semi-minor axes are defined by the Earth's equatorial and polar radii, respectively. Nowadays the most widely used reference ellipsoid is the World Geodetic System 1984 (WGS84), based on which the global coordinates system used by GPS is defined. The coordinates system is also centered at the Earth's center of mass. Its first axis starts from the center and points to the intersection of the Greenwich meridian and the Earth's equator. The third axis is along the direction of the Earth's rotation pole for the year 1984. And finally the second axis is perpendicular to the other two axes. The coordinates can be written in terms of longitude and latitude in degrees or use the Universal Transverse Mercator (UTM) coordinates in meters, depending on different demands. (Dzurisin 2007)

The core of Global Positioning System consists of at least 24 operational satellites deployed in six circular orbits at a height of 20200 km around the Earth. These orbits are centered on the Earth and fixed with respect to the distant stars instead of rotating together with the Earth. (Dixon 1991) All the satellites are distributed in a way that ensures for each point on the Earth at any time there are at least four up to ten satellites visible above the horizon.

Each operational satellite of the constellation continuously transmits signals on certain frequencies to the Earth. The signals are normally modulated by the so called pseudorandom noise codes, which are some sort of noise-like repeated binary pulses. And they carry important messages about the satellite itself such as the satellite's individual vehicle time, the correction for the offset of its clock, its orbits information, the satellite health status, as well as some information regarding the ionosphere-related delays.

All these signals can be acquired by using the GPS receivers. With the information at hand, we can determine the position of a point on the Earth where the receiver locates. In order to calculate the position of a receiver, we need to obtain the signals from at least four different satellites simultaneously. Generally speaking, the more satellites are available, the higher the accuracy of resulting position will be.

In the mathematically ideal case, just using the signals from three satellites is adequate to uniquely determine a receiver's position, because it has only three unknowns, however, since there is always a time offset between the receiver and the GPS time, the fourth satellite is needed for timing correction. Thus we have four independent equations in total to solve for the four unknowns. If more satellites are available, then the number of independent equations will be more than the number of the unknowns. And the resulting receiver coordinates will be much more accurate. A simplified error-free formula illustrating the basic principle of calculating receiver's position from GPS signals is shown below.

$$R_r^s = r_r^s + c \times (dt_r - dt^s) \quad (29)$$

in which

$$r_r^s = \sqrt{(x^s - X_r)^2 + (y^s - Y_r)^2 + (z^s - Z_r)^2} \quad (30)$$

where  $R_r^s$  denotes the measured pseudorange between the satellite and the receiver, which is equal to the travel time of the satellite signals  $\tau$  multiplied by the speed of light  $c$ ,  $r_r^s$ , the real distance between the receiver at time  $t$  and the satellite at time  $(t - \tau)$ ,  $dt_r$ , the

time offset from GPS time of the receiver clock,  $dt^s$ , the satellite clock's time offset from the GPS time,  $(x^s, y^s, z^s)$ , the coordinates of the satellite at time  $(t - \tau)$ , and  $(X_r, Y_r, Z_r)$ , the wanted receiver coordinates at time  $t$ . (Hofmann-Wellenhof et al. 2001)

Among these variables, the travel time of the signals can be measured by the receiver, the coordinates of the satellite as well as the satellite clock offset are known from the information carried by the signals, and the speed of light is a constant, so only four unknowns are left, which are the receiver's position and its clock offset.

In Equation (29), no error effects are taken into account. But in practice, the GPS signals acquired by the receiver are always subjected to certain errors such as the time delays occurred when signals passing through the ionosphere and troposphere, the multi-path error, the error from model imperfection, and some kind of measurement errors. Fortunately, some of these errors can be easily eliminated or greatly diminished via GPS data combination and difference methods. (Hofmann-Wellenhof et al. 2001) As a result, in general the surface deformation data acquired by GPS can achieve a millimeter level accuracy in three dimensions.

Depending on different choices of reference point, the GPS positions can be classified as absolute positions and relative positions. The former is based on the global coordinates system defined before, while the latter is with respect to some local control points. In geoscience applications, the relative positions are more often used, since we usually care more about the relative deformation at observation points with respect to certain local references than their absolute positions. There are many different relative positioning techniques available such as static GPS, stop-and-go kinematic GPS, rapid static GPS as well as real time kinematic GPS. (Hoffmann-Wellenhof et al. 2001)

Thanks to the revolutionary developments of hardware and software happened in recent years, continuously monitoring a single point's motion is possible, which leads us to the present most advanced GPS positioning techniques, the continuous GPS (CGPS) technique. There are many large CGPS networks currently being used for geoscience applications, especially for monitoring some of the dangerous volcanoes where it is too risky for people to work, since the CGPS stations can be operated remotely. The surface deformation data provided by CGPS networks are continuous in time and with a millimeter level accuracy, however, due to some natural limits (e.g. topographical restrictions for construction of CGPS stations) and safety concerns, the observation points are spatially too sparse. And this shortcoming can be overcome by applying other geodetic techniques such as interferometric synthetic aperture radar.

### 3.1.2 Interferometric Synthetic Aperture Radar (InSAR)

Interferometric synthetic aperture radar (InSAR) is a relatively new powerful geodetic and remote sensing technique used for measuring the Earth's surface deformations and topography. The development of the InSAR technique started with the ERS-1 satellite launched by the European Space Agency (ESA) in 1991. And it was firstly made known to the world by its successful application on the M 7.3 Landers earthquake occurred to the east of Los An-

geles, California on 28 June 1992, which was published on the 8 July 1993 issue of *Nature* (Massonnet et al. 1993). Since then, during the last two decades, it becomes more and more popular and turns out to be the only technique which is capable of monitoring in all-weather the surface deformation fields with centimeter accuracy on a wide spatial scale over timespans of several days to years. (Kampes 2006, Dzurisin 2007) It has been successfully applied in monitoring surface displacements generated by some natural hazards, such as volcanoes, earthquakes, landslides, as well as the ground uplift and subsidence. (Massonnet and Feigl 1998)

By definition, InSAR techniques use two or more synthetic aperture radar images of the same area, with the help of interferometric image processing techniques, to get the surface deformation fields during the time span defined by the image acquisitions. There are two important terms within it: the one is the synthetic aperture radar (SAR), and the other is the interferometric image processing. We will explain them in a little bit more detail, respectively.

Before introducing synthetic aperture radar, we need to talk about radar first. Radar is a term abbreviated from "radio detection and ranging". It is an active sensing system using microwaves to work. More precisely, the radar system transmits microwaves at certain frequencies and collects the waves reflected by the targets. Based on the arrival times of the reflected microwaves, the radar can determine the distances between the targets and itself. Because of this active working style, radar system can work effectively both in day and night. Moreover, due to its relatively longer wavelength, radar signals can pass through clouds and ashes easily, which makes it a perfect geodetic tool for observing surface deformation fields regardless of weather conditions. To better distinguish among targets at different distances at the same time get enough amount of signals reflected back to the radar, a suitable angle of incidence should be chosen carefully, for the satellite ERS-1 an incidence angle of 23 degrees is used and for the TerraSAR-X satellites we used, the incidence angles are 43.35 and 31.8 degrees, respectively.

The synthetic aperture radar (SAR) firstly proposed by Carl A. Wiley in 1965 is a form of radar different from real aperture radars. It makes use of the different frequencies generated by the Doppler Effect in the reflected signals to distinguish different targets that cannot be identified by only using the real aperture radar before. Through the motion of the source, it is possible to simulate the use of a very large synthetic antenna, and the azimuth resolution of the radar is improved by two or three orders of magnitude, which is approximately equal to half of the antenna's length. (Massonnet et al. 1993, Bamler and Hartl 1998)

Now we are going to talk about the principles of SAR interferometry techniques, which allow the SAR to image centimeter-scale surface deformations we needed. Not like other image processing techniques, SAR interferometry works based on the phase information of the echo signals. In order to do SAR interferometry, we need to have multiple (at least two) overlapping radar images of the same area. The overlapping radar images can be obtained by using multiple separate radars at slightly different positions observing the target area simultaneously or by using the same radar observing the target area from exactly the same position at different times. In this work, we use multiple passages of satellites and not a sin-

gle time observations by multiple satellites because we are interested in deformation and not only in topography. After we got the overlapping radar images, we need to co-register them so that we can apply subtraction on their phase information at corresponding pixels. The co-register operation depends highly on good spatial coherences between each radar images. When two overlapping radar images are successfully co-registered, the resulting image generated by subtracting their phase values is called an interferogram. The interferogram contains useful information about surface displacements which we need together with other signals that need to be corrected for, such as topography, delays due to atmospheric effects, and noises. After applying some mathematical treatments, the unwanted effects can be removed from the interferogram, e.g. using the digital elevation model (DEM) we can remove the effect of surface topography. Then we can obtain the surface deformation from the treated interferogram. It should be mentioned that the deformation observed by InSAR is only in line of sight. A typical treated interferogram is shown below in Figure 3.1.

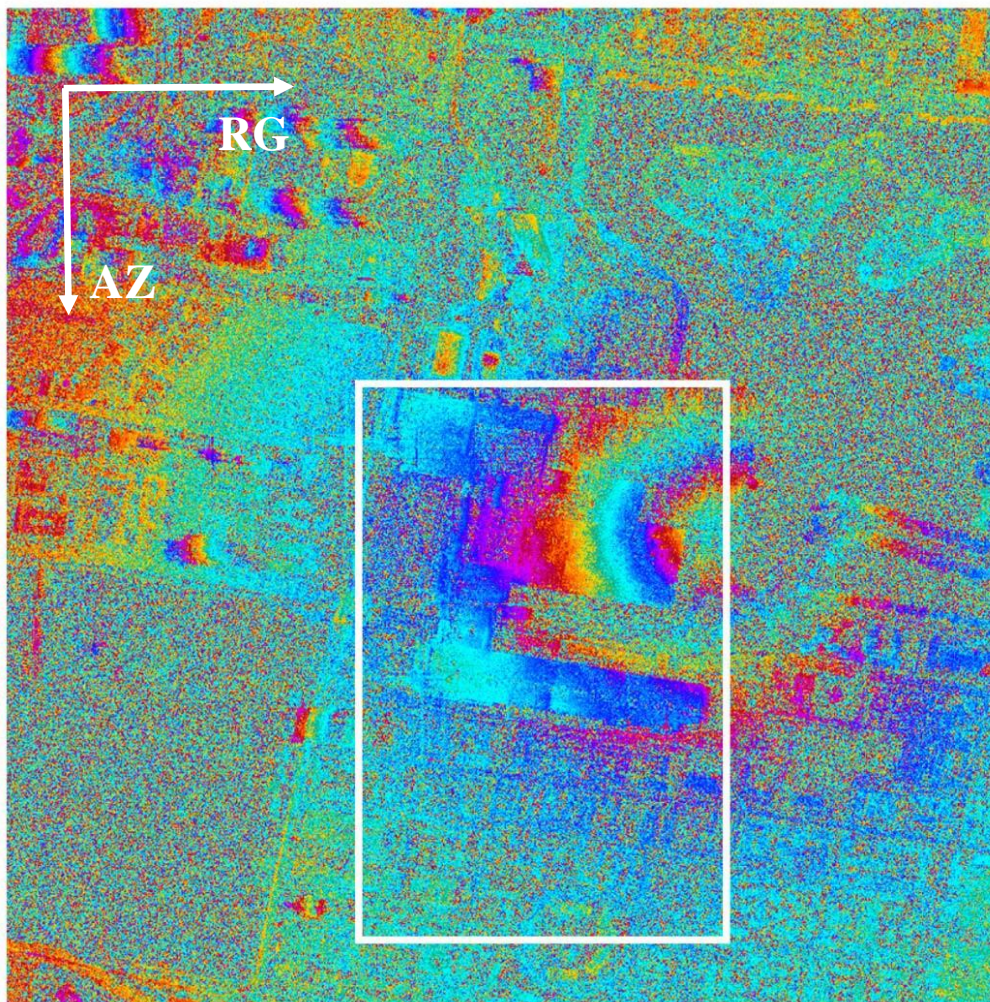


Figure 3.1 Differential interferogram of the test site centered at the convention center in Las Vegas (Zhu and Bamler 2011). It can be seen that there are many fringes in the figure. Each complete interference fringe is shown as a spectrum of colors from violet to green to red in the inter-

ferogram. Each fringe results from a half-wavelength  $\lambda/2$  range change (i.e. the surface displacement) occurred between two image acquisitions. So the interferogram shown here is similar to a deformation map with contour lines. We can get the total amount of surface deformation by counting the number of complete fringes. In our case, since the wavelength of the InSAR we use is 3.11 cm, each fringe corresponds to a range change of  $\lambda/2 = 1.55$  cm, which is quite a high resolution.

In general, InSAR is a powerful geodetic tool and is very sensitive to the surface displacements (of millimeter-scale). It is a highlighted feature required by geophysicists. But currently the time resolution of InSAR (i.e. the orbit repeat cycles) is not small enough, in our case, 11 days, so continuous monitoring is not possible.

## **3.2 Data selection**

In today's geoscience applications it is normal to have a huge amount of observed data, especially for using continuous GPS and Persistent Scatterer InSAR techniques (Kampes 2006). The dataset might contain millions of data points distributed over a huge area of hundreds of square kilometers. However, due to the quality of the data and the limits of computing power, only a part of the whole dataset can be used in further calculation. Thus how to efficiently and effectively select the most important part of data points from the whole dataset becomes a key issue, which in some sense, determines the quality of the final inversion solution. Considering the natural features of observation data in surface deformation fields, we decide to use the so-called weighted uniformly selecting method to select the useful data points, which are named in this thesis as Investigation Points (IPs). The selecting method is implemented by applying combination genetic algorithm (CGA) in programming. (Chen and Hou 2006)

Before talking about the combination genetic algorithm, we would like to first present a short overview of its famous family, the genetic algorithms (GA).

### **3.2.1 The typical genetic algorithm**

Genetic algorithms (GAs) are a part of evolutionary computing theory, which is a rapidly growing field of artificial intelligence. The idea of evolutionary computing was first proposed by I. Rechenberg in his work "Evolution strategies" in 1960s. His idea was then developed by many other researchers. The genetic algorithms which are inspired by the well-known Darwin's theory about evolution were invented by John Holland and developed by himself together with his students and colleagues. This led to Holland's book "Adaption in natural and artificial systems" published in 1975, in which the genetic algorithms are explained theoretically.

The Genetic algorithms are basically stochastic evolutionary algorithms. They apply the principles of evolution found in nature to the problem of finding optimal solutions. The

searching methods they used imitate a few natural phenomena such as genetic inheritance and Darwinian strife for survival (Michalewicz 1992). In a word, the idea behind genetic algorithms is nothing but to do exactly what the nature does. Simply stated, the solution to an optimization problem solved by genetic algorithms is evolved.

In order to better understand the working principle of the genetic algorithm, let us take a look at its biological background.

As is well known, except for virus, all living organisms consist of cells. In the nucleus of each cell, chromosomes carry genetic information. A chromosome is a thread-like structure, in which DNA is tightly coiled many times around histones. Genes, which are made up of DNA, act as instructions to produce proteins and are the basic physical and functional units of heredity. Variant forms of a gene detected as different phenotypes are called alleles. Every person has two alleles of each gene, one inherited from each parent. Furthermore, each gene has its own position in the chromosome, which is called locus (string positions).

The whole set of DNA is called genome. A particular set of genes in genome is called genotype (or individual). The genotype is a major influencing factor in the development of the organism's phenotype, which consists of physical and mental traits such as hair color, intelligence as well as left- and right-handed.

During meiosis, DNA recombination (or crossover) occurs. Genes from parents form in some way a novel combination. The new created offspring can also be mutated. DNA mutation means that the DNA sequence is permanently altered. Some of the changes are due to errors in DNA replication, and some of them may happen because of other reasons such as radiation or chemical induced.

The fitness of an organism is measured by success of the organism in its life.

Let's take the famous rabbits example to illustrate this process more clearly. (Michalewicz 1992)

Assuming at a given time, there is a population of rabbits. Among them, some rabbits are cleverer and stronger, while others are not. These cleverer and stronger rabbits can run faster, so they are more possible to successfully escape from being caught by foxes. As a result, more of them can survive to make more rabbits. Of course, some of the weaker, dumber rabbits are lucky enough to survive as well. This survival population of rabbits begins to breed. The result of breeding is a good mixture of rabbit genetic material, that is to say, some strong rabbits breed with weak ones, some strong with strong, some clever rabbits breed with dumb ones, some dumb with dumb, and so on and so forth. One thing has to be mentioned is that nature throws in a so-called 'wild hare' occasionally by just mutating some parts of the genetic material. The new generation of rabbits will averagely be stronger and cleverer than their parents in the original population because there are more cleverer and stronger parents survived from foxes. This process repeats again and again, so that the rabbit genetic material will be better and better.

A genetic algorithm follows just the same procedure described above step by step. The terms used in genetic algorithms are also borrowed from natural genetics.

Genetic algorithm starts with a set of individuals called a population. One individual is also called one genotype contains one or more chromosomes.

Each individual represents a potential solution to the problem. The search space is the space which consists of all the feasible solutions. An evolution process runs on a population of individuals corresponds to a search through the search space. This search should compromise both the exploitation of best individuals and the exploration of the search space. (Michalewicz 1992) In general, random search strategy only emphasizes on the exploration part with ignoring the exploitation. However, genetic algorithms proven to be a method which can balance exploitation and exploration of search space well.

The population experiences a simulated evolution: for each generation, the relatively good individuals reproduce while the relatively bad ones die.

### **Structure of genetic algorithms**

A typical genetic algorithm should include the following five components. (Michalewicz 1992)

1. A genetic representation for potential solution (individual) to the problem.
2. A method to produce the first generation of individuals.
3. An evaluation function (also called fitness function) which plays the role of the environment or nature, judging individuals according to their “fitness”.
4. Genetic operators such as crossover and mutation.
5. Parameter settings that genetic algorithm needed (e.g. population size, probability of using genetic operators.)

The outline of typical genetic algorithm is below:

1. **Start:** Create random initial population of  $n$  individuals (possible solutions to the problem).
2. **Fitness check:** Evaluate the fitness function  $f(x)$  of each individual  $x$  in the population.
3. **New generation:** Generate a new population by repeating the following steps until the new population is complete.
  - i. **Selection:** Select two individuals as parents from the population according to their fitness. Generally speaking, the better fitness, the bigger chance to be chosen.
  - ii. **Crossover:** With a crossover probability use the selected parents to produce new offspring (children individual). If no crossover was performed, then the offspring is an exact copy of parents.
  - iii. **Mutation:** With a mutation probability mutate a new offspring at random loci (position in chromosome).



- iv. **Accepting:** Place new offspring in the new population considered avoiding duplicate offspring.
4. **Replace:** Use new generation for a further run of algorithm.
5. **Check:** If the end condition is satisfied, stop, and return the best solution in current population.
6. **Loop:** Go to step 2 in loops.

It needs to make clear that the outline of GA shown above is a very general one and there are many things which can be implemented variously according to different kinds of problems.

Several essential questions we need to consider are how to create chromosomes, what type of encoding should we choose, and how to implement the two basic GA operators, crossover and mutation.

Then we need to think about how to deal with the selection of parents for crossover. This can be done in many ways, but the main idea is always to select the better parents since the better parents will more likely produce better offspring. Since making new generations only by new offspring may lose the best individuals from the last generation, elitism is often used. The term "elitism" means that at least one best individual is directly copied without any changes to a new generation, so the best solution which has been found can survive to the end of run. Elitism ensures that the fitness of the best individual in the new generation will never be worse than its parent generation, the worst case is equal.

### Representation for individuals

In genetic algorithms, binary vectors (or binary strings) are used as the typical way of representing chromosomes of individuals that consist of real values. Each real number can be transformed into binary form. The length  $n$  of binary vector is determined by the precision requirement. That is because a  $n$  bits binary vector can only represent  $2^n$  numbers.

For instance, a problem aims at finding  $x$  within the interval  $[1, 2]$  which makes a certain function  $y = f(x)$  get minimum value. The individual or solution to this problem is a real number with precision required to be four digit bits after the decimal point.

According to the precision requirement, the interval  $[1, 2]$  should be equally divided into at least  $10^4$  cells. Since  $8192 = 2^{13} < 10^4 < 2^{14} = 16384$ , so at least 14 bits are required to form a binary vector.

The search space consists of all the binary vectors from  $0000000000000_2$  to  $1111111111111_2$  (the subscript denotes the base number). After obtaining the best individual through genetic algorithm, the solution has to be remapped back into real number. As the binary vectors  $0000000000000_2$  and  $1111111111111_2$  stand for the boundary values 1 and 2 of the interval, respectively. We need to first transform the best solution back into decimal form

$$(b_{13}, b_{12}, \dots, b_0)_2 = \left( \sum_{i=0}^{13} b_i 2^i \right)_{10} = x', \quad (31)$$

then remap it to get the right value

$$x = 1 + x' \cdot \frac{1}{2^{14} - 1}. \quad (32)$$

For instance, if the best individual is  $00010011101011_2$ , then

$$\begin{aligned} x' &= (00010011101011)_2 = 1259_{10} \\ x &= 1 + 1259 \cdot \frac{1}{16384 - 1} = 1.077 \end{aligned} \quad (33)$$

so the best solution is  $x = 1.077$ .

### Fitness function

As mentioned earlier, fitness functions play the role of environments in genetic algorithms. It is an evaluation function which can be used to judge the performance (also called fitness) of individuals. Fitness functions could be in any form, for example, it may stand for the weight of a structure, the distance of a route, the stability of a machine, and the cost of a scheme.

Normally the criterion of judgment is finding the minimum or maximum value of the fitness function. However, sometimes a scaling mechanism is needed to fix the original fitness function in order to make it even more powerful to judge fitness. The most used scaling mechanisms are linear scaling and power law scaling, for example.

### GA operators

Looking through the outline of genetic algorithm, the genetic operators are the most important component of the algorithm. All the new individuals are created by applying these operators to parent individuals. The two classical genetic operators are crossover and mutation, which are both obtained from nature. We will discuss them respectively.

The first genetic operator is called crossover. Simply speaking, crossover selects genes from parent chromosomes, and creates a new offspring. Crossover ensures the mixture of genetic material carried by both parent individuals; it provides the possibility to get better individuals.

There are many ways developed by previous researchers to do the crossover. The simplest way is to randomly choose a position in the chromosome named as a crossover point, and then everything before this crossover point in the new offspring is copied from the first parent while everything after the crossover point is copied from the second parent. Of course the way to do crossover can be very complex. It relies mainly on the encoding of chromosomes.

It needs to be mentioned that specific crossover made for a certain problem could improve the performance of the genetic algorithm dramatically.

When the crossover process is done, mutation occurs. Mutation randomly changes some genes of the new offspring with a probability equals to the mutation ratio. The significance of mutation is to avoid the case where all the solutions in a population fall into a local optimum of the search space. So mutation is necessary for genetic algorithm to find the global optimum. A proper defined mutation operator can help the genetic algorithm find best solution a lot.

### Encoding of GA operators

As indicated before, the means of encoding GA operators are totally based on how the chromosomes are encoded.

Here several common approaches of binary encoding GA operators are given.

#### I. Single point crossover

Single point crossover is also called as simple crossover. Only one crossover point is randomly selected, the binary string from the first bit of chromosome to the crossover point of the offspring is copied from one parent, and the rest is copied from the other. It can be illustrated in the following Figure 3.2.

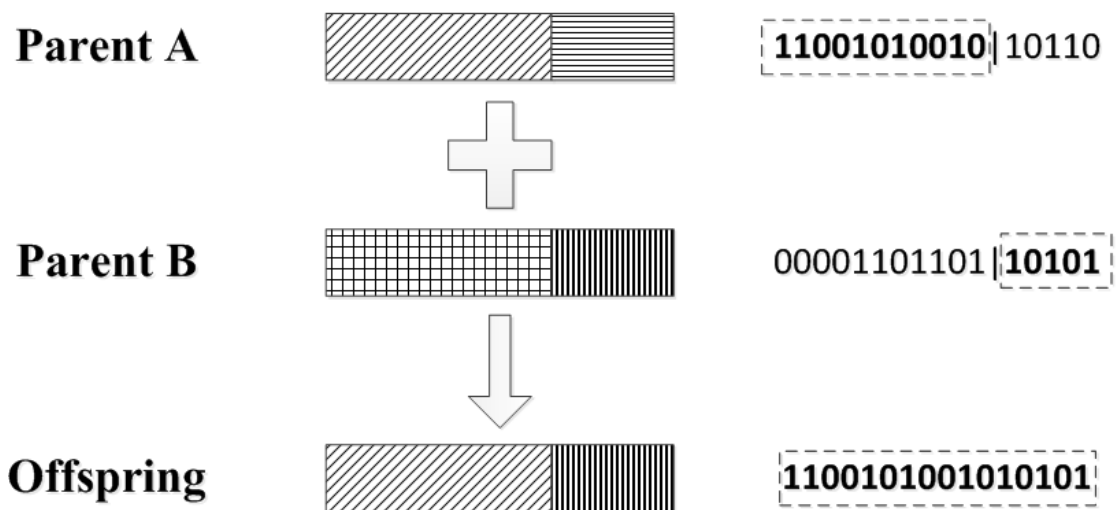


Figure 3.2 Encoding of single point binary crossover.

#### II. Two points crossover

Now, two crossover points are randomly selected, the binary string from the beginning of chromosome to the first crossover point of the offspring is copied from one parent, the part between the two crossover points is copied from the other parent, and the rest is copied from the first parent again. As shown in Figure 3.3 below.

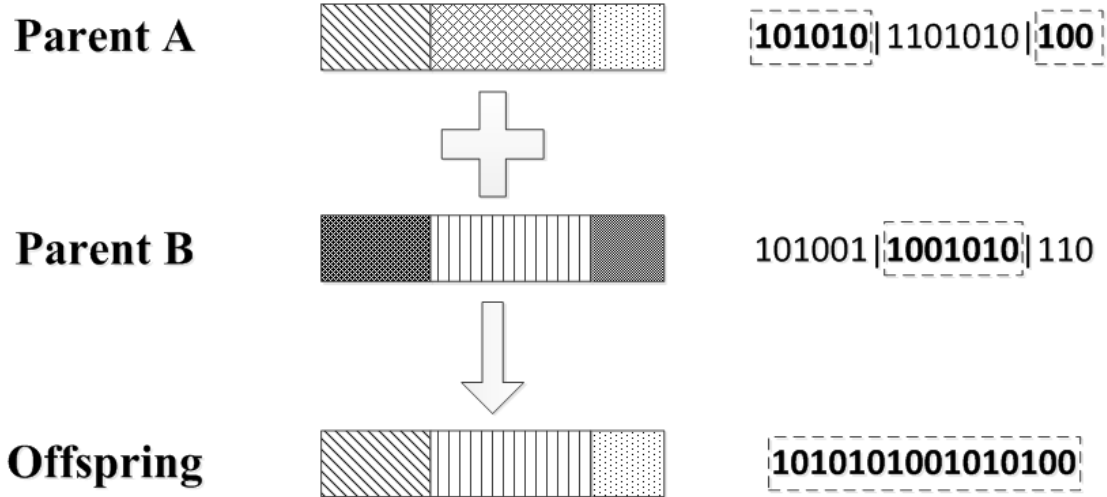


Figure 3.3 Encoding of two points binary crossover.

### III. Uniform crossover

All the bits of the new offspring are randomly copied from either the first parent or the second parent. It can be seen in Figure 3.4.

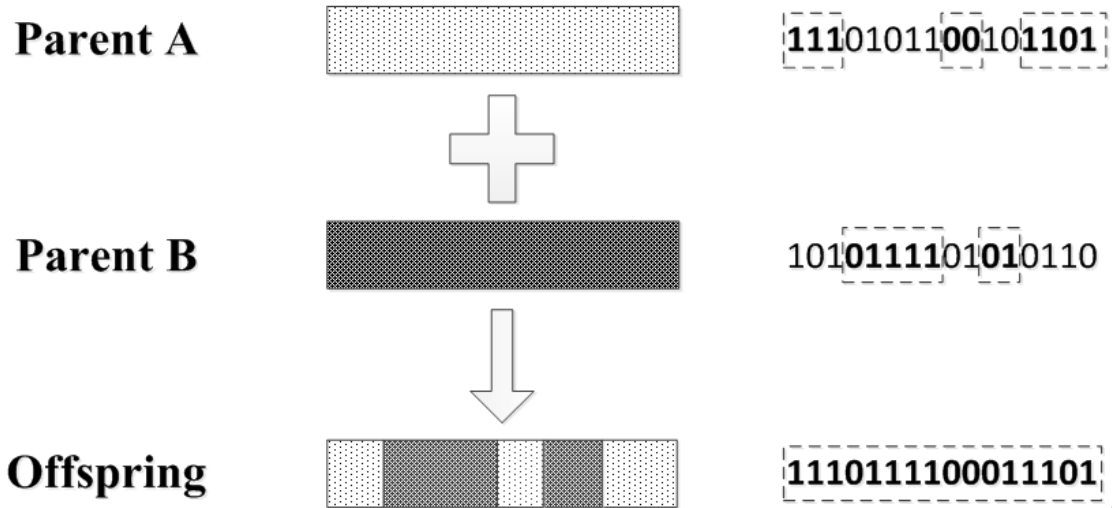


Figure 3.4 Encoding of uniform binary crossover.

### IV. Arithmetic crossover

The new offspring is created by performing some arithmetic operations on the parents. The arithmetic might be logic operations for example (see Figure 3.5).

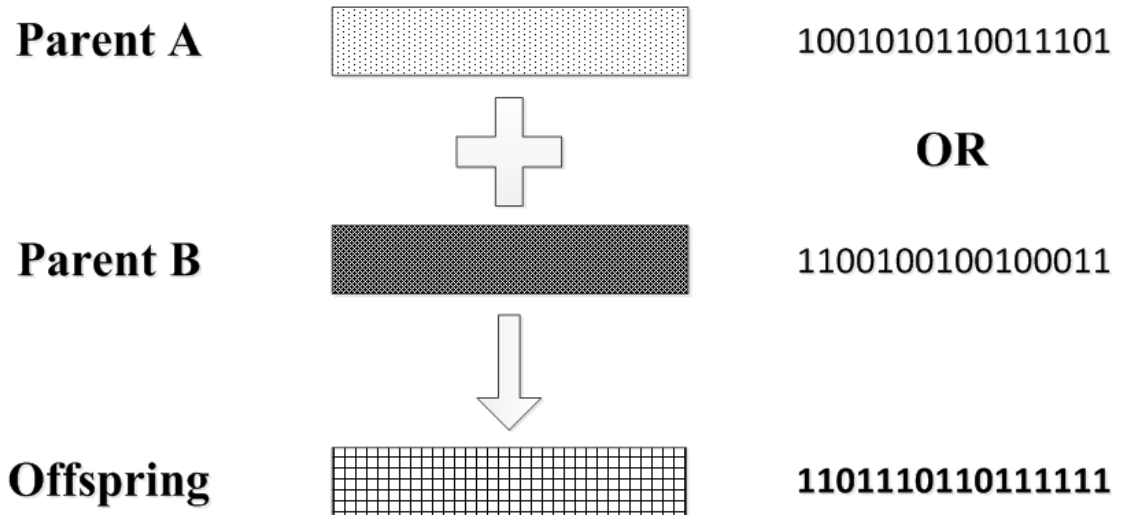


Figure 3.5 Encoding of arithmetic binary crossover.

### V. Encoding of mutation

In binary encoding, mutation is usually implemented by randomly choosing a few bits and switching them from 0 to 1 or from 1 to 0. As shown in Figure 3.6 below:

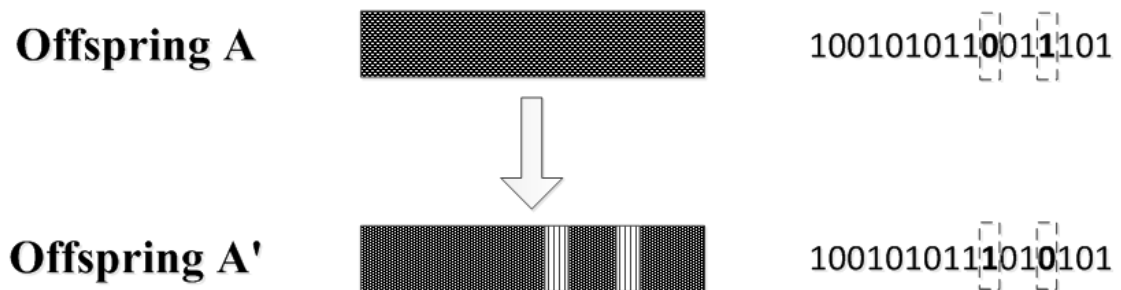


Figure 3.6 Encoding of binary mutation.

### 3.2.2 Combination genetic algorithm (CGA)

From the mathematical point of view, the selection of investigation points (IPs) is a combination problem, which means to select  $m$  elements from total  $n$  elements ( $m \leq n$ ) regardless of the sequences of the selected elements. The selected element set is called a combination, often denoted as  $C_n^m$ . The combination problem has two essential constraints. First of all, all the elements of a combination should belong to the original set, which means the selected element set should be a subset of the whole element set. The second constraint is that all the elements of a combination should be different from each other; in other words, each element can only be selected once.

In order to apply a genetic algorithm to the selection of investigation points, we need to decide how to represent the chromosomes of individuals. It needs to be mentioned that here in our case there is only one chromosome contained in each individual. That is to say, the chromosome is identical to the individual, which is one set of investigation points randomly selected from the whole dataset. Let us check if this case is still suitable for using binary vectors, first.

Assume that there are ten data points in total, which are numbered with 1 to 10 respectively, and we want to select five investigation points from all the data points, which means each individual is a  $C_{10}^5$  combination.

Since  $8 = 2^3 < 10 < 2^4 = 16$ , so at least four bits are required to form a binary representation of a data point. As described above, each individual or solution to this problem should be a combination containing five IPs, so the length of the binary vector which represents one individual must be  $4 \times 5 = 20$  bits.

For instance, if individual A is [2, 3, 4, 5, 7] and individual B is [1, 4, 5, 8, 2], the corresponding binary vectors will be:

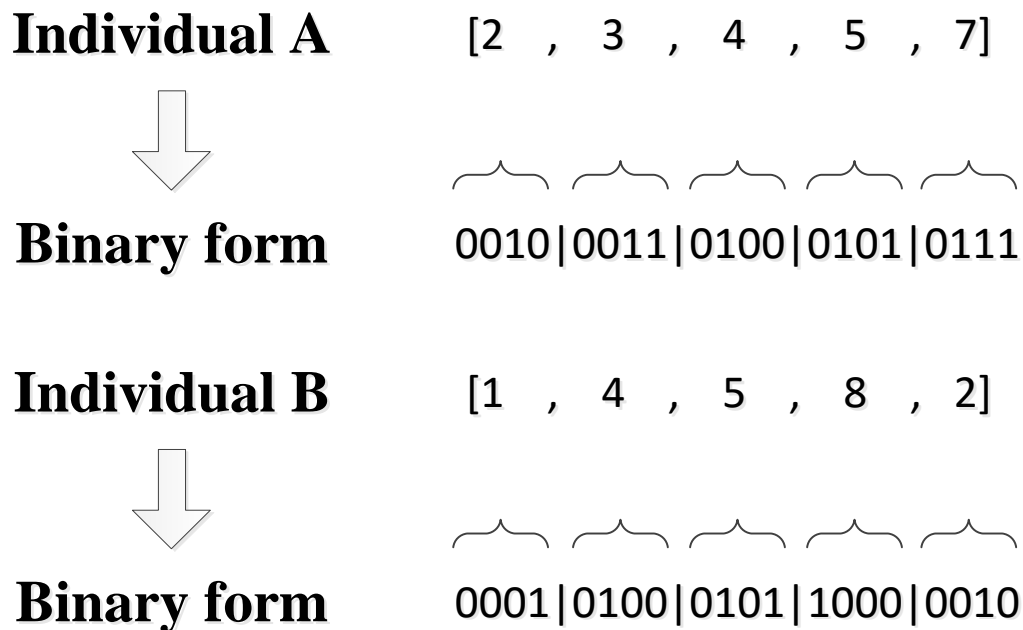


Figure 3.7 Representation of individuals in binary form.

It can be seen from Figure 3.7 that the binary form of the individual A is  $00100011010001010111_2$  and of individual B is  $00010100010110000010_2$ . In the typical GA, then one can directly apply binary crossover and mutation on them to get new legal offspring which are within the range of search space. However, for a combination problem, the binary operations may not be valid by nature.

If we take these two individuals as parents and apply a single point crossover. The po-

sition after the sixth bit is selected as crossover point.

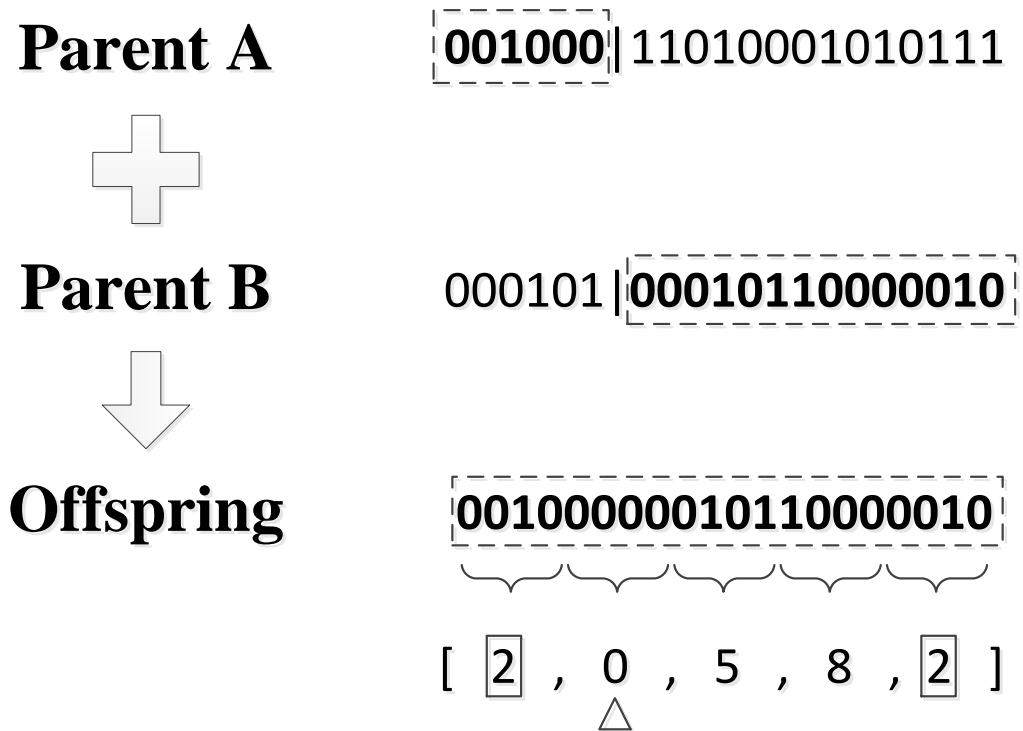


Figure 3.8 Simple binary crossover for the combination problem.

The resulting offspring  $00100000010110000010_2$  corresponding to the combination  $[2, 0, 5, 8, 2]$  is illegal. First, it is not a combination since data point 2 is reduplicate. Second, the binary sequence  $0000_2$  (indicated by  $\triangle$ ) does not belong to the whole dataset. So the resulting offspring is out of the search space.

Similar problems will occur when applying the binary mutation operator.

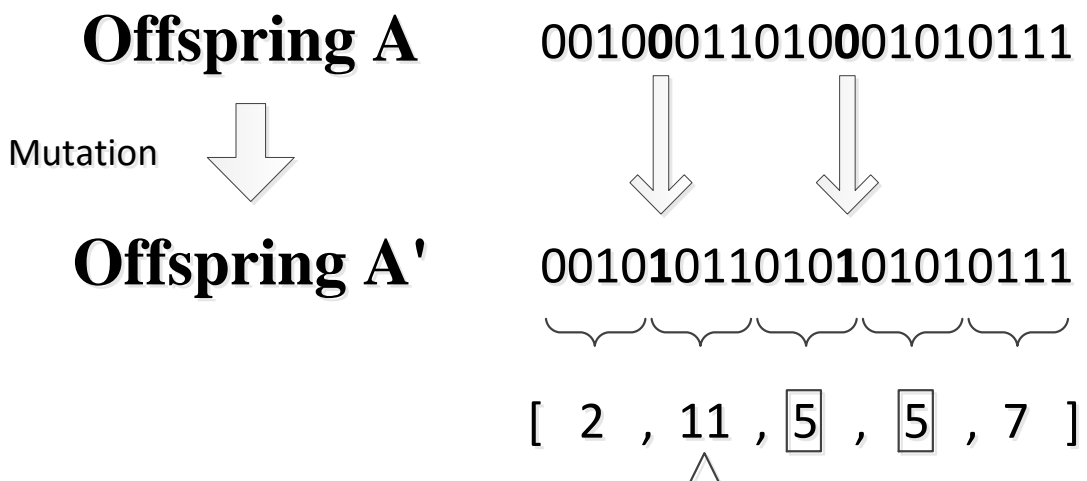


Figure 3.9 Binary mutation for the combination problem.

The resulting new offspring  $001010110101010111_2$  corresponding to the combination  $[2, 11, 5, 5, 7]$  is illegal too. The data point 5 appears twice and data point 11 which does not exist in the whole dataset. Thus for such kind of combination problem the binary encoding of typical genetic algorithms is not suitable.

With the purpose of avoiding getting illegal offspring, either we should use some remedy methods to fix the chromosome in order to make it back into the search space, or one can apply a new way to represent chromosomes.

So instead of using binary vectors, integer vectors are decided to be used for representing individuals for combination problems. That is to say, an integer vector  $[i_1, i_2, \dots, i_k]$  represents a combination  $C_n^k$  containing  $k$  selected investigation points. An individual is now represented as  $[2, 5, 7, 9, 10]$ , for instance. As a consequence, a new type of encoding is needed to implement the crossover and mutation operators, which should be able to handle the integer form of individuals.

### Combination encoding of GA operators

Though there are still two classical genetic operators: crossover and mutation, the combination encoding of them is different from the binary form illustrated in previous sections. It has to make sure that the resulting offspring are legal individuals, that is to say, they are within the search space.

In this work, three different crossover approaches are used in the implementation for selecting investigation points, which are the ‘simple single point crossover’ method, the ‘two points crossover’ method and finally the ‘mixing (or uniform) crossover’ method. (Tropov et al. 2007)

#### I. Simple single point crossover

Similar to single point crossover in binary encoding, one crossover point is randomly selected, the integer string from the first position of chromosome to the crossover point is copied from one parent to the offspring. However, in combination encoding, it has to make sure that there are no duplicate points in the offspring. So in this case, the rest part of offspring cannot be directly copied from the other parent individual. The procedure is done as follows.

The other parent is inspected from the beginning and if a number is not in the offspring yet, it will be added to the offspring. The process will be continued in loops until the required number of investigation points is reached.

It can be illustrated in Figure 3.10, where the crossover point is selected after the third number.



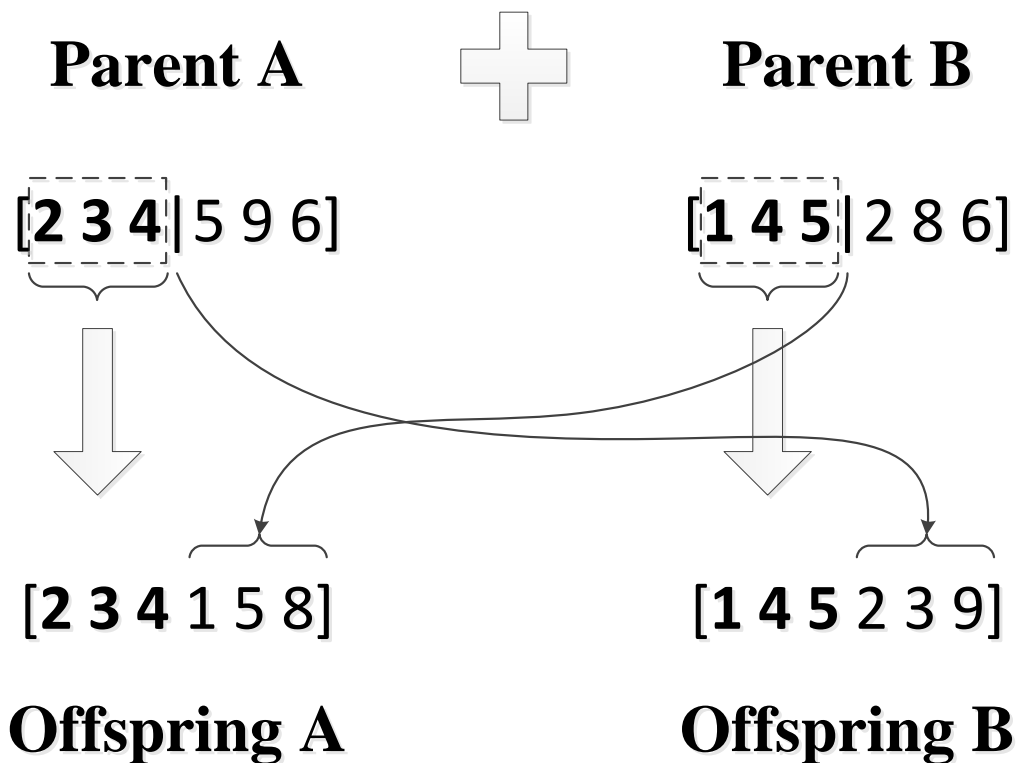


Figure 3.10 Combination encoding of simple crossover.

## II. Two points crossover

It is also similar to the two points crossover in binary coding, two crossover points are randomly selected, the integer string from the beginning of chromosome to the first crossover point and from the second crossover point to the end of the offspring are directly copied from one parent, and the part between the two crossover points is copied from the other parent. The same with the simple crossover, in combination encoding, we must make sure that there are no duplicate points in the offspring. So before adding a number from the other parent to the offspring, we need to inspect whether it has already been contained in the existing part of the offspring. If not, the number will be added. The process will continue again in loops until the required number of investigation points is reached. It can be seen from Figure 3.11 below. The selected two crossover points are after the second and fourth point, respectively.

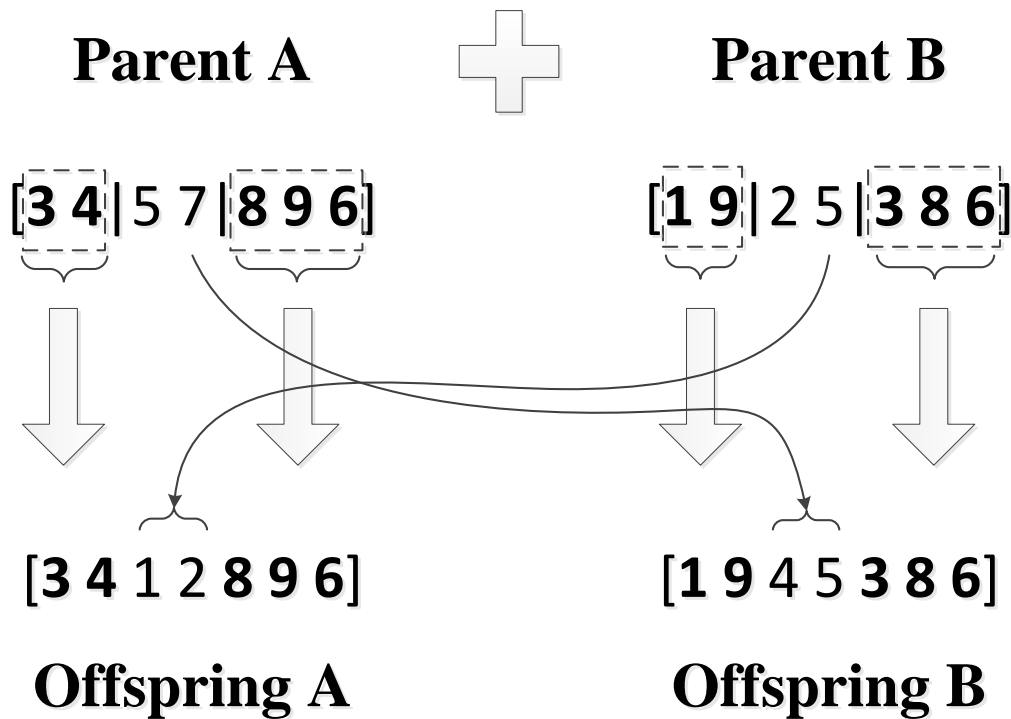


Figure 3.11 Combination encoding of two points crossover.

### III. Mixing crossover

In mixing crossover, all the genes (investigation points) of the offspring are randomly selected from the genes contained in both parents. To do so, we need to firstly create a select pool of all the candidate investigation points that come from both parent individuals, which means to create the union set of all the numbers in two parents. Then the data point is randomly selected from the select pool and put into the offspring one by one until the required number of investigation points is reached. To avoid the duplication in the offspring, each point in the select pool is marked as unavailable after being selected. The whole procedure is illustrated in Figure 3.12.

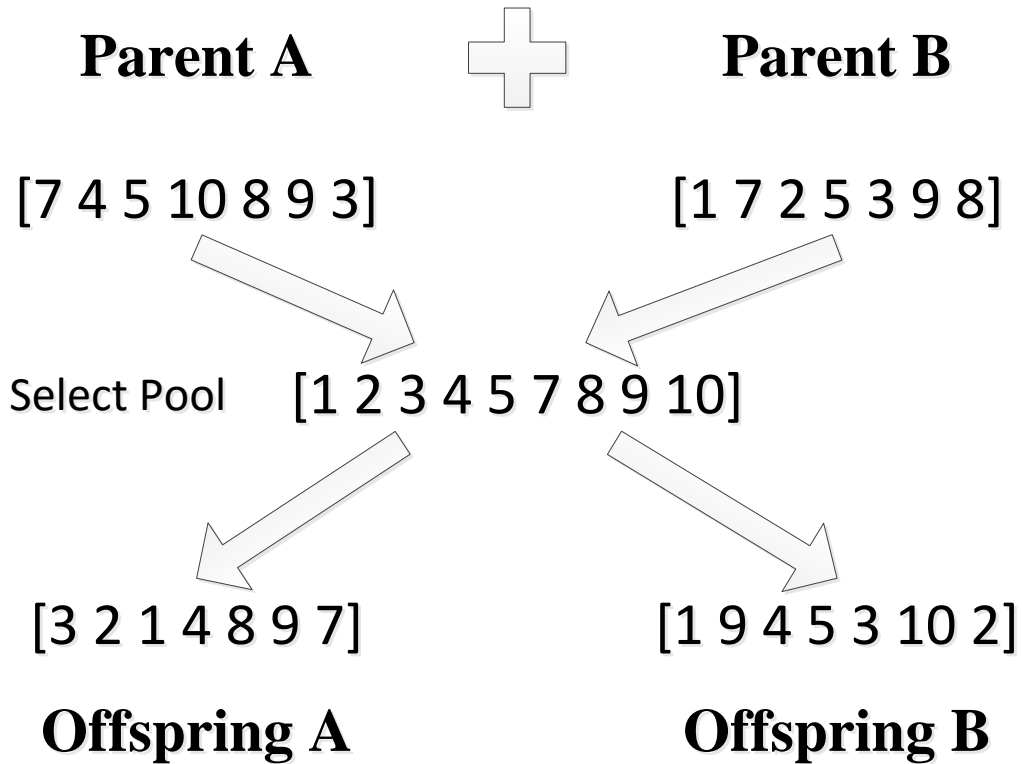


Figure 3.12 Combination encoding of mixing crossover.

#### IV. Mutation

In combination encoding, in order to avoid having duplicate points in the final offspring, the mutation is done as follows. Firstly, a position in the offspring is randomly chosen as the mutation point. Then we delete all the data points that have already been included in the offspring from the whole dataset. After that we randomly select a data point from the remaining dataset, and use it to replace the previous data point at mutation point. In this way, a combination mutation is finished. The process can be seen in Figure 3.13 below, where the mutation point is selected at the fourth position.

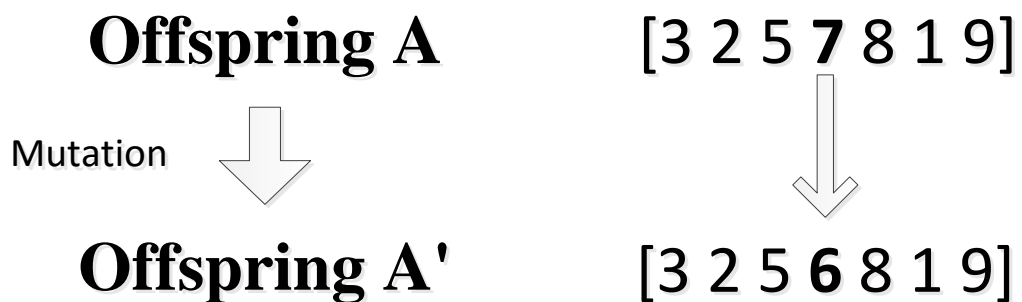


Figure 3.13 Combination encoding of mutation.

### 3.2.3 Weighted uniformly selection of Investigation points (IPs)

For geoscience applications in ground surface deformation fields, what we are most interested in is of course the deformed areas, which means the selected investigation points should reflect the most significant deformations as well as the most significant deformation changes (i.e. the gradient of deformation) contained in the original observation. Besides, the selected set of investigation points should also capture the whole features of the deformation pattern of the original observation as well as possible; in other words, the selected investigation points should distribute somehow uniformly.

Based on these two requirements, the investigation points should be uniformly selected from the observation dataset in general, at the same time concentrating to where large deformations and large deformation changes occurred.

As mentioned before, this problem is a combination problem. Therefore, integer vectors are used to represent the chromosome of individuals. More specifically, each individual in our case is a combination  $C_n^m$ , which stands for selecting  $m$  investigation points from total  $n$  observed data points. In coding, we set an ID number to all the observation data points, and these ID numbers are used as the elements of the integer vectors to distinguish each data point.

To meet the two requirements of investigation points, we created a specified fitness function which is based on a simple physical analogy.

Let's illustrate it with an example of charged balls.

Assuming that we have a large empty cube; many small balls with positive electric charge are thrown into the cube. Because of the like charge, all these small balls exert repelling forces on each other. Furthermore, each position in the cube has a small charger, which contains different amount of electrons that can influence the balls' quantity of electric charge. In general, the more electrons the charger has, the less quantity of electric charge the ball at this position will have, and thus the smaller repelling forces it will exert on other balls. The amount of electrons contained in the chargers at each position is constant. Therefore, the whole system has some kind of potential energy.

When all the balls are released from their initial positions, they will move. And they will not stop moving until the repelling forces among each other reach the equilibrium. At that moment, the stored potential energy (here is electric potential energy) of the whole system has the minimum value. The magnitude of repelling forces is inversely proportional to the square of the distance between the charged balls multiplied by the sum of weights (the influences due to the electrons contained in the chargers) at the positions where the charged balls are.

Minimizing the function

$$\min \mathbf{U} = \min \sum_{p=1}^m \sum_{q=p+1}^m \frac{1}{w_{pq}} \cdot \frac{1}{L_{pq}^2} \quad (34)$$

will give a system of balls which are distributed weighted uniformly in the cube. The function above is used as the fitness function, where  $U$  stands for the potential energy of the whole system,  $w_{pq}$ , the sum of weights at the positions where the charged ball  $p$  and  $q$  are, and  $L_{pq}$ , the distance between charged ball  $p$  and  $q$ .

This fitness function we used to evaluate the fitness of all the potential solutions to the selecting IPs problem is a modified version of the Audze-Eglais objective function (Audze and Eglais 1977), which takes different weights of the balls into account. Here in our case,  $L_{pq}$  stands for the distance between data point  $p$  and  $q$ , and the sum of weights  $w_{pq}$  is equal to the sum of  $w_p$  (weight of data point  $p$ ) and  $w_q$  (weight of data point  $q$ ).

The weight of each data point  $i$  is calculated as follows. Assuming the surface deformation field can be represented by a function  $F(x, y)$ , then the second gradient of  $F$  at the data point  $i$  can be written as

$$\nabla^2 F = \left( \begin{array}{cc} \frac{\partial^2 F}{\partial x \partial x} & \frac{\partial^2 F}{\partial x \partial y} \\ \frac{\partial^2 F}{\partial y \partial x} & \frac{\partial^2 F}{\partial y \partial y} \end{array} \right) \Big|_{x_i, y_i} \quad (35)$$

and so the weight of the data point  $i$  is defined as

$$w_i = \sqrt{|\det(\nabla^2 F)|}. \quad (36)$$

We can use a synthetic example to explain how this method works. If the whole set of observation data points are like the one shown in Figure 3.14, based on the calculated weights (see Figure 3.15), the final distribution of selected investigation points (denoted by blue circles) will look like the one shown in Figure 3.16. And in Figure 3.17, we plot the uniformly selected IPs without considering the gradient as different weight. Compared it with Figure 3.16, we can clearly see that including different weights in selection allows us to have more points selected from the important deformation area and the distribution of resulting IPs can capture the characteristics of the original deformation pattern much better.

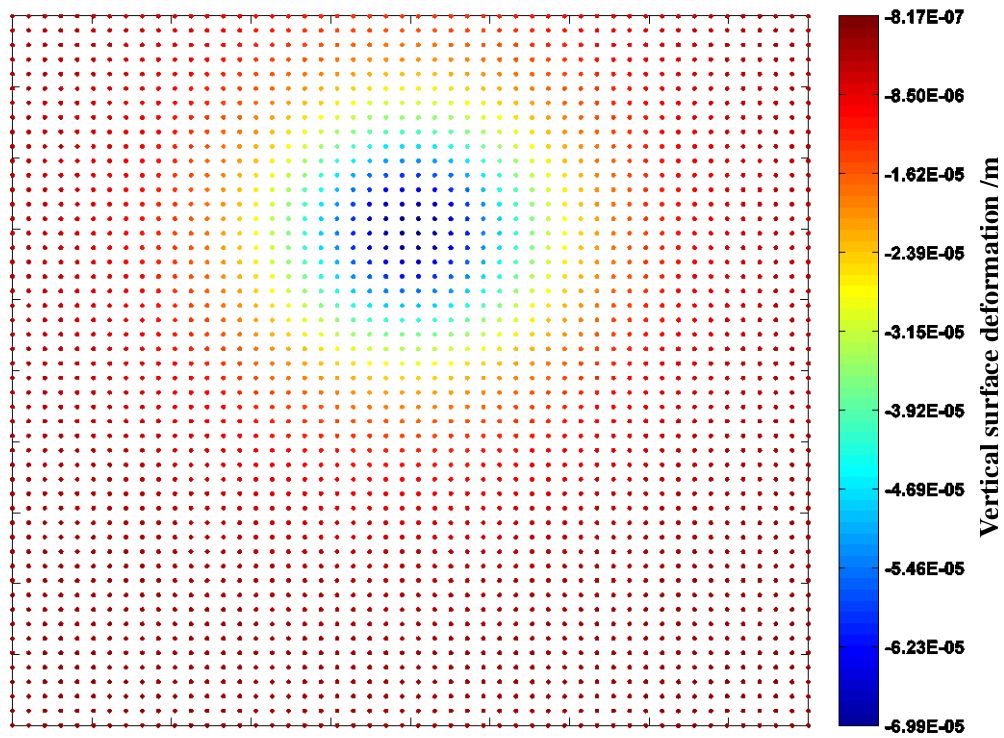


Figure 3.14 The whole set of observation data points of the synthetic example.

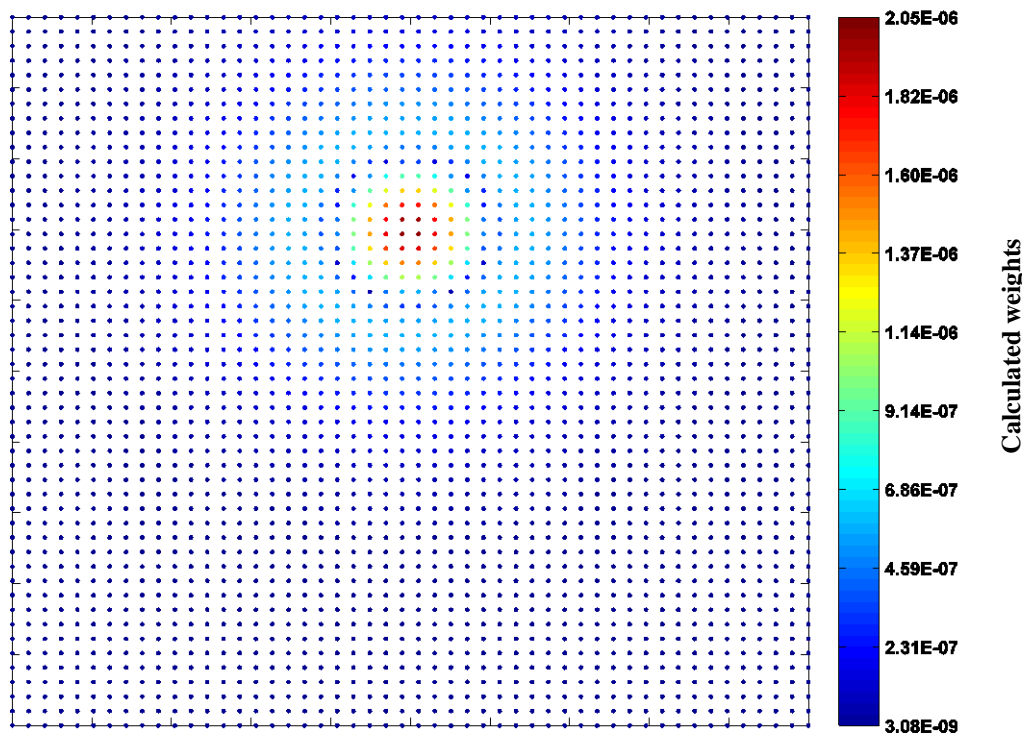


Figure 3.15 The calculated weights for each data points of the synthetic example.

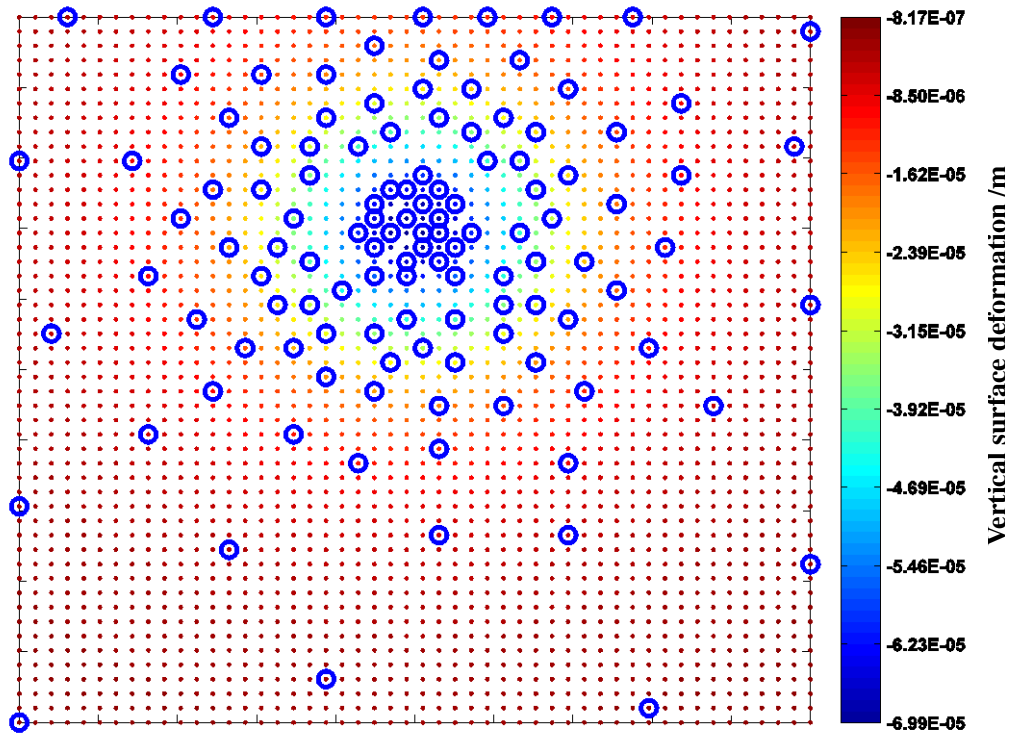


Figure 3.16 Weighted uniformly selected investigation points (blue circles) in the whole set of data points.

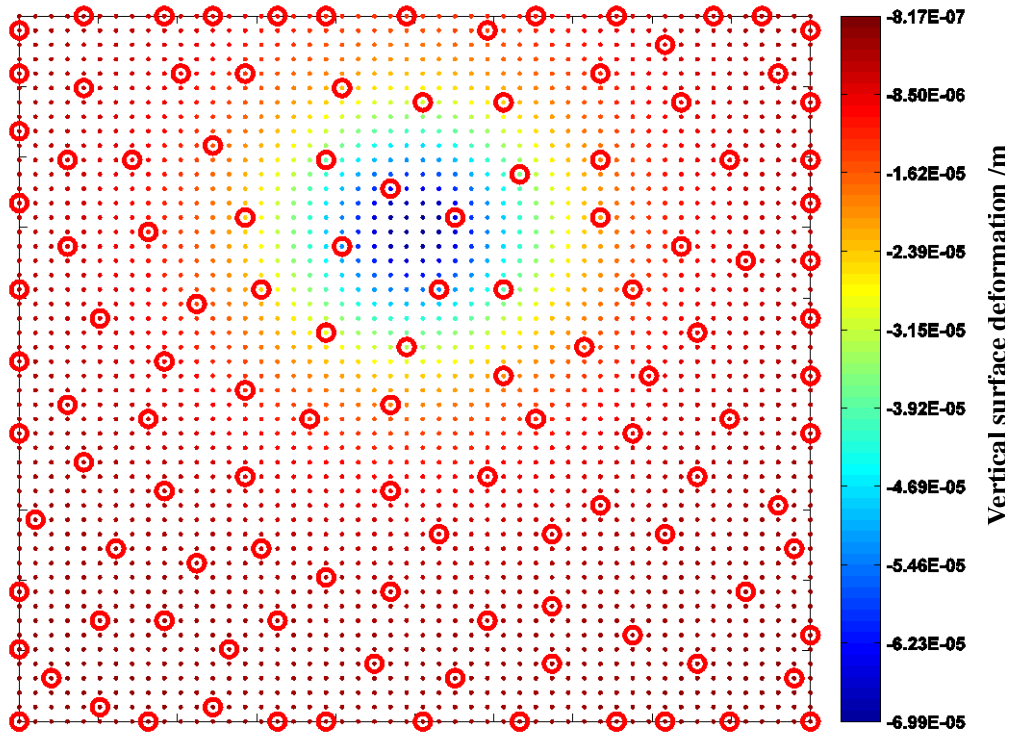


Figure 3.17 Uniformly selected investigation points (red circles) without considering weights in the whole set of data points.

In the example shown above, the whole dataset contains 2500 data points in total and 120 investigation points are selected. The color codes in the figures represent the vertical deformation of each point.



## Chapter 4

### Analytical Geophysical Models

---

This chapter is dedicated to several analytical geophysical models which are typical and have been widely applied in the literature by many geophysicists all over the world. In the first section, it starts with a brief introduction to the Earth's internal structure. Then a couple of famous volcano deformation source models are presented and some related issues such as tradeoff between parameters are discussed in detail. At last, we will discuss in general the drawbacks and shortcomings of the analytical geophysical models.

#### 4.1 Volcano deformation source models

##### 4.1.1 Structure of Earth's interior

As is well known, the Earth is a terrestrial planet, which also is a very complicated multi-physical system. The interior structure of the Earth can be divided into different layers either by its chemical (compositional) properties, or based on the rheological (mechanical) properties. Chemically, the Earth can be roughly divided into three major layers: crust, mantle and core, moreover, the crust can be further classified as oceanic crust or continental crust. The crust varies in thickness from very thin oceanic crust (about 5 km) up to typical continental crust (20~50 km), and it can reach about 65 km thick under high mountains. The boundary between crust and mantle is known as Mohorovičić discontinuity or Moho for short, named after the famous Yugoslav seismologist in 1909. As material changes, the density increases from crust to the core. The crust is principally made of less dense rock, such as granite (~2700 kg/m<sup>3</sup>) and basalt (~3000 kg/m<sup>3</sup>), while the mantle consists of denser rock like peridotite (~3400 kg/m<sup>3</sup>). The core of the Earth has a very high density (10000~13000 kg/m<sup>3</sup>), which indicates it is a composition of metals. (Press and Siever 1994)

Rheologically, the interior of the Earth consists of five layers: lithosphere, asthenosphere, mesosphere, outer core and inner core, which are distinguished by measuring the speed of seismic waves. The crust and part of the upper mantle together form the lithosphere, which is the rigid strong outer layer of the Earth ranges from about 10 to 200 km thick and remains elastic behavior for a long period of geologic time. Beneath it is the asthenosphere, a much weaker layer of the upper mantle, whose temperature can reach 1100~1200 °C. Due to the high temperature and relatively low pressure in this layer, rock is ductile, and so the asthenosphere has a relatively low viscosity (10<sup>19</sup>~10<sup>24</sup> Pa·s). (Walzer et

al. 2003) Therefore, it behaves like Silly Putty<sup>®</sup>, which deforms as an elastic solid in short term but as a viscous fluid during a long period of time. Although the asthenosphere can flow, it is worth pointing out that it is not liquid since both P-wave and S-wave can travel through it. As the depth increases, pressure is getting higher and higher. At the depth of 660 km (Jordan 1979), the pressure is so high that it forces the rocks into a denser and more rigid structure, mainly the magnesium silicate olivine is transformed in spinel. In mesosphere, the mantle cannot flow. The outer core of the Earth is nothing but a ~2200 km thick liquid layer of molten metals surrounding the solid inner core. (Press and Siever 1994)

Generally speaking, among all the layers most of volcanism primarily relates to the lithosphere and asthenosphere. In this thesis we limit our study to magmatism within the crust.

### **4.1.2 Elastic half-space**

In order to approximate the ground deformation and better understand the underlying mechanism of volcanic activity, many different analytical models have been developed. And due to the complexity of the Earth's structure and composition, all the analytical models require plenty of assumptions and simplifications. As mentioned above, the Earth's lithosphere behaves elastically. Therefore, many analytical models describe the lithosphere as an ideal semi-infinite elastic body, also called an elastic half-space. By definition, the half-space has only one free surface, and extends to infinity in all other directions. The material of the half-space is assumed to be homogenous and isotropic; furthermore, it also obeys the Hook's law, which means the strain and stress have a linear relationship.

To describe the stress-strain constitutive relation of such material, two independent constants are demanded. Here in this thesis, the Poisson's ratio  $\nu$  and shear modulus  $G$  are adopted, since these two constants are commonly used in volcanic source models. And of course, we could choose the Poisson's ratio  $\nu$  and Young's modulus  $E$  or other combinations as well, which is just a matter of convenience.

The typical  $G$  value for the Earth's crust is in the range of 1 GPa to 100 GPa. Seismologists usually take 60~70 GPa as the suitable  $G$  value, which is determined by the velocity of seismic waves. However, volcanologists tend to use smaller  $G$  value like 30~40 GPa, because in general rocks in volcanic areas are much weaker than normal due to hydrothermal alteration and fracturing. There are also results of laboratory testing which show that rocks may have a very low shear modulus around 1~2 GPa (Davis et al. 1974, Apuani et al. 2005b).

The value of Poisson's ratio  $\nu$  obtained by laboratory experiments on intact crustal rocks is in the range of 0.15 to 0.30, and it is usual to assume  $\nu$  is equal to 0.25 (or  $\lambda = G$ , where  $\lambda$  is the Lamé's first parameter) for the sake of convenience, since it simplifies significantly the mathematical solution. (Segall 2010)

Although the elastic half-space assumption ignores many features of the Earth, it can successfully provide a first order approximation of the surface deformation caused by short-term volcanic activities.

### 4.1.3 Spherical and spheroidal sources

The first and simplest source model is a point pressure source, which is also known as the Mogi model after the prominent Japanese seismologist Kiyoo Mogi (1958). The Mogi model represents a magma chamber as a fluid-pressurized spherical cavity whose radius is much smaller than its depth ( $a \ll d$ ) embedded in an elastic half-space (see Figure 4.1).

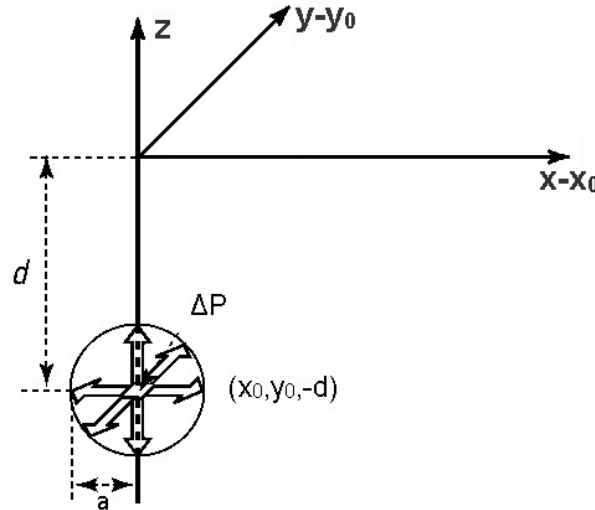


Figure 4.1 Coordinate system and parameter definition of point pressure source. (Mogi 1958)

The surface displacements induced by such a Mogi source are given by:

$$\begin{pmatrix} U_x \\ U_y \\ U_z \end{pmatrix} = a^3 \Delta P \frac{(1-\nu)}{G} \begin{pmatrix} \frac{x-x_0}{R^3} \\ \frac{y-y_0}{R^3} \\ \frac{d}{R^3} \end{pmatrix} \quad (37)$$

where  $U_x, U_y, U_z$  are three components of the displacement vector at the point  $(x, y, 0)$ , the center of the source is at  $(x_0, y_0, -d)$ ,  $a$  the radius of the cavity,  $\Delta P$  the pressure change in the source, and  $R = \sqrt{(x-x_0)^2 + (y-y_0)^2 + d^2}$  the distance from the center of the source to the point on the free surface.

From the formulation above, we can see there is a tradeoff between the radius  $a$  of the Mogi source and the pressure change  $\Delta P$ . In other words, a small source with large pressure change can produce the same surface displacements as a large source with small pressure change. Therefore, it is common to combine  $a$  with  $\Delta P$  to form a new parameter

usually termed as "source strength". And the Mogi model, in total, has four independent parameters, three for the location plus the source strength.

In order to be able to get the estimates of the radius and pressure change separately, McTigue (1987) modified the Mogi model expressions by adding higher order correlation terms. This kind of source model represents the surface deformation induced by a finite spherical source embedded in an elastic half-space. The corresponding surface displacements are given by:

$$\begin{pmatrix} U_x \\ U_y \\ U_z \end{pmatrix} = \left( a^3 \Delta P \frac{(1-\nu)}{G} \left( 1 + \left( \frac{a}{d} \right)^3 \left( \frac{(1+\nu)}{2(5\nu-7)} + \frac{15d^2(\nu-2)}{4R^2(5\nu-7)} \right) \right) \right) \begin{pmatrix} \frac{x-x_0}{R^3} \\ \frac{y-y_0}{R^3} \\ \frac{d}{R^3} \end{pmatrix} \quad (38)$$

where all the symbols are the same as in Equation (37).

Since the high order correlation terms have a factor  $(a/d)^3$ , it affects the surface displacements significantly only when the radius of the source  $a$  is similar to its depth  $d$  (i.e.  $0.2 \leq (a/d) < 1$ ). When the depth of the source is larger than ten times of its radius, the McTigue model will give nearly the same results of surface deformation as the Mogi model. Figure 4.2 shows the comparison of surface deformation fields generated by Mogi and McTigue source model with different radius to depth ratio  $(a/d)$ . In the figure, the distance is in unit of source depth  $d$  and the displacements are normalized by  $a^3 \Delta P (1-\nu) / G d^2$ , the maximum vertical displacement of Mogi model, for convenience.

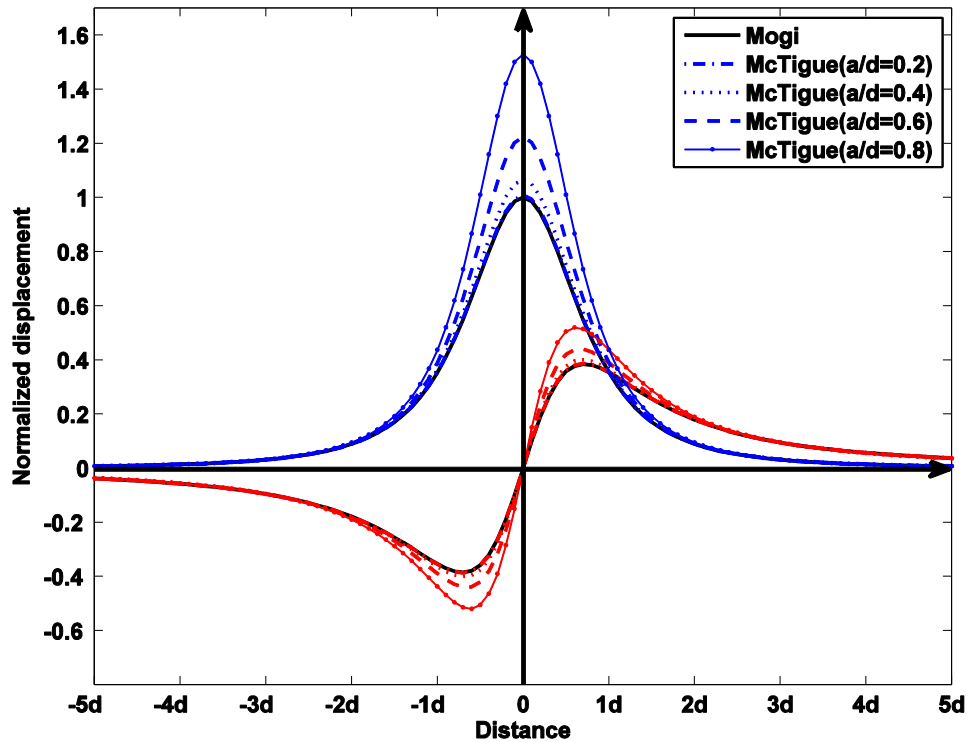


Figure 4.2 Profiles of normalized axisymmetric horizontal (red) and vertical (blue) displacements generated by Mogi and McTigue source.

The McTigue model can be considered to have five independent parameters: three for source location, radius of the source and the pressure change in the source. However, it is better to look at the source strength since the radius and pressure change are not fully separated and there still are some tradeoffs between them. The tradeoffs between model parameters are discussed in detail later in this chapter.

It is obvious to see that both the point and finite spherical source model will produce a symmetric deformation field. Since most of the data sets obtained from volcanic areas in the world usually show asymmetric deformation patterns, a more generalized model is required to better describe them (Segall 2010). To meet the needs, Davis and Yang (Yang et al. 1988) further extended the Mogi source model to a model with a dipping finite prolate spheroidal source, also known as Yang's model. There are eight parameters used in Yang's model, which include the semi-major,  $a$ , and semi-minor axis,  $b$ , the location of source center,  $(x_0, y_0, -d)$ , the pressure change of the source  $\Delta P$ , the dipping angle  $\theta$  and the strike angle  $\phi$ . The definition of these parameters and coordinate system used to derive the surface displacement fields are shown in Figure 4.3.

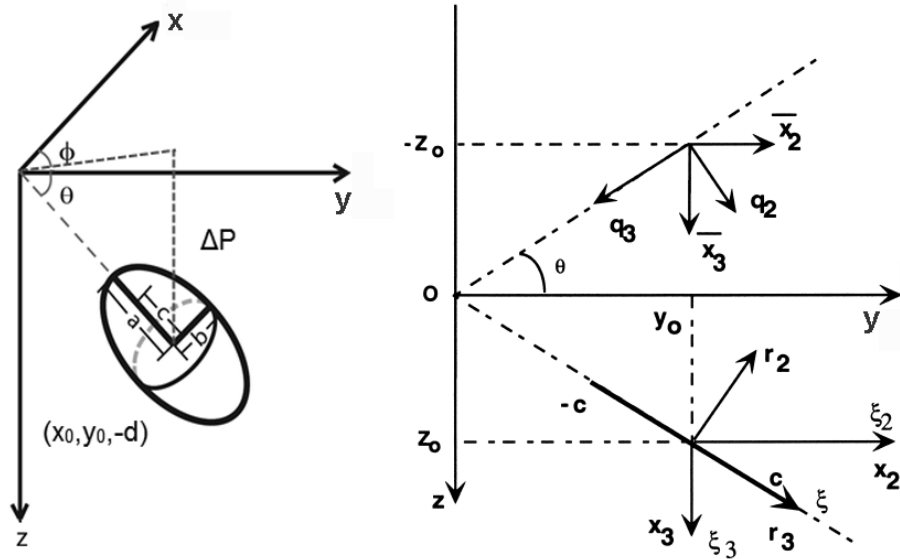
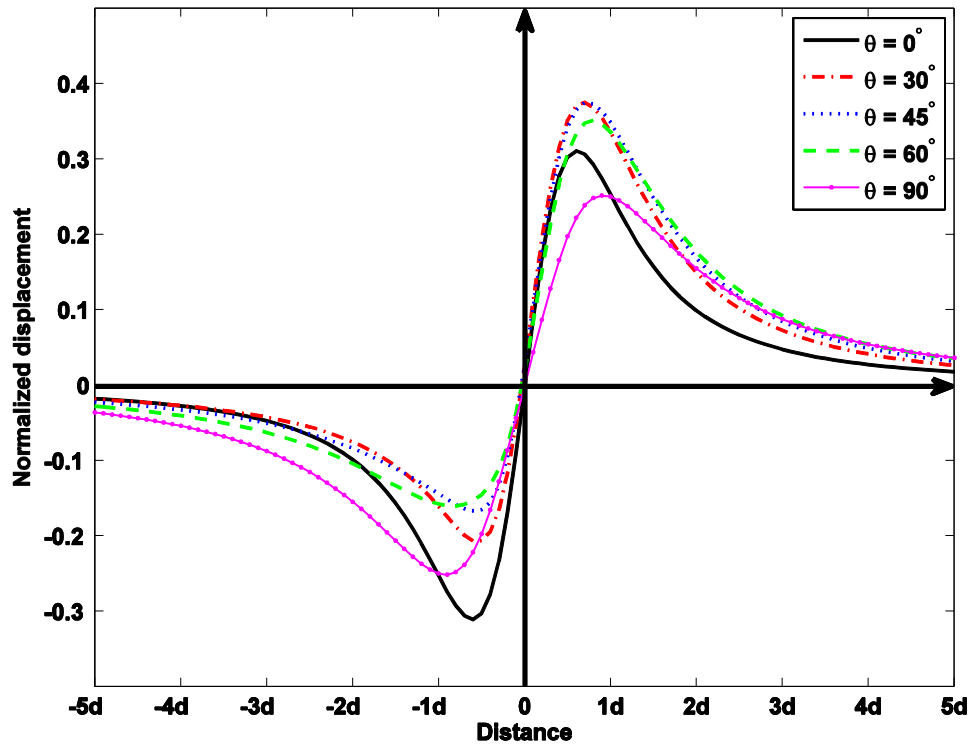


Figure 4.3 Coordinate system and parameter definition of Yang's model. (Yang et al. 1988)

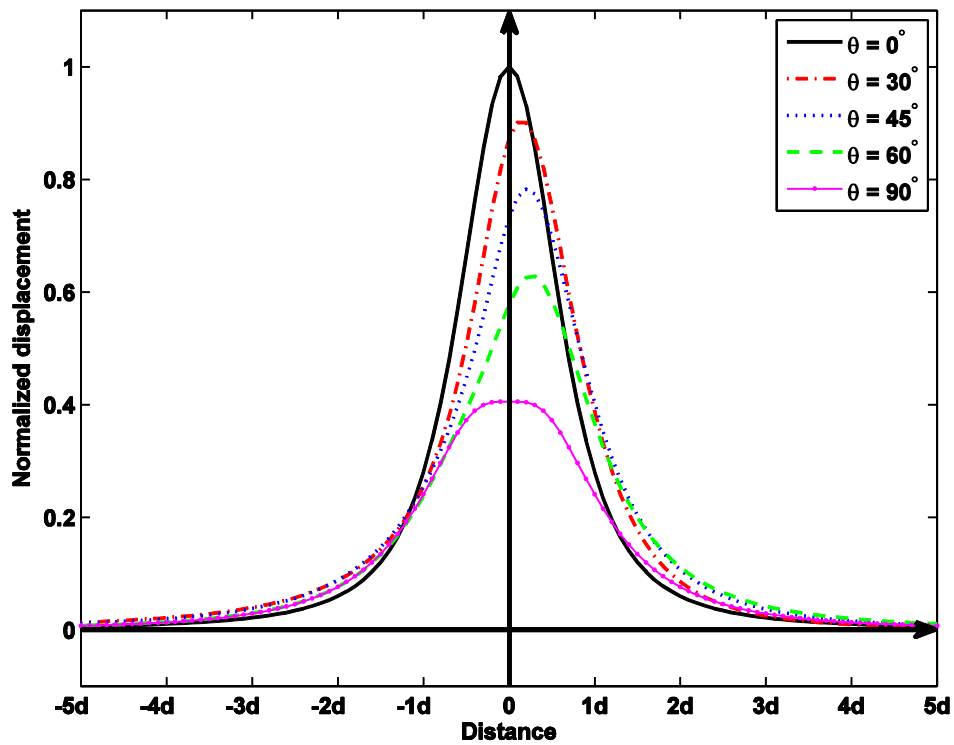
As Yang addressed in his paper, the deformation fields of such a dipping finite prolate spheroidal source embedded in an elastic full-space is equivalent to that generated by a parabolic distribution of double forces and centers of dilatation between the spheroid foci. By applying Mindlin's point force solutions, a half-space solution of deformation fields can be obtained. It is the principal idea of deriving Yang's model.

In order to avoid redundancy, we do not provide the detailed mathematical expressions of Yang's model here in this thesis. The detailed analytic solution can be found in the reference paper (Yang et al. 1988), and a correction to it was defined by Newman in the appendix of his paper (Newman et al. 2006). A further correction was found as part of our work and validated via comparing the analytic solutions with the finite element models for the same parameters. The detailed form of the correction can be found in Appendix 1.

Figure 4.4 illustrates the surface displacement fields generated by the Yang's model with different dipping angles ( $\theta = 0^\circ, 30^\circ, 45^\circ, 60^\circ$  and  $90^\circ$ ). The horizontal (Figure 4.4a) and vertical (Figure 4.4b) displacements plotted in the diagrams are in the vertical plane which contains the major axis of the spheroid. The origin in the figures is moved to  $(x_0, y_0, 0)$ , and other parameters are  $a = 1.0$  km,  $b = 0.5$  km,  $d = 3$  km and  $\Delta P = 10^7$  Pa. The material properties are assumed to be constant, which are shear modulus  $G = 40$  GPa and Poisson's ratio  $\nu = 0.25$ . The distance is still in units of source depth and all the displacements are normalized by the maximum vertical displacement generated by the prolate spheroid with dipping angle  $\theta = 0^\circ$  for convenience. It is obvious to see that when the prolate spheroid is horizontally or vertically embedded, the corresponding surface displacements are symmetric; otherwise, both the vertical and horizontal displacement fields are skewed to the down-dip direction where the spheroid dips.



(a)



(b)

Figure 4.4 Normalized surface displacement fields generated by the Yang's model. (a). Horizontal displacement; (b). Vertical displacement.

If the dipping angle is  $90^\circ$  and the minor axis of the prolate spheroid is much smaller than its major axis, the Yang's model degenerated into a closed pipe model, also known as cigar model (see Figure 4.5), given by Bonaccorso and Davis (1999).

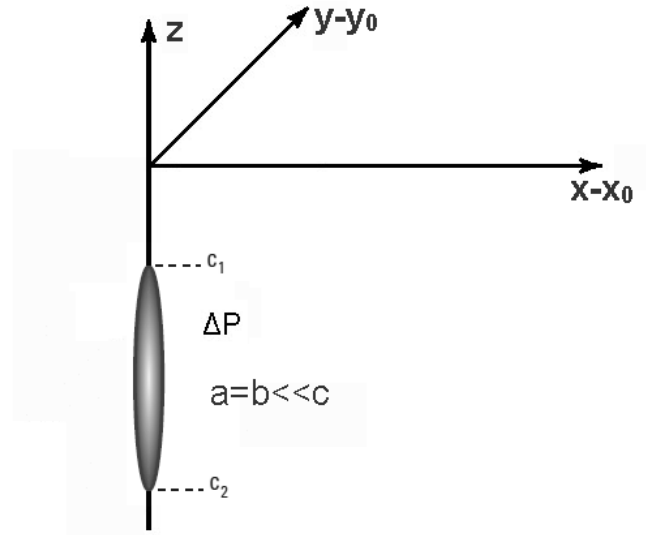


Figure 4.5 Coordinate system and parameter definition of cigar-shaped source model (Dzurisin 2007)

The closed pipe model is used for modeling cigar-shaped magma chambers or plugged conduits. Like the Yang's model, the solution of a closed pipe model also consists of two terms: an integral of a line of dilatations and a line of vertical double forces. The surface displacements generated by a closed pipe model are given by:

$$\begin{aligned}
 U_x &= \frac{a^2 \Delta P}{4G} \left( \frac{c_1^3}{R_1^3} + \frac{2c_1(5\nu - 3)}{R_1} - \frac{2c_2(5\nu - 3)}{R_2} - \frac{c_2^3}{R_2^3} \right) \frac{x - x_0}{r^2} \\
 U_y &= \frac{a^2 \Delta P}{4G} \left( \frac{c_1^3}{R_1^3} + \frac{2c_1(5\nu - 3)}{R_1} - \frac{2c_2(5\nu - 3)}{R_2} - \frac{c_2^3}{R_2^3} \right) \frac{y - y_0}{r^2} \\
 U_z &= -\frac{a^2 \Delta P}{4G} \left( \frac{10\nu - 3}{R_1} - \frac{10\nu - 3}{R_2} + \frac{r^2}{R_2^3} - \frac{r^2}{R_1^3} \right)
 \end{aligned} \tag{39}$$

where  $a$  is the semi-minor axis of the degenerated spheroid,  $c_1$  and  $c_2$  the depths of the top and bottom of the pipe, respectively,  $r = \sqrt{(x - x_0)^2 + (y - y_0)^2}$  the horizontal distance from the source, and  $R_1 = \sqrt{r^2 + c_1^2}$  and  $R_2 = \sqrt{r^2 + c_2^2}$  the distances from the top and bottom of the pipe to a point on the free surface. Other symbols are the same as in Equation (37).



The horizontal (red) and vertical (blue) surface displacements produced by a cigar model are shown in Figure 4.6. The origin in the plot is moved to  $(x_0, y_0, 0)$ . All the displacements are normalized by  $a^2 \Delta P / 4Gc_1$ , the source strength multiplied by the inverse of the top depth of the source, and the distance is in unit of top depth. It has been found that the change of Poisson's ratio has a significant impact on the near-field surface displacements.

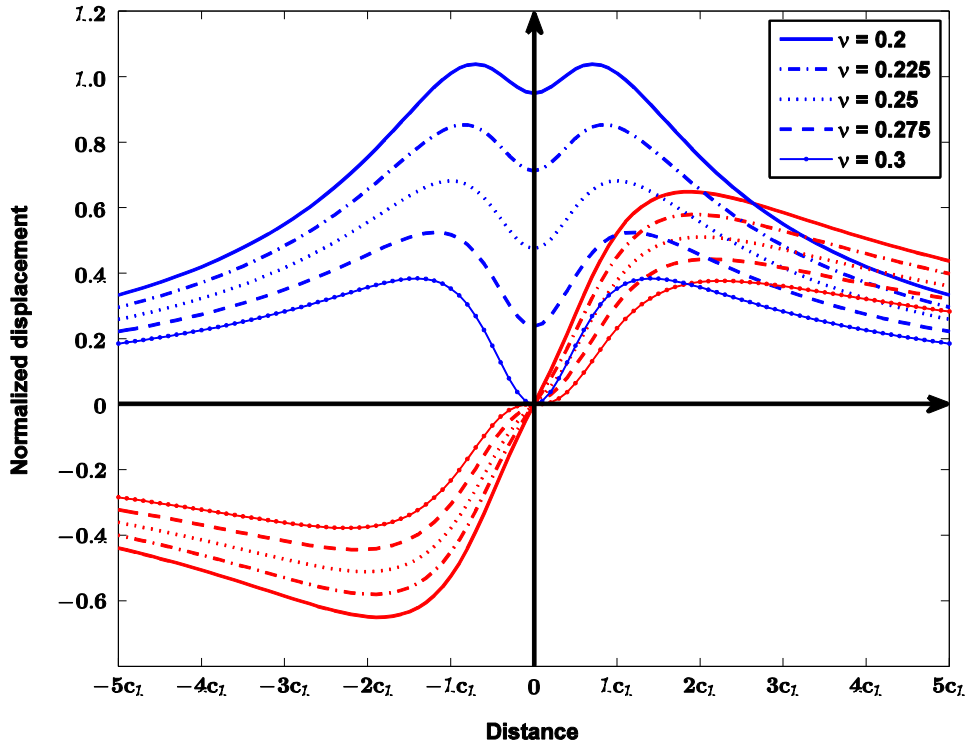


Figure 4.6 Normalized surface displacements generated by a closed pipe model with different Poisson's ratio.

If we consider the Poisson's ratio  $\nu$  as a constant, then the closed pipe model has six parameters. But from the Equation (39) we can see, like the Mogi model, there is also a tradeoff between the semi-minor axis  $a$  and pressure change  $\Delta P$ , so it is better to use source strength instead of  $a$  and  $\Delta P$  as an independent parameter. Thus, only five independent parameters are left, which are  $(x_0, y_0)$  for the horizontal location of the pipe, the top and bottom depth of the pipe  $c_1$  and  $c_2$ , and the source strength. Since the bottom depth  $c_2$  slightly affects only the far-field surface displacements, it can be set to infinity in some cases for convenience. The parameters used here to plot Figure 4.6 are  $a = 0.025$  km,  $c_1 = 2$  km,  $c_2 = 40$  km and  $\Delta P = 3 \times 10^6$  Pa.

Apart from all the models mentioned above, there are other kinds of source models used to represent inflating and deflating magma chambers, like ellipsoidal source model (Eshelby 1959, Davis 1986), oblate spheroidal source model (Fialko et al. 2001), etc., which are not discussed here in detail.

#### 4.1.4 Dipping point and finite rectangular tension cracks

Another class of volcano deformation source models is used to represent tabular intrusions such as sills and dikes. By definition, a sill is a tabular intrusive layer of igneous rock which is normally parallel to the layered rock beds. In contrast, a dike is a narrow tabular body of rock which is perpendicular to the layering (see Figure 4.7). The width of a dike can range from a few centimeters to several meters, and its length can be up to several kilometers.

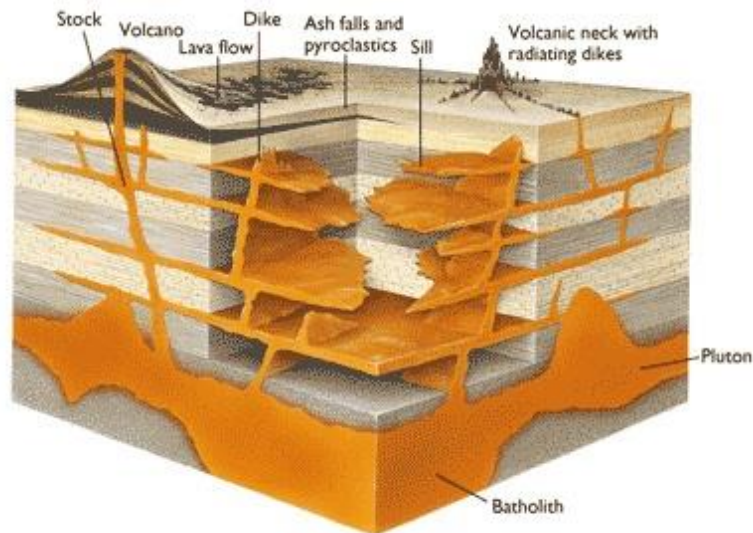


Figure 4.7 Cross-sectional view of sills and dikes. (Press and Siever 1994)

In general, such kind of tabular intrusions can be represented by dipping point and finite rectangular tensile cracks. Under certain circumstances, such as deep sill-like magma chambers, they can be represented by other simplified models like finite pressurized horizontal penny-shaped cracks, for example. Here we use the general form of solutions given by Okada (Okada 1985, Okada 1992) to calculate the surface deformation fields. Figure 4.8 shows the parameter definition and local coordinate system of Okada's point and finite rectangular tensile faults. The point fault (left) is centered at  $(x_0, y_0, -d)$ , while the center of finite rectangular fault (right) is defined by the middle point of its lower edge. For both models, the faults strike along the  $x$ -axis and have a dipping angle  $\delta$  from horizontal.  $M_0$  is the tensile moment of the point fault. For the rectangular fault,  $W$  is the down-dip width,  $L$  denotes its half-length, and  $U$  stands for the uniform opening of the fault that is normally many orders of magnitude smaller than the size of the fault.

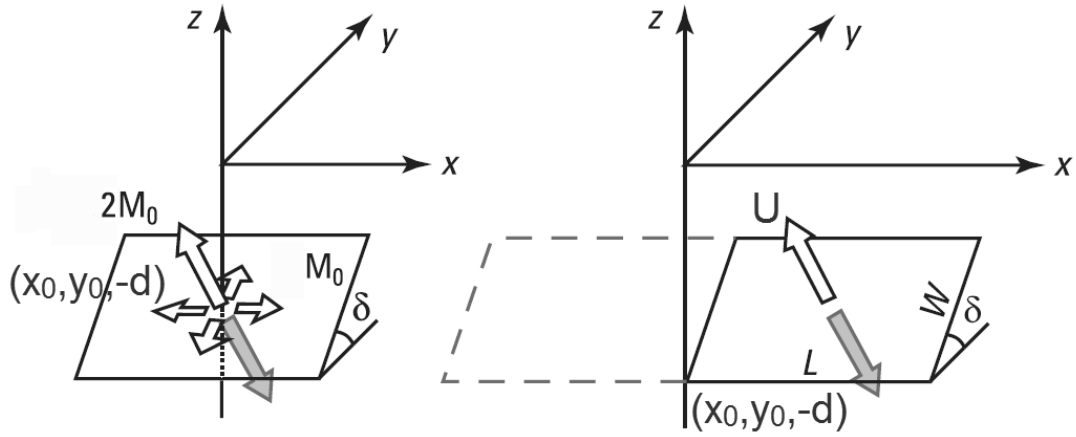


Figure 4.8 Parameter definition and local coordinate system of dipping point and finite rectangular tensile faults. (Okada 1992)

#### Point tensile crack:

The surface displacements produced by a point tensile crack are given by:

$$\begin{aligned}
 U_x &= \frac{M_0}{2\pi G} \left( \frac{3(x-x_0)q^2}{R^5} - (1-2\nu)I_3^0 \sin^2 \delta \right) \\
 U_y &= \frac{M_0}{2\pi G} \left( \frac{3(y-y_0)q^2}{R^5} - (1-2\nu)I_1^0 \sin^2 \delta \right) \\
 U_z &= \frac{M_0}{2\pi G} \left( \frac{3dq^2}{R^5} - (1-2\nu)I_5^0 \sin^2 \delta \right)
 \end{aligned} \tag{40}$$

where

$$\begin{aligned}
 I_1^0 &= (y-y_0) \left( \frac{1}{R(R+d)^2} - (x-x_0)^2 \frac{3R+d}{R^3(R+d)^3} \right) \\
 I_2^0 &= (x-x_0) \left( \frac{1}{R(R+d)^2} - (y-y_0)^2 \frac{3R+d}{R^3(R+d)^3} \right) \\
 I_3^0 &= \frac{x-x_0}{R^3} - I_2^0 \\
 I_5^0 &= \frac{1}{R(R+d)} - (x-x_0)^2 \frac{2R+d}{R^3(R+d)^2}
 \end{aligned} \tag{41}$$

$$\begin{aligned}
 q &= (y-y_0) \sin \delta - d \cos \delta \\
 R &= \sqrt{(x-x_0)^2 + (y-y_0)^2 + d^2}
 \end{aligned} \tag{42}$$

where  $R$  is the distance from fault center to the point at the free surface,  $M_0$  the tensile moment,  $\delta$  the dipping angle. Other symbols remain the same as in Equation (37).

Figure 4.9 shows the horizontal (left) and vertical (right) surface displacement fields

along (Figure 4.9a) and across (Figure 4.9b) an Okada point tensile crack with different dipping angles ( $\delta = 0^\circ, 30^\circ, 45^\circ, 60^\circ$  and  $90^\circ$ ). The origin in the plots is moved to  $(x_0, y_0, 0)$ , the distance is in the unit of the fault depth which is the depth of the fault center, and all the displacements are normalized by the maximum vertical displacement produced by a horizontal point tensile crack ( $\delta = 0^\circ$ ). To better understand the whole pattern of surface deformation, a 2D plot of surface displacement fields generated by an Okada point tensile crack with dipping angle  $\delta = 90^\circ$  is illustrated in Figure 4.10. Horizontal displacements are denoted by arrows while vertical displacements are represented by different colors.

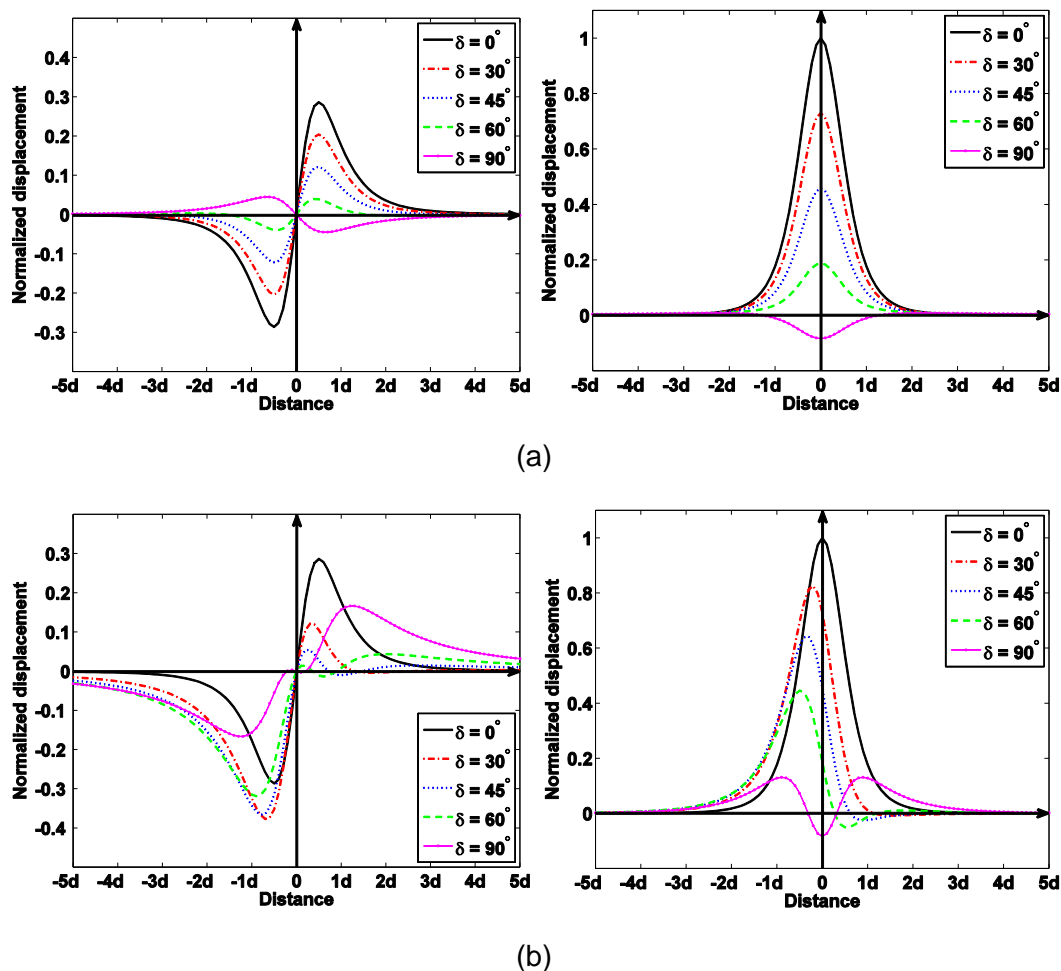


Figure 4.9 Normalized surface displacement fields generated by a point tensile crack. (a). Surface displacements along the crack; (b). Surface displacements across the crack.

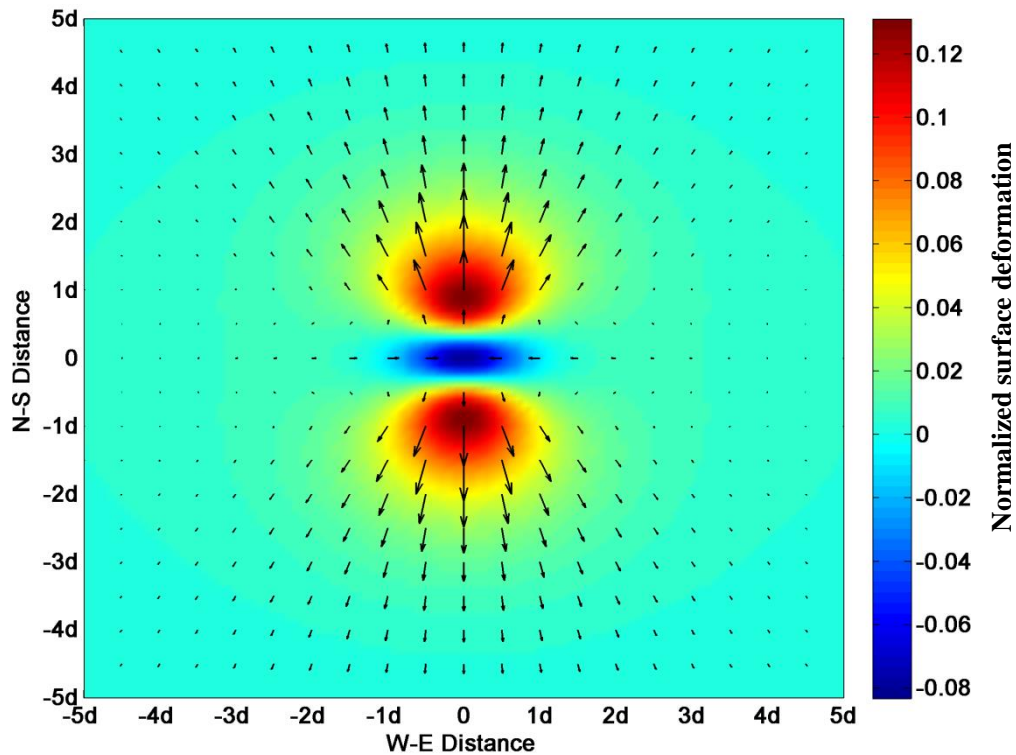


Figure 4.102D normalized surface deformation of Okada model induced by a point tensile crack with dipping angle  $\delta = 90^\circ$ .

From Figure 4.9 we can see, both the horizontal and vertical surface displacements along the point tensile crack decrease as the dipping angle increases, and when the dipping angle is large ( $\delta = 75^\circ$ ), the surface displacements will reverse.

For the surface displacements across the point tensile crack, they are axisymmetric only when the crack is horizontally or vertically embedded. In other cases, the displacement fields are skewed to the down-dip direction. The maximum vertical displacement decreases with increasing dipping angle, and a depression appears in the up-dip direction.

The Okada point tensile crack has six parameters in total, which are  $(x_0, y_0, -d)$  for the location of the fault center,  $M_0$  for the tensile moment,  $\delta$  for the dipping angle, and finally  $\beta$  for the strike angle.

#### **Finite rectangular tensile crack:**

The surface displacements produced by a finite rectangular tensile crack are given by:

$$\begin{aligned}
 U_x &= \frac{U}{2\pi} \left( \frac{q^2}{R(R+\eta)} - (1-2\nu)I_3 \sin^2 \delta \right) \Big\| \\
 U_y &= \frac{U}{2\pi} \left( \frac{-\tilde{d}q}{R(R+\xi)} - \sin \delta \left( \frac{\xi q}{R(R+\eta)} - \tan^{-1} \frac{\xi \eta}{qR} \right) + (1-2\nu)I_1 \sin^2 \delta \right) \Big\| \\
 U_z &= \frac{U}{2\pi} \left( \frac{\tilde{y}q}{R(R+\xi)} + \cos \delta \left( \frac{\xi q}{R(R+\eta)} - \tan^{-1} \frac{\xi \eta}{qR} \right) - (1-2\nu)I_5 \sin^2 \delta \right) \Big\|
 \end{aligned} \quad (43)$$

where

$$\begin{aligned}
 I_1 &= \frac{1}{\cos \delta} \frac{\xi}{R+\tilde{d}} + \frac{\sin \delta}{\cos \delta} I_5 \\
 I_3 &= \frac{1}{\cos \delta} \frac{\tilde{y}}{R+\tilde{d}} - \ln(R+\eta) + \frac{\sin \delta}{\cos^2 \delta} \left( \ln(R+\tilde{d}) - \sin \delta \ln(R+\eta) \right) \\
 I_5 &= \frac{2}{\cos \delta} \tan^{-1} \frac{\eta(X+q \cos \delta) + X(R+X) \sin \delta}{\xi(R+X) \cos \delta}
 \end{aligned} \quad (44)$$

and if  $\cos \delta = 0$ ,

$$\begin{aligned}
 I_1 &= \frac{\xi q}{2(R+\tilde{d})^2} \\
 I_3 &= \frac{1}{2} \left( \frac{\eta}{R+\tilde{d}} + \frac{\tilde{y}q}{(R+\tilde{d})^2} - \ln(R+\eta) \right) \\
 I_5 &= -\frac{\xi}{R+\tilde{d}} \sin \delta
 \end{aligned} \quad (45)$$

$$\begin{aligned}
 p &= (y-y_0) \cos \delta + d \sin \delta \\
 q &= (y-y_0) \sin \delta - d \cos \delta \\
 \tilde{y} &= \eta \cos \delta + q \sin \delta \\
 \tilde{d} &= \eta \sin \delta - q \cos \delta \\
 R &= \sqrt{\xi^2 + \eta^2 + d^2} \\
 &= \sqrt{\xi^2 + \tilde{y}^2 + \tilde{d}^2} \\
 X &= \sqrt{\xi^2 + q^2}
 \end{aligned} \quad (46)$$

where  $\|$  in Equation (43) denotes the Chinnery's notation to represent the substitution:

$$f(\xi, \eta) \Big\| = f(x' + L, p) - f(x' + L, p - W) - f(x' - L, p) + f(x' - L, p - W) \quad (47)$$

and in which  $x' = x - x_0$ .

Figure 4.11 shows the horizontal (left) and vertical (right) surface displacement fields along (Figure 4.11a) and across (Figure 4.11b) an Okada finite rectangular tensile crack with different dipping angles ( $\delta = 0^\circ, 30^\circ, 45^\circ, 60^\circ$  and  $90^\circ$ ). Again, in the plots, all the origins are moved to  $(x_0, y_0, 0)$  for convenience. The distances are in the unit of fault depth which is defined by the depth of the middle point of the fault's lower edge. All the displacements are normalized by the maximum vertical displacement produced by a horizontal finite rectangular tensile crack ( $\delta = 0^\circ$ ).

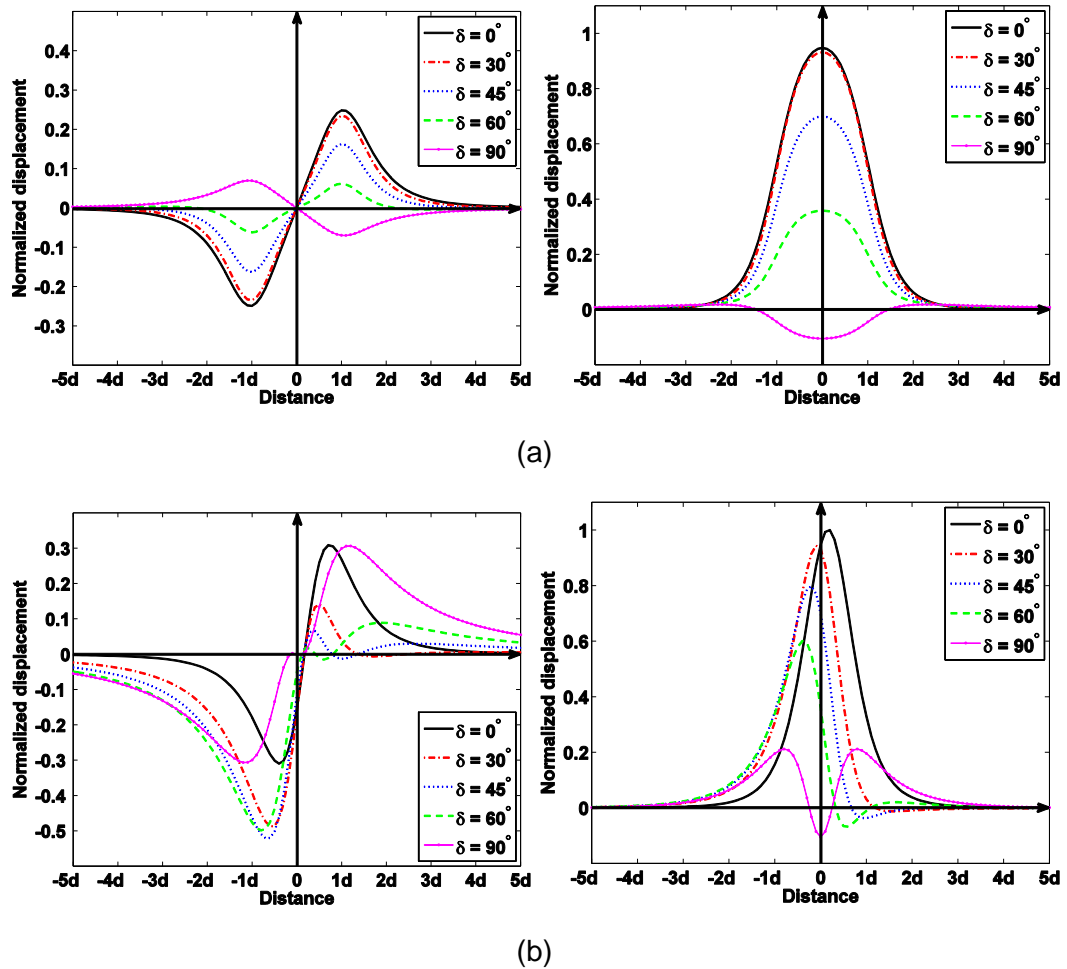


Figure 4.11 Normalized surface displacement fields generated by a finite rectangular tensile crack. (a). Surface displacements along the crack; (b). Surface displacements across the crack.

Compared with Figure 4.9, we can see that the surface displacements along the finite rectangular tensile crack decrease with increasing dipping angle, which is similar to the point tensile crack. But the shape of vertical displacements is much broader than the one of point crack since the length of the crack is taken into account.

The surface displacements across the finite rectangular tensile crack have similar features as the point crack discussed above. However, due to the definition of the center of the finite rectangular crack, both the horizontal and vertical displacements have an offset of  $\frac{W}{2} \cos \delta$  to the origin, and of course when the rectangular crack is vertically embedded i.e.  $\delta = 90^\circ$ , the offset will vanish.

A 2D plot of surface deformation fields produced by a vertical Okada finite rectangular tensile crack ( $\delta = 90^\circ$ ) is provided in Figure 4.12 for comparison. The arrows represent the horizontal deformation and the colors illustrate the vertical one.

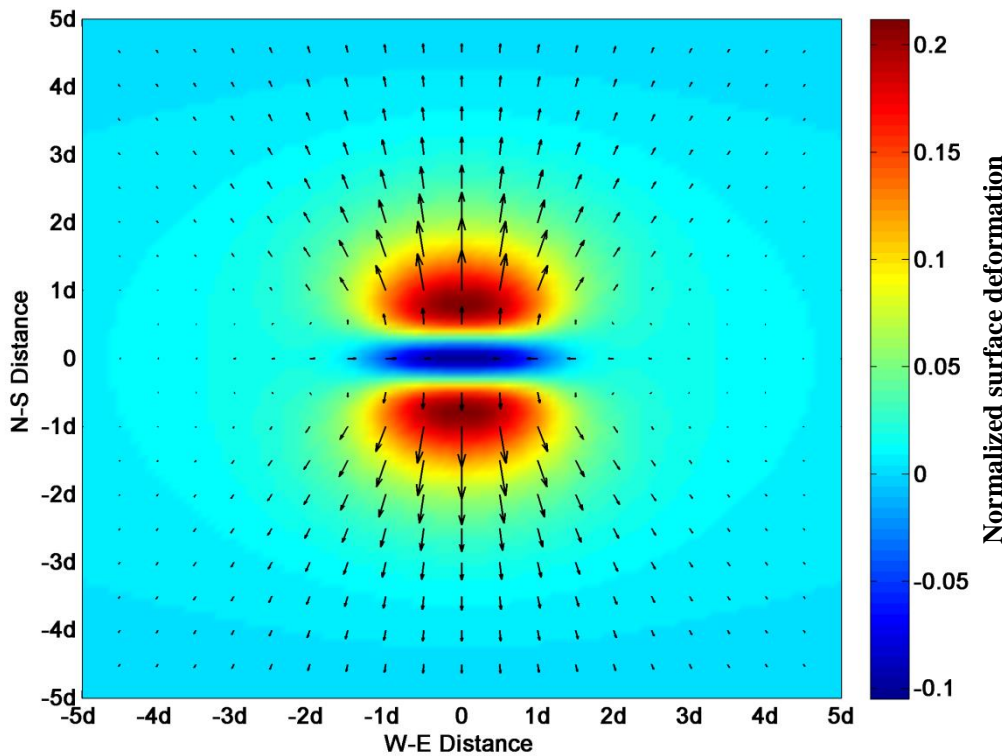


Figure 4.122D normalized surface deformation induced by a finite rectangular tensile crack with dipping angle  $\delta = 90^\circ$ .

The Okada finite rectangular tensile crack has eight independent parameters in total, which are  $(x_0, y_0, -d)$  for the location of the fault center,  $L$  and  $W$  for the size of the crack,  $U$  for the opening of the crack, the dipping angle  $\delta$ , and the strike angle  $\beta$  for the orientation of the crack.

#### 4.1.5 Tradeoff between parameters

As mentioned in previous sections, one big issue suffered nearly by all the analytical volcano source models is that there are many tradeoffs between the parameters. Some tradeoffs can be easily recognized from the model's formulation, for instance, from the Equation (37) we can clearly see the tradeoff between the radius  $a$  and pressure change  $\Delta P$  of Mogi source, in that case, if  $a^3 \Delta P$  is kept as a constant, then the deformation will not change with different radius  $a$  and pressure change  $\Delta P$ . That is why we decide to introduce the new parameter "source strength  $S$ " into the model at the first place. Even so, there are still many other tradeoffs that are not so obvious for people to see, and we will use some specific examples to provide a rough idea about the tradeoffs and discuss them in more detail in this section. It needs to be mentioned that these tradeoffs are one of the main reasons why the final inverted solution of parameters may not be unique, and they also affect the stability of the inversion.



The process of finding out how much influence the tradeoffs between parameters will have on the inversed solution is called sensitivity analysis of solution to the change in model parameters. Here in this section, the tradeoffs of each analytical source model are illustrated and discussed by means of applying a grid search on two parameters while fixing the others. For each combination of the two parameters, we evaluate the surface deformation at certain given measure points and calculate the corresponding  $\chi^2$  values by Equation (48). (Andrae et al. 2010)

$$\chi^2 = \sum_i \frac{(U_i - U_i^{ref})^2}{\sigma^2} \quad (48)$$

### Mogi source model

The Mogi source model has four independent parameters, which are  $x_0$ ,  $y_0$ ,  $d$  and source strength  $S$ . Some parameters like  $x_0$  and  $y_0$  are well constrained i.e. there are no tradeoff between them, which can be seen from the result of grid search (see Figure 4.13). But for other parameters such as  $d$  and  $S$ , the tradeoff is quite clear as shown in Figure 4.14. The star in the figures indicates the minimal  $\chi^2$ , i.e. the  $\chi^2$  of the reference model.

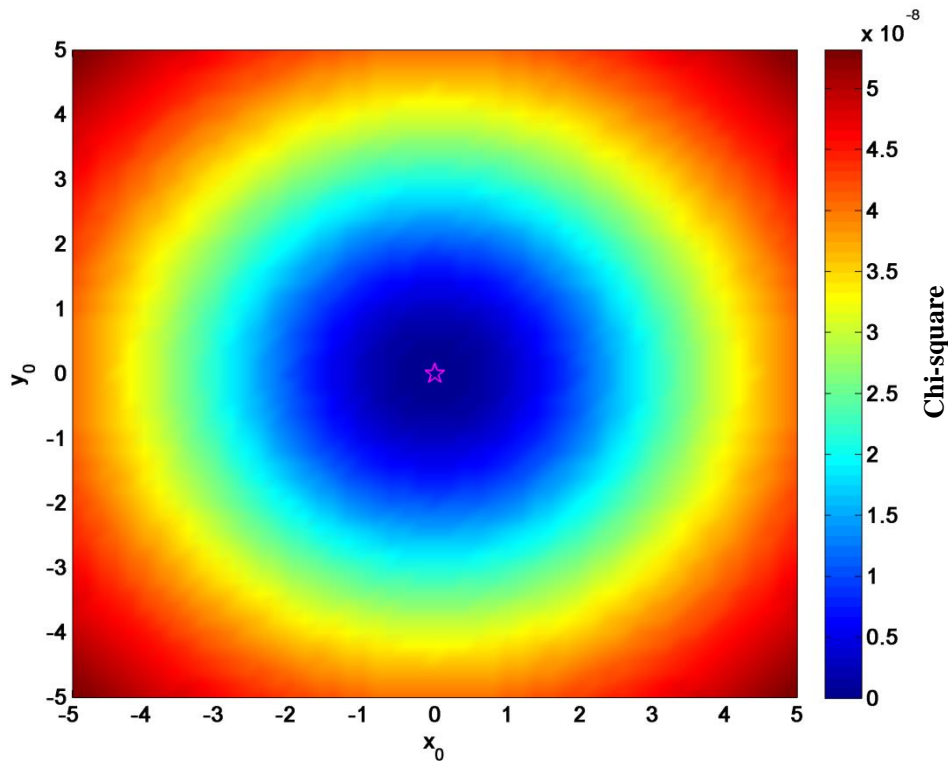


Figure 4.13  $\chi^2$  plot for the grid search of parameter  $x_0$  and  $y_0$ .

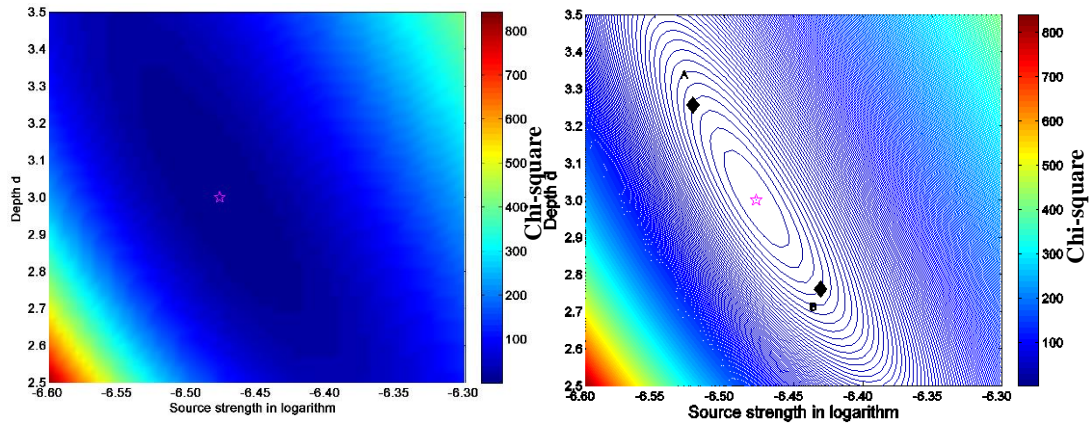


Figure 4.14  $\chi^2$  plot and contour plot for the grid search of parameter  $d$  and  $S$  (with a contour interval of 2.1).

From Figure 4.14 we can see, along each contour line, all the combinations of the source depth  $d$  and source strength  $S$  are equally good in the  $\chi^2$  sense, which also means that there is no way to distinguish the ground surface deformations produced by them.

Normally speaking a reduced  $\chi^2$  less than 1 can be considered as a good solution, here in our case, theoretically we can get  $\chi^2 = 0$  (indicated by the pink star), although it generally never happens in reality. To be more realistic, we assume that any solution inside the first contour line (2.1) in Figure 4.14 (right) is a good solution. This value of  $\chi^2$  is related to typical uncertainties of measured data. And if we arbitrarily choose two points (indicated by the black diamonds) on the same contour line inside this region, which are A ( $\Delta P = -3.33 \times 10^6$  Pa,  $d = 3.26$  km) and B ( $\Delta P = -2.70 \times 10^6$  Pa,  $d = 2.76$  km) and plot the corresponding two surface deformation fields (as shown in Figure 4.15), we can clearly see the two deformation fields are almost identical. That is to say, in our inversion we cannot have any sensitivity to distinguish those two parameters.

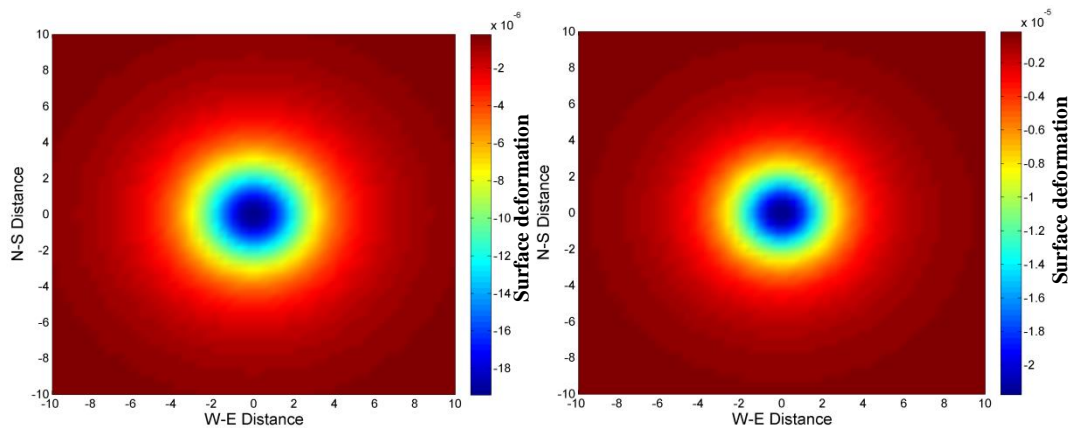


Figure 4.15 Surface deformations produced by different parameter settings A (left)

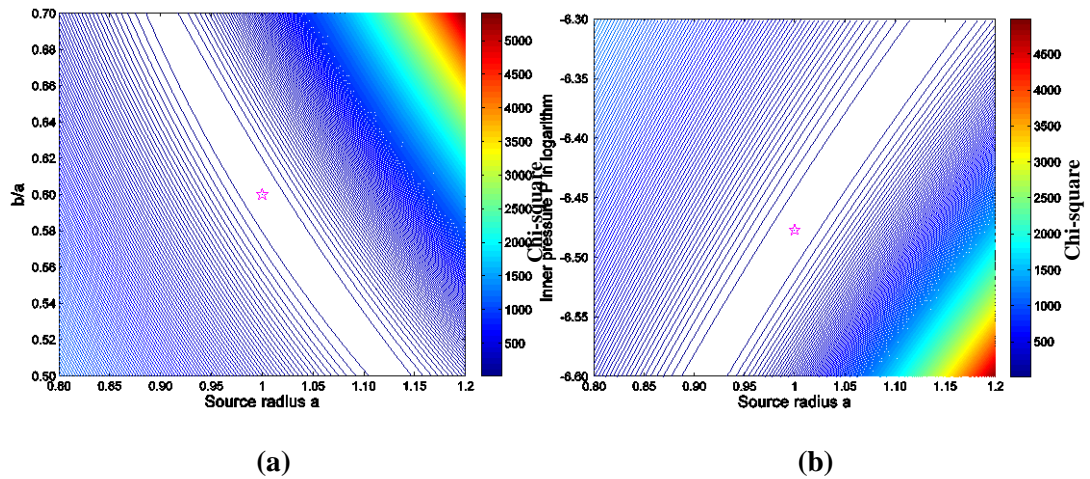
and B (right).

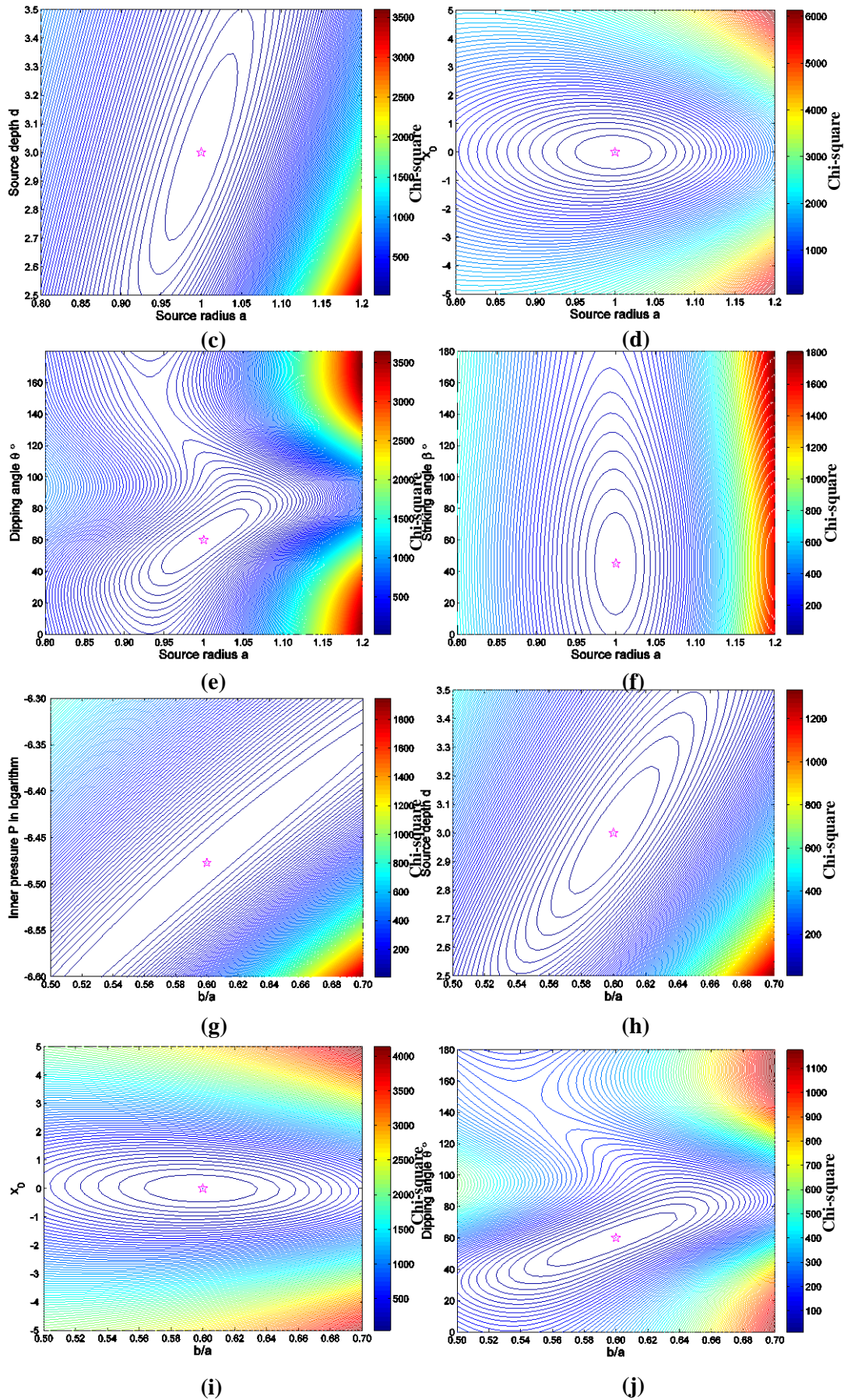
### Yang's model

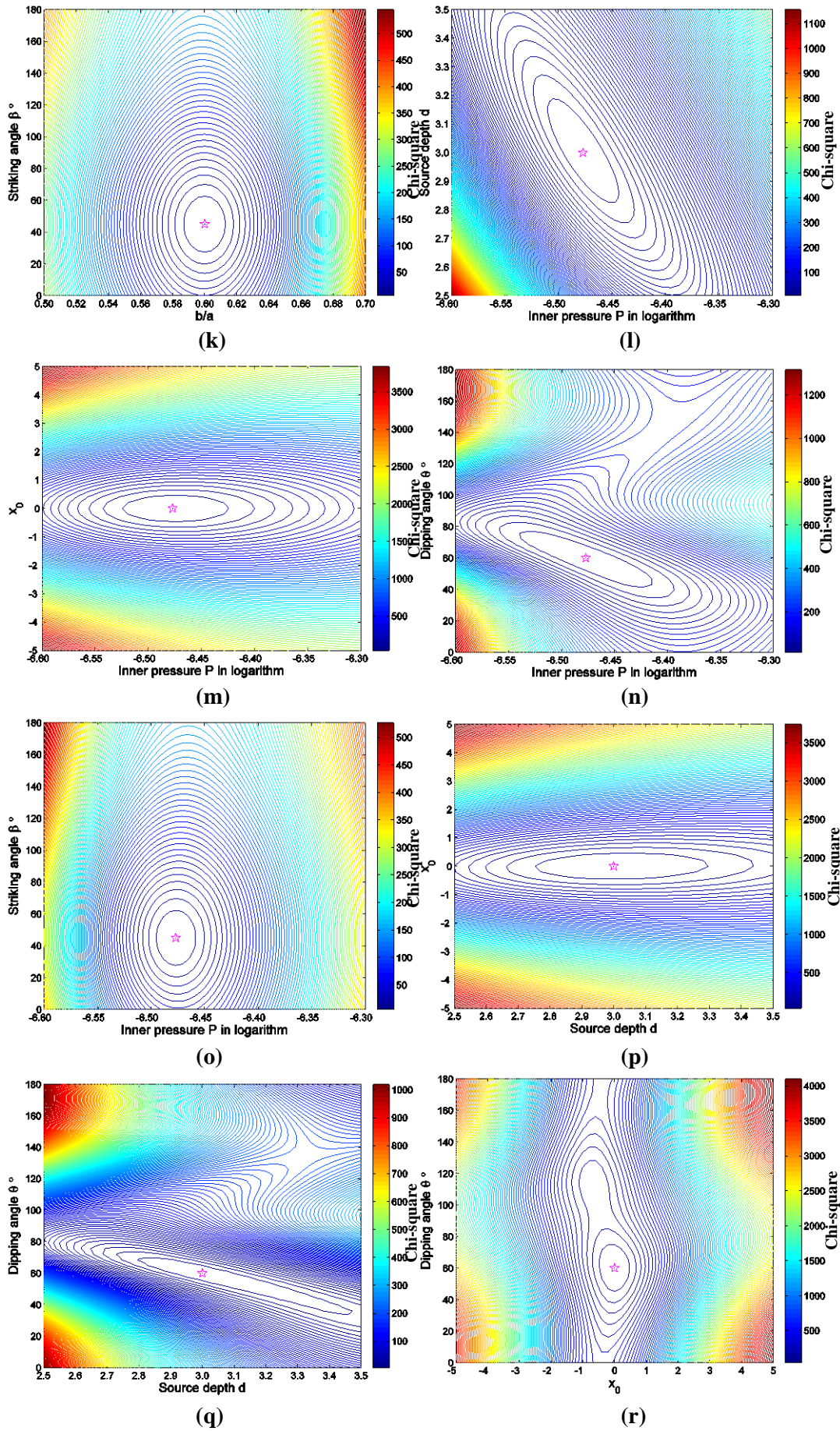
The Yang's model has eight independent parameters, so the situations of tradeoffs between parameters are much more complicated than the spherical case. The given combination of parameters used as model reference in the grid search is a prolate spheroidal source with semi-axis  $a = 1$  km,  $b/a = 0.6$ , centered at point  $(0, 0, -3)$ , the inner pressure  $P$  is  $-3 \times 10^6$  Pa, and its dipping angle  $\theta$  and striking angle  $\beta$  are  $60^\circ$  and  $45^\circ$  respectively. The range of each parameter is listed in Table 4-1. For each grid search, we fix six parameters to their reference values and only allow the other two parameters to vary within their range. Some of the results of grid searches are plotted in Figure 4.16. Again, the star in the figure indicates the minimal  $\chi^2$ , i.e. the  $\chi^2$  of the reference model.

Table 4-1 Range of all the parameters of Yang's model used in the grid search.

Parameter	$a$ (km)	$b/a$	$P$ (Pa)	$x_0$ (km)	$y_0$ (km)	$d$ (km)	$\theta$ ( $^\circ$ )	$\beta$ ( $^\circ$ )
Lower bound	0.8	0.5	$2 \times 10^6$	-5	-5	2.5	0	0
Upper bound	1.2	0.7	$4 \times 10^6$	5	5	3.5	180	180







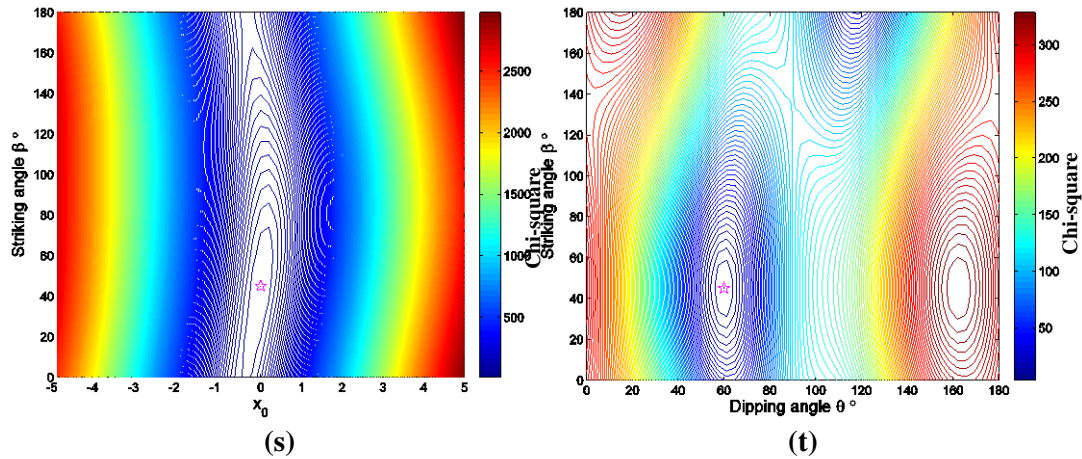


Figure 4.16(a)-(t) Contour plot of  $\chi^2$  for the grid searches between parameters of the Yang's model. The pink star indicates the minimum of  $\chi^2$ , i.e. the  $\chi^2$  of the reference model. The contour interval is set to 1/400 of the maximum of each panel in order to show the pattern more clearly.

From Figure 4.16 we can see that there are multiple tradeoffs among a variety of parameters. The tradeoffs are so complex that we cannot easily know how many degrees of freedom we have. For some parameters such as the horizontal location of the source center  $x_0$  and  $y_0$ , we can constrain them very well. For some parameters like the source radius  $a$  and  $b/a$  or  $a$  and  $\Delta P$  (see the first two panels of Figure 4.16, panels (a) and (b)), there are pure linear tradeoffs between them. All the parameter combinations inside the long narrow valley region will provide the "same" or "very similar" surface deformation fields and so we have no sensitivity to distinguish these parameters in the inversion. In some cases where one of the two parameters is well constrained, but the other one is not, e.g. between  $d$  and  $x_0$  (see panel (p) of Figure 4.16). And for the other parameters there are more complex relations between them, which can be clearly seen from relation between the depth  $d$  and dipping angle  $\theta$  (see panel (q) of Figure 4.16). In fact, what we see from Figure 4.16 are basically the marginal distributions of  $\chi^2$ . Since the parameter space is an eight dimensional space, we should note that there could be more complex tradeoffs occurred in hyper-space (as indicated by the plot between  $a$  and  $\theta$ , see panel (e)), which cannot be easily seen by just applying the 2D grid search. It is also worth to mention that when calculating the  $\chi_r^2$ , we usually assume that all these model parameters are free parameters, but we must keep in mind that in reality the degree of freedom is smaller than the number of model parameters because of the tradeoffs discussed above.

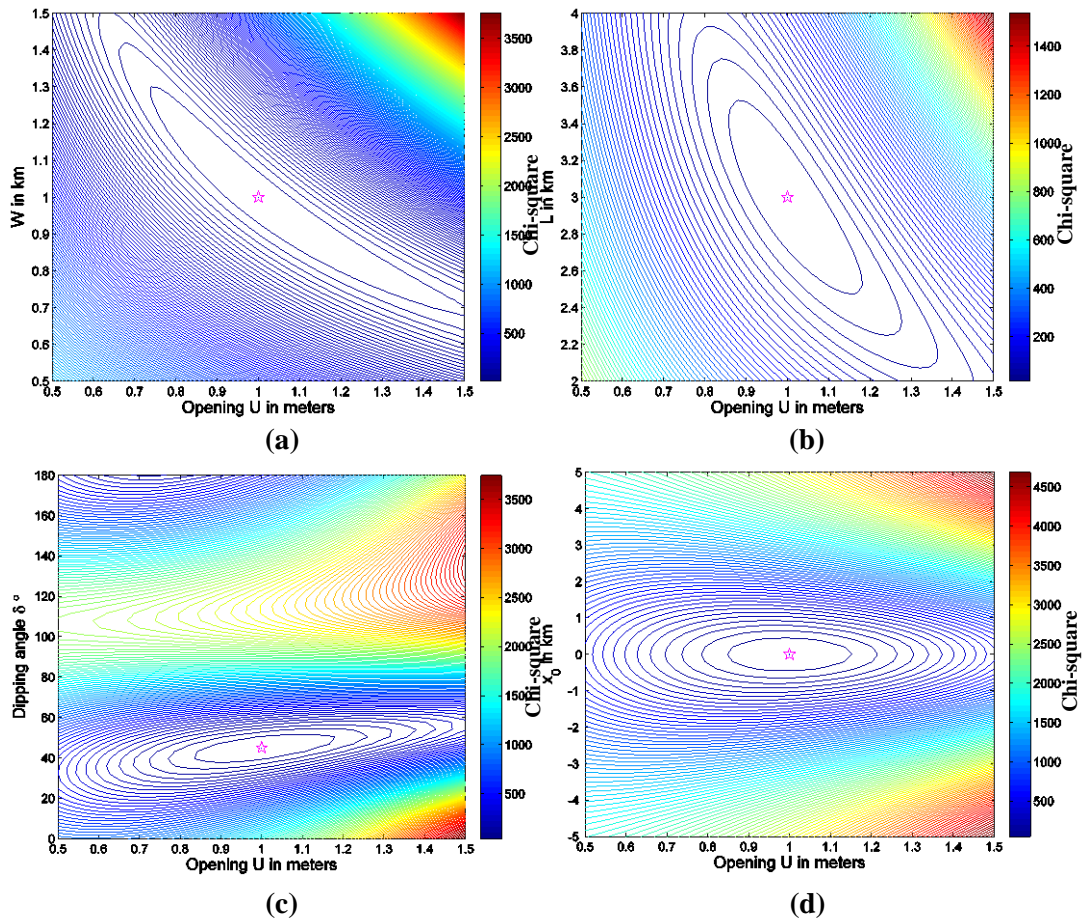
### Okada model

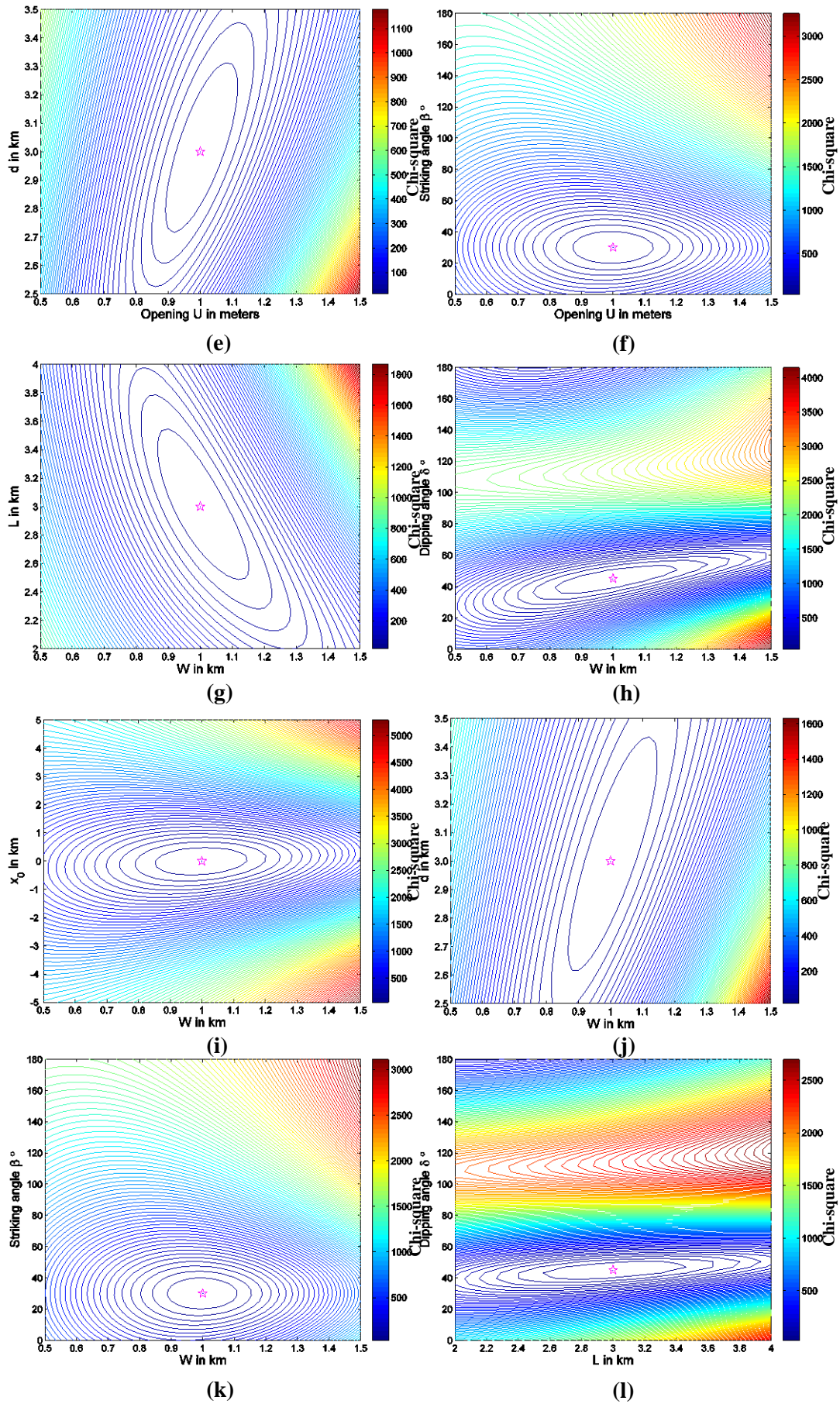
The Okada model, i.e. finite rectangular fault model, has eight independent parameters too. We set a combination of parameters as model reference and applied the grid search similar to what we did for the Yang's model. The given model reference is a rectangular fault with  $L = 3$  km and  $W = 1$  km bottom-centered at  $(0, 0, -3)$ , its opening  $U$  is 1 m, and the dipping angle  $\delta$  and striking angle  $\beta$  are  $45^\circ$  and  $30^\circ$ , respectively. The ranges of all the parameters are listed in Table 4-2. Part of the grid search results are plotted in Figure

4.17.

Table 4-2 Range of all the parameters of Okada model used in the grid search.

Parameter	$U$ (m)	$W$ (km)	$L$ (km)	$x_0$ (km)	$y_0$ (km)	$d$ (km)	$\delta$ ( $^\circ$ )	$\beta$ ( $^\circ$ )
Lower bound	0.5	0.5	2	-5	-5	2.5	0	0
Upper bound	1.5	1.5	4	5	5	3.5	180	180







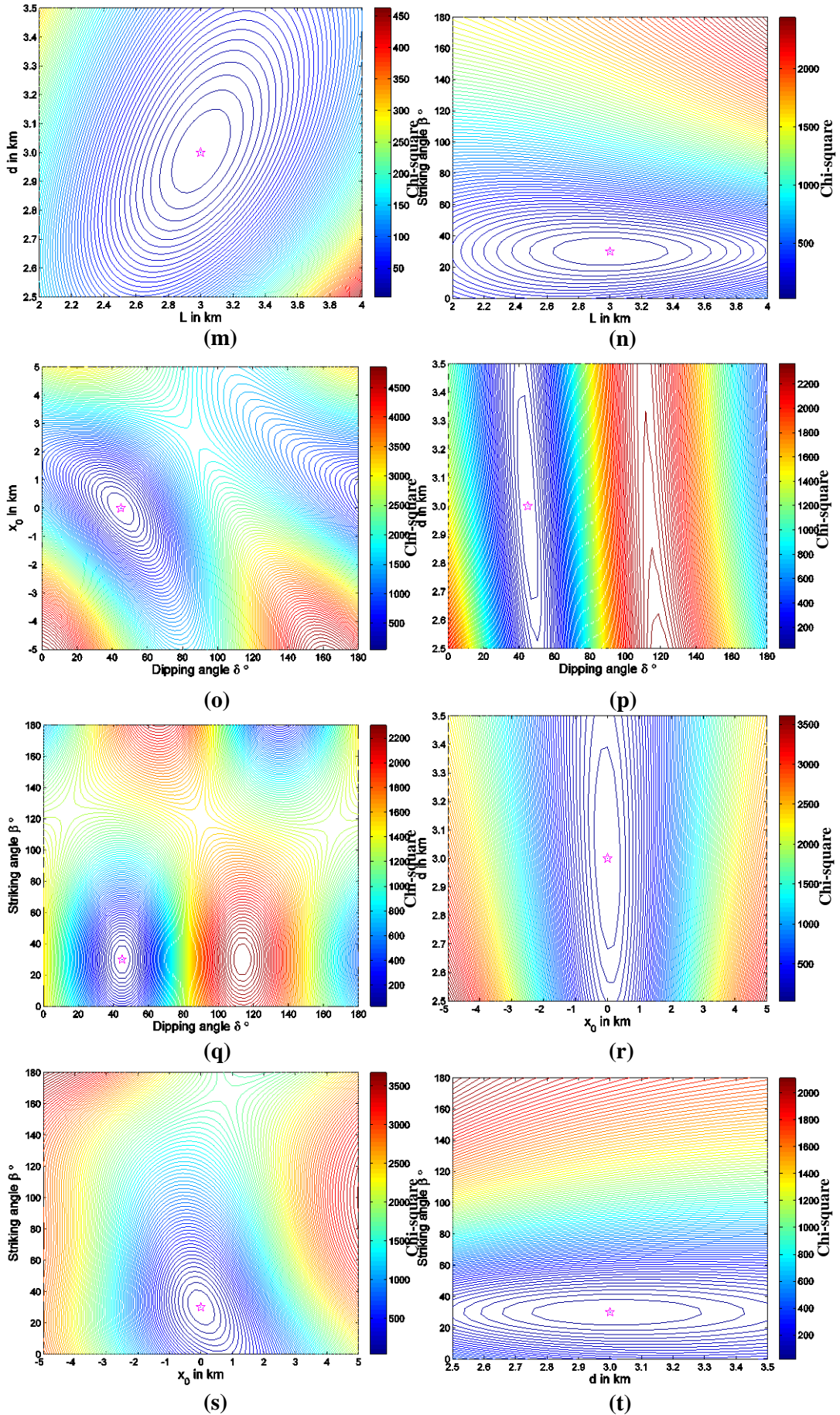


Figure 4.17(a)-(t) Contour plot of  $\chi^2$  for grid searches between parameters of the Okada model. The pink star indicates the minimum of  $\chi^2$ , i.e. the  $\chi^2$  of the reference model. The contour interval is set to 1/400 of the maximum of each panel in order to show the pattern more clearly.

Similar with the Yang's model, it can be seen from Figure 4.17 that the tradeoffs between parameters of Okada model have many different patterns as well. Due to the complex tradeoffs, it is also difficult to say how many degrees of freedom we have. For some parameters like  $x_0$ ,  $y_0$  and striking angle  $\beta$ , they are well-constrained. For the dipping angle  $\delta$ , from the figures we can see that it is generally well-constrained but the contour plot of  $\chi^2$  contains some saddle points and local minima. For the source depth  $d$ , it is not so well-constrained, i.e. the sensitivity of  $d$  is relatively low. For the other parameters such as  $U$  and  $W$  or  $U$  and  $L$ , we can clearly see the tradeoffs (see the first two panels of Figure 4.17, panels (a) and (b)) between them, which indicate that in the inversion we cannot have good sensitivity to determine the related parameters.

## Chapter 5

### Metamodels Substituting Computer Simulations

---

Although the analytical models mentioned in previous chapter have made great contributions to understanding and investigating the mechanism of geophysical phenomena, they by nature have some restricts - the simplifications, which are needed for obtaining analytical solutions. Due to the rapid development happened in the fields of computer science and technology, in today's world, more and more scientific and engineering methods are highly based on the computer-based codes and numerical computations, among which is the widely-used finite element method, for instance. These computer codes or numerical models normally only provide discrete information (such as nodal or elemental solutions used in FEM) about the underlying relationship connecting the input parameters with the output results or observations, that is partly because of the binary-based working principle of modern computers. With the help of numerical analysis, we are able to take more factors such as real topography (Williams and Wadge 1998, Williams and Wadge 2000, Trasatti et al. 2003, Lungarini et al. 2005, Masterlark and Feigl 2012), heterogeneity (Manconi et al. 2007, Manconi et al. 2010), material viscosity (Newman et al. 2006, Scandura et al. 2008), etc. into account in order to establish more complex and more realistic models which can be applied to describe and solve real problems that are too complex for the analytical models. (Bonaccorso et al. 2005, Currenti et al. 2008a, Del Negro et al. 2009, Manconi et al. 2009) However, the more complex model we have, the more time it will take to run. Although today's computers have real powerful calculation ability, running complex numerical models is still quite a time consuming task. As mentioned in Chapter 2, the whole process of inversion is actually an optimization problem and the models are usually required to be run many times to find the optimum. Obviously, the price of running complex numerical models hundreds or even thousands of times is significant, so the time consuming issue becomes even more critical for solving inverse problems.

With the aim to reduce the computation cost for solving inverse problems, an approach applying statistical global approximation techniques is presented. The basic idea of the approach is to construct approximations of the original complex computer codes and use them to replace the original codes in the optimization process (Simpson et al. 2001, Park and Jeon 2002). It is clear that the approximations should be more efficient to evaluate than the original models, and at the same time they should gain an insight into the core relationship between input parameters  $\mathbf{X}$  and an output  $Y$ , that is to say, the approximations should provide the same or similar results as the original codes. If the essence of relationship between  $\mathbf{X}$  and  $Y$  is

$$Y = f(\mathbf{X}) \quad (49)$$

then its approximation can be written as

$$\hat{Y} = g(\mathbf{X}) \quad (50)$$

and so

$$Y = \hat{Y} + \varepsilon \quad (51)$$

where  $\varepsilon$  represents the errors, including both the approximation and random ones. The approximation  $\hat{Y}$  here is called a metamodel. By definition, a metamodel is an approximation of a simulation model, which indicates the functional relationship between the input variables  $\mathbf{X}$  and output variable  $Y$  of the simulation model. The metamodel and the simulation model have exactly the same value only on several points (known as evaluation points or sampling points); the values of other points are gained by other mathematic methods such as interpolating. In different literatures, the term "metamodel" is also known as surrogates, response surfaces, auxiliary models, and so on, in this work, metamodel is preferred. (Kleijnen 2009)

To generate a metamodel normally needs three steps.

Firstly, we need to select an appropriate set of sampling points ( $\mathbf{X}_1, \mathbf{X}_2, \mathbf{X}_3, \dots, \mathbf{X}_k$ ) to obtain information about the whole simulation model. The way to select the efficient set of sampling points is known as design of experiments method (DoE method), which will be discussed afterwards.

Secondly, we need to choose a proper formulation of the metamodel (also known as metamodeling approach) according to different purpose. The common choices include linear or quadratic polynomials, radial basis functions, stochastic process, network of neurons, and so on.

Finally, we need to find a way of fitting the metamodel to the data evaluated at the sampling points. Least squares regression is one of the widely used methods to fit the model to the data. Besides, best linear unbiased predictor and log-likelihood have been proven to have better performance in stochastic cases. (Kleijnen 2009)

Compared with the original model, a good metamodel has several advantages as follows. It can show a better expression of the relationship between  $\mathbf{X}$  and  $Y$ ; it can provide reduction in computational costs (or acceleration of the analysis); and moreover, with it one can do simple exploration of the entire design space, which is extremely important especially for optimization process. All these benefits make the metamodel very suitable of being used in optimization. It can be used to replace the original complex models and make the whole inversion much more efficient. (Jurecka 2007)

## **5.1 Design of Experiments (DoE)**

Since the expense and time spent on simulation of many input variables with complex rela-

tionships among each other are non-trivial, so the number of simulation runs is really limited. Usually, only several hundred to thousand runs are feasible. Depending on these runs, a complete analysis of the simulation model is required. That is to say, the number of simulation runs should be minimized, and at the same time the information about the model obtained from these simulation runs should be as much as possible.

Consequently, the choice of location of the sampling points (or evaluation points) is very important in getting a good approximation of the response, especially when evaluations are expensive. The methods used for selecting the sampling points are together termed as design of experiments (DoE). (Jurecka 2007)

The DoE methods were originally developed as a systematic approach for laboratory or field experiments to obtain a maximum of information about a data trend with the least amount of effort. A DoE method defines a set of experiments (FE simulations) to be performed, which is expressed in terms of  $n$  input variables (input parameters) set to specific values. Each of these input parameter sets is called a sampling point in design of experiments. Each experiment provides a single value which is also called the response value at the corresponding sampling point. In other words, each experiment is a selected combination of  $n$  input parameters  $\mathbf{X} = (X_1, X_2, \dots, X_n)$ . The better the DoE method is, the more efficient the selection of  $\mathbf{X}$  would be.

There are many different methods to do the design of experiments (Unal et al. 1998, Simpson et al. 2001, Jurecka 2007). Here we provide a short review of some representative DoE methods.

### **Factorial designs:**

Factorial design is the most fundamental kind of experimental design. There are two common types of factorial designs: *full factorial design* and *fractional factorial design*. The number of sampling points given by a full factorial design is equal to the product of the number of levels (e.g. the minimum and maximum of a design parameter can be called as 2 levels, the minimum, median and maximum of a design parameter can be called as 3 levels) for each input parameter (e.g.  $2^n$  for  $n$  input parameters at 2 levels). The mostly used full factorial designs are  $2^n$  and  $3^n$  designs. Moreover, a  $2^n$  design is actually a set containing all the vertices of a  $n$ -D design space, which is of great importance for constrained optimization problems, since the optima sometimes locate at the vertices of the feasible domain.

As the number of sampling points of a full factorial design will increase exponentially with large amount of input parameters, it is difficult to handle. In this case, a fractional factorial design is used instead. A fractional factorial design is one section of the full factorial design, the most common design form is  $2^{(n-p)}$ , in which the section is  $1/2^p$ . It is often used for identifying or screening for important input parameters. In Figure 5.1 below, examples of  $2^3$  full factorial design (a) and  $2^{(3-1)}$  fractional factorial design (b) are given.

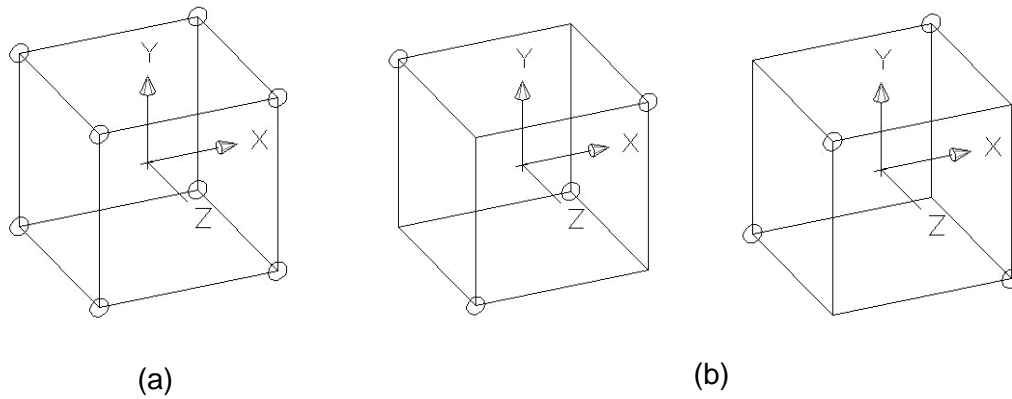


Figure 5.1 Examples of factorial designs.

**Central composite design (CCD) and Box-Behnken design:**

Central composite and Box-Behnken designs are the most common second order designs used to estimate quadratic effects with fewer sampling points. A central composite design (CCD) is based on a two level full or fractional factorial design ( $2^n$  or  $2^{(n-p)}$ ), added with  $n_0$  center points and two so called ‘star’ points located at  $\pm\alpha$  for each input parameter. For  $K$  parameters, the number of total sampling points is  $2^K + 2K + n_0$ . The Figure 5.2 shows the case that a CCD has three input parameters.

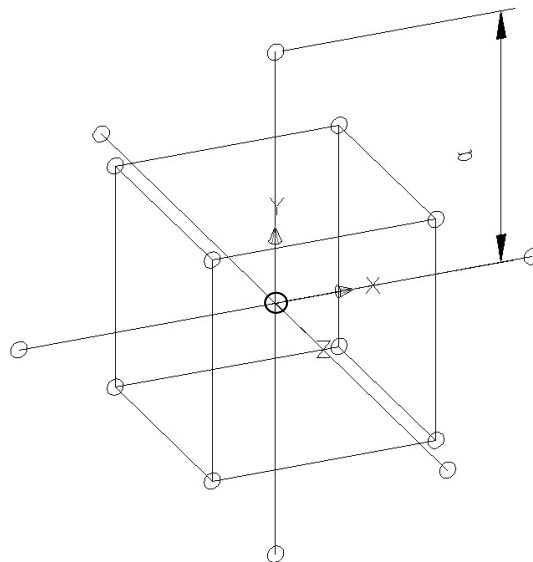


Figure 5.2 Example of Central Composite Design.

For the case of three input parameters shown above, if  $\alpha = 1$ , the star points will lo-

cate at the centers of the faces of the cubic. This case is also called face-centered central composite design (CCFD).

Box-Behnken designs are generated by combining the  $2^n$  factorial design together with some incomplete block designs, in order to make the number of factor levels used in experimental design as small as possible. (Box and Behnken 1960)

**Orthogonal arrays (OA):**

Orthogonal arrays method proposed by Taguchi (Taguchi et al. 1993) is created for the purpose of decreasing the number of sampling points used in experimental designs. A design is called orthogonal if, for every couple of input parameters  $X_i$  and  $X_j$ , the sum of cross product of all the  $P$  sampling points satisfies

$$\sum_{k=1}^P X_{ik}X_{jk} = 0 \tag{52}$$

Orthogonal arrays are normally fractional factorial designs at 2 or 3 levels (i.e.  $2^{(n-p)}$  or  $3^{(n-p)}$ ). For example, 2 level  $L_{12}$  arrays can evaluate 11 input parameters using only 12 sampling points. And 2 level  $L_{16}$  arrays use 16 design points to estimate 15 effects. (Simpson et al. 2001)

Besides, there are also other methodologies. Among these methods, one satisfactory method of selecting the values of input variables is the Latin hypercube designs (or Latin Hypercube sampling method), first proposed by McKay et al. (1979) and Iman and Conover (1980), which is independent of the mathematical model of a problem. These authors indicated that LHD is usually good and efficient for computer experiments.

LHD has many advantages. It has good one-dimensional projective property. It does better as an unbiased estimator compared with simple random sampling and stratified sampling, since its variance (also called mean square error) is small. It can give much more accurate estimates of the model and with it an estimate of the effect of changing input distribution can be also obtained. Furthermore, it can show relative importance of each input parameter (Iman and Conover 1980). And basically it is computationally cheap to construct and can make the whole design space well covered. (Jin et al. 2003 and Sacks et al. 1989a)

To describe how a Latin hypercube is generated, let us assume again, a vector of  $n$  input parameters  $\mathbf{X} = (X_1, X_2, \dots, X_n)$  and an output response  $Y$ . The relationship between input parameters and output is

$$Y = f(\mathbf{X}) \tag{53}$$

The LH DoE is structured so that each parameter  $X_m$  ( $m = 1, 2, \dots, n$ ) is divided into  $K$  strata of equal marginal probability  $1/K$ . Now there are  $K^n$  cells, and  $K$  sampling points  $(S_1, S_2, \dots, S_K)$  should be chosen from them. In practice, a Latin hypercube can be generated as follows. (Iman and Conover 1980)

Firstly selecting a random number from  $(1, 2, \dots, K)$  on  $X_1$ , matched with a random selected number on  $X_2$ , and so on through  $X_n$ , all these numbers determine the location of

the cell where the first sampling point  $S_1$  is. Then selecting another random number from the remaining set on  $X_1$ , matched with a remaining number randomly selected on  $X_2$ , and so on through  $X_n$ , all these numbers determine the second sampling point  $S_2$ . Repeating this procedure for  $S_3$  to  $S_K$  until all the numbers of  $(1, 2, \dots, K)$  is selected. As a result, a Latin hypercube sample is obtained.

In encoding, the process is a little different. Instead of selecting sampling points one by one, the Latin Hypercube sample is done by generating a random permutation sequence of  $(1, 2, \dots, K)$  on  $X_1$ , matched with a random generated sequence on  $X_2$ , and so on through  $X_n$ . After that the complete set of sampling points  $(S_1, S_2, \dots, S_K)$  is generated. It is much more efficient.

In this way, for each stratum, there is only one sampling point (i.e. experiment), which ensures that the entire range of each input parameter has been sampled.

Furthermore, a random (equally likely) combination of different strata of the different parameters ensures that each stratum of each parameter is somehow possible to couple with strata of other parameters. If there are only two input parameters, it is also named as “Latin square”, and if there are more than two parameters, it is usually called “Latin hypercube sampling”. Figure 5.3 and Figure 5.4 provide examples of LHD in 2D and 3D case, respectively.

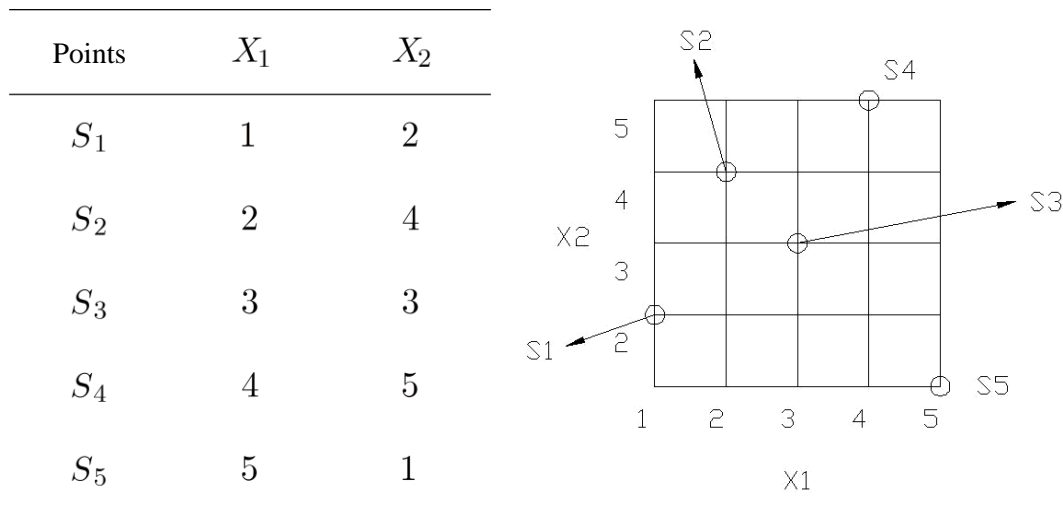


Figure 5.3 Latin hypercube design for  $K=5$  and  $n=2$ .



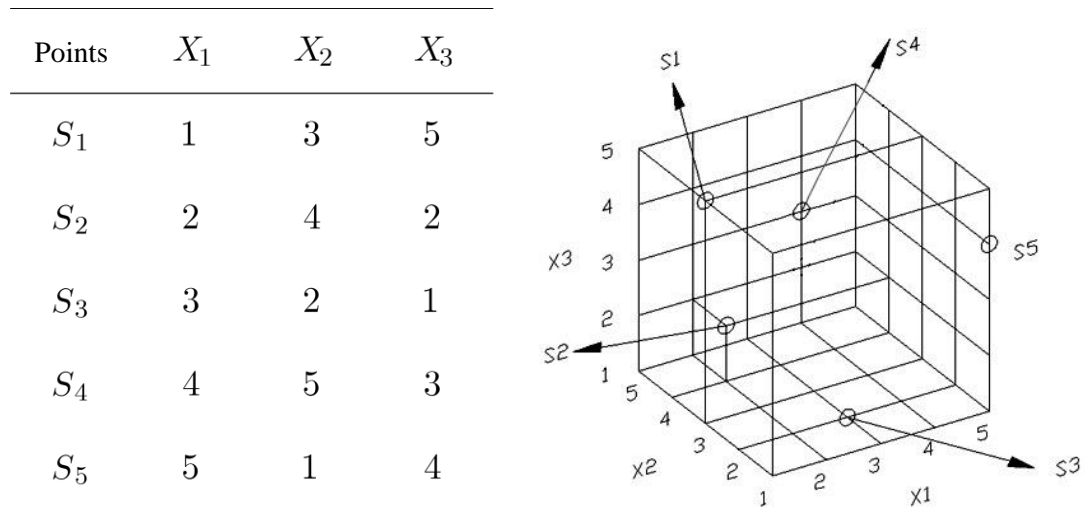


Figure 5.4 Latin hypercube design for  $K=5$  and  $n=3$ .

### 5.1.1 Space-filling Latin Hypercube Designs (LHD)

Space-filling design of experiment is a unique type of DoE. It means to treat the whole design space equally. Through literatures, many researchers have indicated that the sampling points should be selected to fill the whole design space. Moreover, space-filling design becomes necessary especially for non-random, complex, deterministic computer experiments. Since in deterministic computer experiments there is usually no random error, and the lack of random measurement error causes a lot of difficulties in computing and analysis such as the classical notions of experimental blocking, replication and randomization are not appropriate any more. (Sacks et al. 1989b)

Several different criteria have been used to judge the space-filling property of an experimental design, e.g. the integrated mean squared error (IMSE) and the entropy of design region. Based on these criteria, many approaches have been developed to generate space-filling designs.

The maximum entropy principle is used as a rule to create experimental designs by Shewry and Wynn (1987). Johnson et al. (1990) proposed the minimax and maximin designs firstly. Tang (1993) constructs a special Latin hypercube design based on orthogonal arrays, which performs better than the original Latin hypercube designs. Maximin distance design based on Latin hypercube arrangements is proposed by Morris and Mitchell (1995), which is proven to have good projective properties in each dimension.

Park (1994), in his paper, creates a so called optimal Latin hypercube design (OLHD) by combining the ideas of both Latin hypercube design and optimal designs. This OLHD can either maximize the entropy or minimize the IMSE, spreading the sampling points all over the design space.

As mentioned in previous section, Latin hypercube design (LHD), comparing with other experimental design methods, has many advantages. However, since the original LHD normally does not associate with any optimal properties of designs, sometimes it will be poor in evaluating the expected response value or in forecasting the response values at the untried points.

The LHD method can be generally classified into random sampling LH method (RLH) and optimal LH method (OLH) in terms of how the sampling points in DOE are distributed.

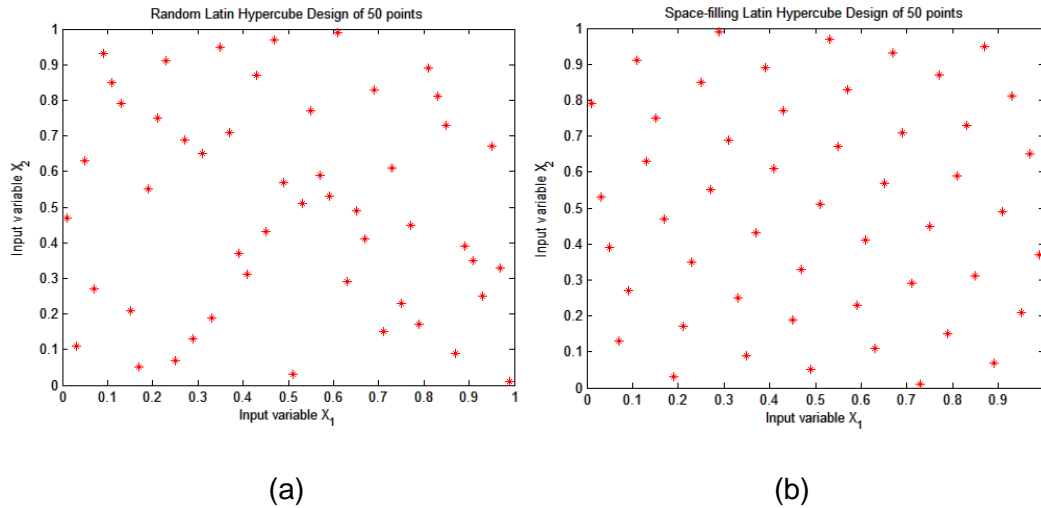


Figure 5.5 Comparison of (a) Random LHD to (b) space-filling LHD.

In the figures above, Figure 5.5(a) shows the random Latin hypercube design with fifty sampling points for two variables (input parameters), while Figure 5.5(b) shows the space-filling Latin hypercube design (also known as uniform LHD or OLHD) with the same number of sampling points and variables.

It can be intuitively seen from the figure that the space-filling LHD would be much better in estimating the response values in the whole design space than the general LHD since the sampling points are uniformly distributed and well covering the whole design space.

In order to construct an optimal Latin hypercube design, some optimality criteria have to be used.

**Maximin or minimax distance criterion:**

A design is called maximin distance design, if it maximizes the minimum inter-site distance:

$$\min_{1 \leq i, j \leq n, i \neq j} d(P_i, P_j) \tag{54}$$

where  $d(P_i, P_j)$  is the distance between two sampling points  $P_i$  and  $P_j$ . And

$$d(P_i, P_j) = d_{ij} = \left[ \sum_{k=1}^m |P_{ik} - P_{jk}|^q \right]^{\frac{1}{q}} \quad (55)$$

in which  $q = 1$  or  $2$ .

It is very easy to understand this criterion. The maximin distance criterion means that for an arbitrary sampling point, the distances from this point to any other points are as far as possible. This criterion will of course lead to a well space-filling design.

And a design is called minimax distance design, if it minimizes the distance between an arbitrary prediction point and its closest sampling point. Since the number of prediction points could be infinite, so in practice it is nearly impossible to use this minimax criterion unless the total number of prediction points is finite. Moreover, it is usually more time-consuming in computation. (Jurecka 2007, Jin et al. 2003, Johnson et al. 1990)

**Entropy criterion:**

Entropy was firstly used by Shannon (in 1948) to qualify the ‘‘amount of information’’. Let the whole design space be a set  $S$ , which is divided into two subsets the sample set  $s$  and its complement set  $\bar{s}$ , ( $s \cup \bar{s} = S, s \cap \bar{s} = \emptyset$ ).  $X_S$  is a vector which refers to the whole design space. And  $X_s$  refers to all sampled points, while  $X_{\bar{s}}$  refers to all points in set  $\bar{s}$ .

For a random variable  $Y$  with density  $f(Y)$  the entropy is defined as

$$Ent(Y) = -E_Y(\log f(Y)) = - \int f(y) \log f(y) dy \quad (56)$$

So the entropy for  $S$  is

$$\begin{aligned} Ent(X_S) &= Ent(X_s) + Ent(X_{\bar{s}}) \\ &= Ent(X_s) + E_{X_s}[Ent(X_{\bar{s}}|X_s)] \end{aligned} \quad (57)$$

where  $X_{\bar{s}}|X_s$  denotes the variable  $X_{\bar{s}}$  conditional on  $X_s$ . The goal of optimization is to minimize the second term on the right hand side of the Equation (57). Since  $Ent(X_S)$  is constant, the goal is turned to be

$$\max Ent(X_s) \quad (58)$$

That is why it is called maximum entropy sampling method (Shewry and Wynn 1987, Currin et al. 1991). The core idea of this criterion is also very simple; it means to get a set of sampling points which contains as much information about the whole design space as possible.

Besides these two criteria, there are also other widely used methods such as IMSE, centered  $L_2$  discrepancy criterion, etc. (Fang et al. 2000, Ye et al. 2000 and Simpson et al. 2001)

In the presented metamodel aided inversion approach, we chose space-filling LHD together with  $2^n$  full factorial designs as the DoE method for the  $n$  dimensional input pa-

parameter space. The space-filling LHD part is generated based on the maximin distance criterion by applying the genetic permutation algorithm (GPA).

## 5.2 Metamodels

As mentioned at the beginning of this chapter, a metamodel is by definition an approximated model of the complex simulation model. It works as a "black box", which means that given a set of input parameters  $\mathbf{X}$ , it will get an output value  $\hat{Y}$ . Researchers have developed a variety of metamodeling formulations in order to meet different requirements in different fields. The widely used metamodels include polynomial regression models (Box and Draper 1987), Kriging models (Sacks et al. 1989b), non-uniform rational B-spline (NURBS), radial basis function models (Dyn et al. 1986), artificial neural networks, etc. (Apley et al. 2006). In this work, the polynomial regression models and Kriging models have been applied for the treatment of observation data and optimization process, respectively. So at first we would like to provide a short overview of these two famous metamodeling techniques. For further interest, one can get more detailed information in (Jurecka 2007, Kleijnen 2009).

### 5.2.1 Response surface models

Response surface models (also called Polynomial regression models) as a common metamodeling approach have been largely applied in the literatures. Each author has his own way to describe it. Box and Draper (1987) describe that "Response surface methodology comprises a group of statistical techniques for empirical model building and model exploitation. By careful design and analysis of experiments, it seeks to relate a response, or output variable, to the levels of a number of predictors, or input variables, that affect it". Myers and Montgomery (1989) define that the response surface method "is a collection of statistical and mathematical techniques useful for developing, improving, and optimizing processes. It also has important applications in the design, development, and formulation of new products, as well as in the improvement of existing product designs".

The polynomial regression model was originally used for analyzing physical experiments. Assuming to have an output response  $Y$ , and all the independent factors  $\mathbf{X}$  which affect  $Y$ . The true relationship between  $\mathbf{X}$  and  $Y$  is

$$Y = f(\mathbf{X}) + \varepsilon \quad (59)$$

where  $\varepsilon$  stands for random observation or experimental errors, which is assumed to be normally distributed with  $\mu = 0$  and  $\sigma^2$ .

Since the true relationship function  $f(\mathbf{X})$  is unknown, a function  $g(\mathbf{X})$  is used as the approximation of  $f(\mathbf{X})$ , and the Equation (59) turns to be

$$Y = g(\mathbf{X}) + \varepsilon \quad (60)$$

Low-order polynomials are often taken as the approximation function  $g(\mathbf{X})$ . A first order polynomial looks like

$$g(\mathbf{X}) = \alpha_0 + \sum_{i=1}^n \alpha_i X_i \quad (61)$$

which is suitable for low curvatures. A second order polynomial has the form

$$g(\mathbf{X}) = \alpha_0 + \sum_{i=1}^n \alpha_i X_i + \sum_{i=1}^n \alpha_{ii} X_i^2 + \sum_{i=1}^n \sum_{j=1, i < j}^n \alpha_{ij} X_i X_j \quad (62)$$

which is suitable for the high curvatures. Since the second order polynomial form also takes the interactions of two input factors into account, it is more common in use. The coefficients  $\alpha_0, \alpha_i, \alpha_{ii}, \alpha_{ij}$  in the formulas can be assembled in one vector  $\alpha$  when using matrix notation. And so the approximation function  $g(\mathbf{X})$  can be written as

$$g(\mathbf{X}) = \alpha^T \mathbb{X} \quad (63)$$

in which

$$\mathbb{X} = [\mathcal{X}_1, \mathcal{X}_2, \dots, \mathcal{X}_{n_\alpha}]^T \quad (64)$$

and each  $\mathcal{X}_i (i = 1, 2, \dots, n_\alpha)$  is called a regressor, which is an independent function of  $\mathbf{X}$ .

And the coefficients can be obtained by least squares regression analysis while fitting the approximation model to the selected training data.

Assuming we have  $k$  response values (assembled in vector  $\tilde{\mathbf{Y}}$ ) obtained by running the original complex model at sampling points  $\mathbf{X}^l (l = 1, 2, \dots, k)$ , the Equation (60) can be written as

$$\tilde{\mathbf{Y}} = \mathbf{F}\alpha + \mathbf{e} \quad (65)$$

in which

$$\mathbf{F} = \begin{bmatrix} \mathcal{X}_1^1 & \mathcal{X}_2^1 & \dots & \mathcal{X}_{n_\alpha}^1 \\ \mathcal{X}_1^2 & \mathcal{X}_2^2 & \dots & \mathcal{X}_{n_\alpha}^2 \\ \vdots & \vdots & \ddots & \vdots \\ \mathcal{X}_1^k & \mathcal{X}_2^k & \dots & \mathcal{X}_{n_\alpha}^k \end{bmatrix} \quad (66)$$

The least squares regression analysis is trying to get the coefficients by minimizing the sum of squared residuals  $\mathbf{e}^T \mathbf{e}$ , which means nothing but

$$\min_{\alpha} (\tilde{\mathbf{Y}} - \mathbf{F}\alpha)^T (\tilde{\mathbf{Y}} - \mathbf{F}\alpha) \quad (67)$$

By applying the necessary condition at the minimum, Equation (67) can be written as

$$\left. \frac{\partial ((\tilde{\mathbf{Y}} - \mathbf{F}\alpha)^T (\tilde{\mathbf{Y}} - \mathbf{F}\alpha))}{\partial \alpha} \right|_{\hat{\alpha}} = 0 \quad (68)$$

which is

$$\left. \frac{\partial(\tilde{\mathbf{Y}}^T\tilde{\mathbf{Y}} - (\mathbf{F}\boldsymbol{\alpha})^T\tilde{\mathbf{Y}} - \tilde{\mathbf{Y}}^T\mathbf{F}\boldsymbol{\alpha} + (\mathbf{F}\boldsymbol{\alpha})^T\mathbf{F}\boldsymbol{\alpha})}{\partial\boldsymbol{\alpha}} \right|_{\hat{\boldsymbol{\alpha}}} = 0 \quad (69)$$

which gives

$$\mathbf{F}^T\mathbf{F}\hat{\boldsymbol{\alpha}} - \mathbf{F}^T\tilde{\mathbf{Y}} = 0 \quad (70)$$

if  $\mathbf{F}^T\mathbf{F}$  is invertible, which can be easily fulfilled as long as there are at least as many sampling points as the coefficients needed to be evaluated, then we have

$$\hat{\boldsymbol{\alpha}} = (\mathbf{F}^T\mathbf{F})^{-1}\mathbf{F}^T\tilde{\mathbf{Y}} \quad (71)$$

and so

$$\hat{Y} = g(\mathbf{X}) = \hat{\boldsymbol{\alpha}}^T\mathbb{X} \quad (72)$$

## 5.2.2 Kriging model

The Kriging model is another kind of metamodel based on the research of D. G. Krige (1951), which is originally used in the field of geostatistics. It was firstly applied to model the responses of deterministic computer codes by Sacks et al. (1989b), and that is why the Kriging model is also called as DACE model. Nowadays it becomes a very famous and commonly used metamodel technique, which has been applied in many different fields of science and engineering.

In Kriging model, the relationship between input variables  $\mathbf{X}$  and output  $Y$  has the following form:

$$Y = g(\mathbf{X}) + Z(\mathbf{X}) + \varepsilon \quad (73)$$

where  $g(\mathbf{X})$  is a polynomial term as defined in Equation (63),  $Z(\mathbf{X})$  is assumed to be a normally distributed random process term with  $\mu = 0$ ,  $\sigma^2$  and nonzero covariance, and  $\varepsilon$ , the approximation error.

The key idea of the Kriging model is to use a combination of polynomial model and a random process to model the response values  $Y$ . The polynomial term  $g(\mathbf{X})$  provides a general trend of the true underlying function, and by introducing the Gaussian random term  $Z(\mathbf{X})$ , the Kriging model can obtain exactly the same interpolation values  $\hat{\mathbf{Y}}$  as the responses  $\tilde{\mathbf{Y}}$  produced by the original underlying function at all the sampling points. That is to say, for the sampling points  $\mathbf{X}^l (l = 1, 2, \dots, k)$ ,

$$\tilde{Y}_l - \hat{Y}_l = 0, \quad (l = 1, 2, \dots, k) \quad (74)$$

The covariance matrix of the Gaussian random term  $Z(\mathbf{X})$  is defined by

$$Cov(Z(\mathbf{X}^i), Y(\mathbf{X}^j)) = \sigma^2\mathbf{R} \quad (75)$$

where  $\mathbf{R}$  is the correlation matrix defined by

$$\mathbf{R} = [R(\mathbf{X}^i, \mathbf{X}^j)], \quad 1 \leq (i, j) \leq k \quad (76)$$

in which  $R(\mathbf{X}^i, \mathbf{X}^j)$  represents the correlation function between any two sampling points

$\mathbf{X}^i$  and  $\mathbf{X}^j$  of the whole set.

The form of the correlation function is user-specified. In principle, one could choose any functions as long as they satisfy the conditions that  $R(\mathbf{X}^i, \mathbf{X}^j) = R(\mathbf{X}^j, \mathbf{X}^i)$  and  $R(\mathbf{X}^i, \mathbf{X}^i) = 1$ , so that the correlation matrix  $\mathbf{R}$  is a  $k \times k$  symmetric matrix with all ones along the main diagonal. Here in this thesis, we apply the Gaussian correlation expressed by:

$$R(\mathbf{X}^i, \mathbf{X}^j) = \exp \left[ \sum_{w=1}^n \theta_w (X_w^i - X_w^j)^2 \right] \quad (77)$$

in which  $\theta_w$  is the undetermined so-called correlation parameter used to fit the model,  $X_w^i$  and  $X_w^j$  are the  $w^{\text{th}}$  component of the sampling point  $\mathbf{X}^i$  and  $\mathbf{X}^j$ , respectively.

Since the assumed  $Z(\mathbf{X})$  is a Gaussian random process, so the parameters  $\alpha$ ,  $\sigma^2$  and  $\theta$  can be solved by applying the maximum likelihood estimation. Assuming we have a vector  $\tilde{\mathbf{Y}}$  of the response values obtained at all the sampling points  $\mathbf{X}^l (l = 1, 2, \dots, k)$ , the corresponding likelihood function can be written as

$$L(\alpha, \sigma^2, \theta | \tilde{\mathbf{Y}}) = \frac{1}{\sigma^k \sqrt{|\mathbf{R}|} (2\pi)^k} \exp \left( -\frac{1}{2\sigma^2} (\tilde{\mathbf{Y}} - \mathbf{F}\alpha)^T \mathbf{R}^{-1} (\tilde{\mathbf{Y}} - \mathbf{F}\alpha) \right) \quad (78)$$

in which  $\mathbf{F}$  is the matrix defined as Equation (66).

By taking the natural logarithm of  $L$  and applying the necessary condition at the maximum of  $\ln L$  with respect to  $\alpha$  and  $\sigma^2$  respectively, we can get

$$\left. \frac{\partial \ln \left[ \frac{1}{\sigma^k \sqrt{|\mathbf{R}|} (2\pi)^k} \exp \left( -\frac{1}{2\sigma^2} (\tilde{\mathbf{Y}} - \mathbf{F}\alpha)^T \mathbf{R}^{-1} (\tilde{\mathbf{Y}} - \mathbf{F}\alpha) \right) \right]}{\partial \alpha} \right|_{\hat{\alpha}} = 0 \quad (79)$$

$$\left. \frac{\partial \ln \left[ \frac{1}{\sigma^k \sqrt{|\mathbf{R}|} (2\pi)^k} \exp \left( -\frac{1}{2\sigma^2} (\tilde{\mathbf{Y}} - \mathbf{F}\alpha)^T \mathbf{R}^{-1} (\tilde{\mathbf{Y}} - \mathbf{F}\alpha) \right) \right]}{\partial \sigma^2} \right|_{\hat{\sigma}^2} = 0 \quad (80)$$

which are

$$\left. \frac{\partial \ln \frac{1}{\sigma^k \sqrt{|\mathbf{R}|} (2\pi)^k} + \partial \left( -\frac{1}{2\sigma^2} (\tilde{\mathbf{Y}} - \mathbf{F}\alpha)^T \mathbf{R}^{-1} (\tilde{\mathbf{Y}} - \mathbf{F}\alpha) \right)}{\partial \alpha} \right|_{\hat{\alpha}} = 0 \quad (81)$$

$$\left. \frac{\partial \ln \frac{1}{\sigma^k \sqrt{|\mathbf{R}|} (2\pi)^k} + \partial \left( -\frac{1}{2\sigma^2} (\tilde{\mathbf{Y}} - \mathbf{F}\alpha)^T \mathbf{R}^{-1} (\tilde{\mathbf{Y}} - \mathbf{F}\alpha) \right)}{\partial \sigma^2} \right|_{\hat{\sigma}^2} = 0 \quad (82)$$

which give

$$\hat{\alpha} = (\mathbf{F}^T \mathbf{R}^{-1} \mathbf{F})^{-1} \mathbf{F}^T \mathbf{R}^{-1} \tilde{\mathbf{Y}} \quad (83)$$

$$\hat{\sigma}^2 = \frac{1}{k} (\tilde{\mathbf{Y}} - \mathbf{F}\hat{\alpha})^T \mathbf{R}^{-1} (\tilde{\mathbf{Y}} - \mathbf{F}\hat{\alpha}) \quad (84)$$

Based on these two parameters, the third parameter  $\hat{\theta}$  can be determined by maximizing (Booker et al. 1995)

$$\max \left( -\frac{k}{2} (\ln \hat{\sigma}^2 + \ln |\mathbf{R}|) \right) \quad (85)$$

and it is usually solved numerically by applying optimization algorithms.

With all the three parameters at hand, the approximation of the original underlying function can be determined by

$$\hat{Y} = \hat{\alpha}^T \mathbb{X} + \mathbf{r}^T(\mathbf{X}) \mathbf{R}^{-1} (\tilde{\mathbf{Y}} - \mathbf{F} \hat{\alpha}) \quad (86)$$

in which  $\mathbf{r}(\mathbf{X})$  is the correlation vector

$$\mathbf{r}(\mathbf{X}) = \left[ R(\mathbf{X}, \mathbf{X}^1), R(\mathbf{X}, \mathbf{X}^2), \dots, R(\mathbf{X}, \mathbf{X}^k) \right]^T \quad (87)$$

that consists of all the individual correlations between the current point  $\mathbf{X}$  and each sampling point  $\mathbf{X}^l (l = 1, 2, \dots, k)$ .

### 5.3 Update procedures to improve quality of the meta-model

When the metamodel, instead of the original underlying function, is used in the optimization procedure for inversion, there is a main problem needed to be solved, which is the possible uncertainty or error of the approximated response values, since all the judgments used in the optimization algorithm depend on these values. In other words, the quality of the metamodel has to be good enough in order to make the inversion results meaningful and trustable.

Generally speaking, the more sampling points are used, the better the quality of the metamodel will be. However, including too many sampling points will significantly increase the calculation time and the memory use. Thus, we need to find a compromised way to maintain the effectiveness as well as the efficiency of the metamodel simultaneously.

Since what we want is to find the minimum of the underlying function, so we do not have to make a metamodel that is accurate everywhere, instead, what we need is a metamodel that has a relatively good approximation to the original function near its true minimum.

According to this goal, there are two major cases which we need to focus on. The first case is that the true minimum of the underlying function has been captured by the metamodel, and it is smaller than any response values taken at the sampling points, which means

$$\exists \hat{Y}_{min} < \min (\hat{Y}_1, \hat{Y}_2, \dots, \hat{Y}_k) \quad (88)$$

And the second case is that the true minimum has been missed because the approximation errors of the metamodel at the position where the true minimum is are too large.



Therefore, to improve the quality of the metamodel near the minimum, more sampling points ought to be added at such positions where either have smaller response values or have large inaccuracy. Many different updating approaches have been developed based on this idea. (Sasena et al. 2002, Regis and Shoemaker 2005, Wang 2003, Toropov et al. 2007)

Here in this thesis, we adopted the so-called efficient global optimization method, which was firstly proposed by Jones et al (1998). It considers the both cases mentioned above while determines the positions where to put new sampling points. And the key idea of the efficient global optimization method is to maximize the expected improvement (Schonlau 1997) of the current metamodel.

The expected improvement used here is so defined. Assuming we have a metamodel (more precisely a Kriging model) trained by a set of sampling points  $\mathbf{X}^l (l = 1, 2, \dots, k)$  and the corresponding response values  $\tilde{Y}^l (l = 1, 2, \dots, k)$ . The minimum of all the response values is denoted as  $\tilde{Y}_{co}$ , and it also can be called the optimum of the current metamodel.

For a Kriging model, by definition, every approximated value is a Gaussian random process  $\mathbb{Y} \sim N(\hat{Y}, \hat{s}^2)$ , where  $\hat{Y}$  is the approximated mean value, and  $\hat{s}^2$  is the estimated variance of the approximation error, which can be determined as follows by applying the mean squared error

$$\hat{s}^2 = \text{MSE}(\hat{Y}) = \hat{\sigma}^2 \left( 1 - \begin{bmatrix} \mathbb{X}^T & \mathbf{r}^T(\mathbf{X}) \end{bmatrix} \begin{bmatrix} \mathbf{0} & \mathbf{F}^T \\ \mathbf{F} & \mathbf{R} \end{bmatrix} \begin{bmatrix} \mathbb{X} \\ \mathbf{r}(\mathbf{X}) \end{bmatrix} \right) \quad (89)$$

in which all the symbols are the same as in Equation (64), (66), (76) and (87). Then the improvement of any approximation value can be defined as

$$I = \max \{ (0, (\tilde{Y}_{co} - \mathbb{Y})) \} \quad (90)$$

And so the expected improvement is defined as below

$$E(I) = E(\max \{ (0, (\tilde{Y}_{co} - \mathbb{Y})) \}) \quad (91)$$

which is the expectation of the improvement defined in Equation (90). Assuming the probability density function of the Gaussian random process  $\mathbb{Y}$  is denoted as  $p_{\mathbb{Y}}$ , then the expected improvement can be written as

$$E(I) = \int_{-\infty}^{\tilde{Y}_{co}} (\tilde{Y}_{co} - Y) p_{\mathbb{Y}}(Y) dY = (\tilde{Y}_{co} - \hat{Y}) \Phi \left( \frac{\tilde{Y}_{co} - \hat{Y}}{\hat{s}} \right) + \hat{s} \phi \left( \frac{\tilde{Y}_{co} - \hat{Y}}{\hat{s}} \right) \quad (92)$$

in which  $\Phi$  and  $\phi$  are the cumulative density function and the probability density function of the standard normal distribution  $N(0, 1)$ , respectively.

From Equation (92), it is obvious to see that the first term will be large when the new approximated mean value  $\hat{Y}$  is a real improvement regarding the current optimum  $\tilde{Y}_{co}$  and at the same time the approximation error is relative small, while the second term will be large when the approximation error is large. And so this criterion meets our requirements of finding the suitable positions to put new sampling points quite well.

The whole updating procedure works as follows:

1. An initial metamodel was trained by an initial set of sampling points and their corresponding response values.
2. Get the current optimum of the metamodel.
3. Based on the current optimum, maximize the expected improvement of the current metamodel.
4. Add a new sampling point at the position where the maximal expected improvement locates.
5. Run the original model to obtain the corresponding response value (observation) of the new added sampling point.
6. Update the metamodel with the new set of sampling points and response values.
7. Go to 2.

The loop will continue until the maximum of expected improvement is smaller than a given threshold value, then we can get the willing optimum of the metamodel, which should also be a good approximation of the optimum of the original underlying function. Furthermore, since the maximum of expected improvement is not monotone decreasing during the metamodel updating process, the average value of the last several iterations is used for the stopping criterion.

Among all the steps listed above, the most important one is the maximization of the expected improvement of the metamodel, which is a highly nonlinear optimization problem. In order to avoid the drawbacks of possibly present local minima, the so-called Particle Swarm Optimization (PSO) algorithm (Kennedy and Eberhart 1995) is applied here. And it has been proven by many literatures that the PSO algorithm is very suitable to deal with such nonlinear multi-parameter optimization problems. More detailed information can be found in (Parsopoulos and Vrahatis 2002, Yang 2009).

## Chapter 6

### Application Examples

---

In this chapter, the metamodel-based inversion approach proposed in Figure 1.1 is tested on several interpretive examples. To show the inversion ability and effectiveness of the metamodel-based approach, firstly, three synthetic examples are presented. Thereafter, the approach is applied to a real geophysical application example about the Long Valley Caldera in California.

#### 6.1 Synthetic examples

##### 6.1.1 FE model without topography

In the first synthetic example, the topography is not taken into account, so that the inversion results of the FE model can be easily verified by comparing with the corresponding analytical solutions.

We use the commercial code ANSYS<sup>®</sup> version 12.1 to establish the finite element models. We consider a 3D cubic geometry that is 20 km long, 20 km wide and 15 km deep. The top surface of the cubic stands for the ground. The region we are interested in is a  $5 \times 5$  km<sup>2</sup> square in the middle of the top surface, and to gain accurate results of surface deformation, a finer mesh is used. For those uninterested parts, a relative coarse mesh is applied, in order to reduce the number of elements and save the calculation time. The total dimension of the model is chosen to be large enough, in order to avoid the influences of the boundary conditions on the surface deformation results.

For the modeling of volcanic source, two different models are applied, i.e. a spherical cavity at certain depth is modeled as the magma chamber for the 4-parameter Mogi source, and a dipping prolate spheroidal cavity at certain depth is modeled for the 8-parameter Yang's source. For both cases, we assume a constant inner pressure change  $\Delta P$  as loading case. The models are meshed with 3-D 10-node tetrahedral elements. For the model with Mogi source, there are 35558 elements in total, and for the model with Yang's source, it has a total of 33078 elements. The FE model setup is shown in Figure 6.1.

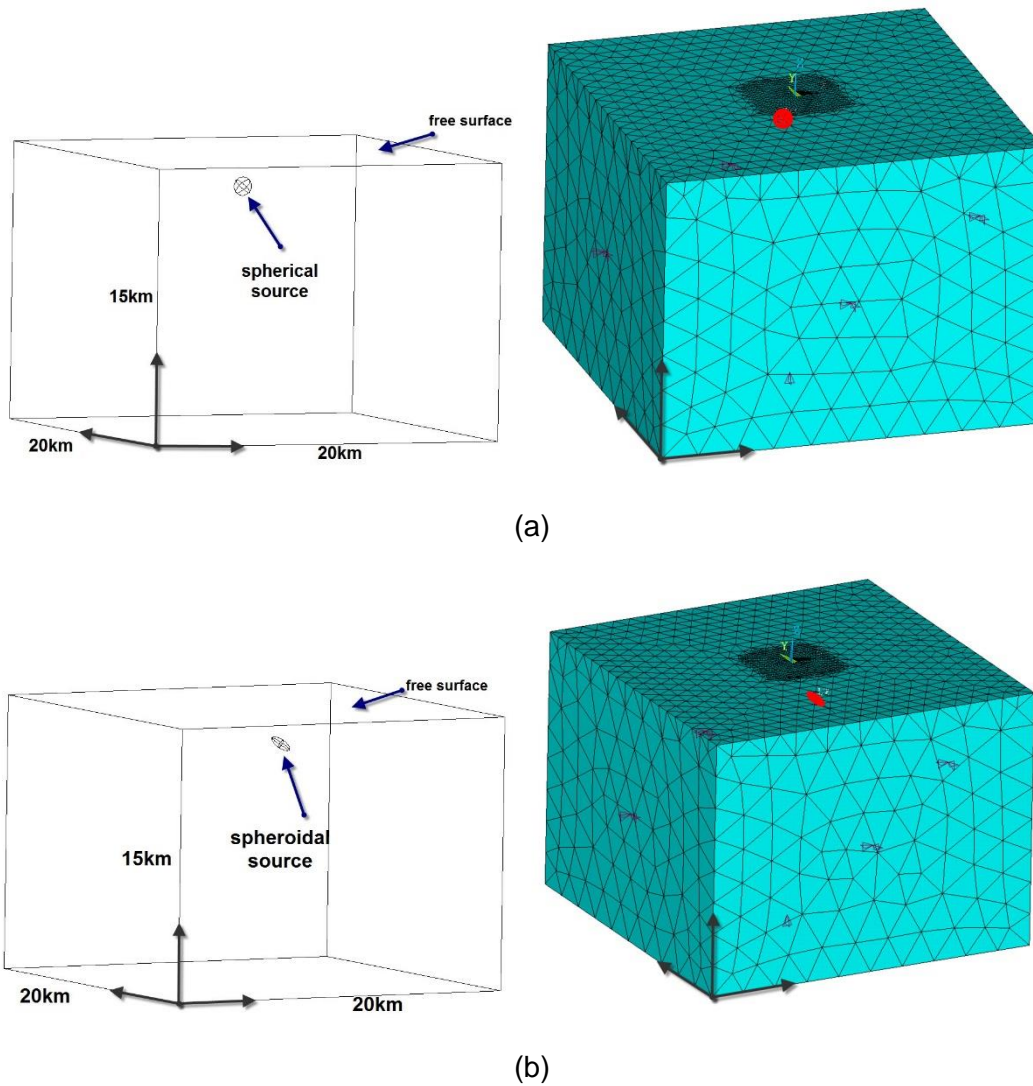


Figure 6.1 (a) The setup of the FE model for the spherical source case. (b) The setup of FE model for the prolate spheroidal source case.

For the Mogi source, we assume the radius of the cavity is a constant (0.5 km), so the four chosen parameters are the inner pressure change  $\Delta P$  and the coordinates of the source center  $(x_0, y_0, d)$ ; for the Yang's model, the chosen parameters are semi-major axis  $a$ , the semi-minor axis  $b$ , the inner pressure change  $\Delta P$ , the location of source center  $(x_0, y_0, d)$ , the dipping angle  $\theta$  and the strike angle  $\phi$ .

As boundary conditions, we assume zero normal displacements for all the side and bottom faces of the model. For the material properties, we assume a Young's modulus of 2.5 GPa in the whole domain and a Poisson's ratio of 0.25, that are, common values for rocks. The numerical solution of the FE model has been validated by comparing results calculated by the related Mogi and Yang's model.

For testing the metamodel-based inversion approach, we generated two sets of synthetic data of the observed surface deformation with the parameter sets listed in Table 6-1.

Moreover, to be realistic, we add a random noise to the synthetic observed data. The random noise has a Gaussian distribution with mean zero, and its maximum value is equal to 20% of the maximal vertical surface deformation.

Table 6-1 Parameters used to generate the synthetic surface deformation data.

(a) Spherical source:

$\Delta P$ (Pa)	$x_0$ (km)	$y_0$ (km)	$d$ (km)
$-3 \times 10^6$	0	2	2

(b) Spheroidal source:

$a$ (km)	$b/a$	$\Delta P$ (Pa)	$x_0$ (km)	$y_0$ (km)	$d$ (km)	$\theta$ ( $^\circ$ )	$\phi$ ( $^\circ$ )
0.6	0.4	$-3 \times 10^6$	1	-1	2	30	50

From the observed surface deformation data, 120 investigation points (IPs) (circled in Figure 6.2 and Figure 6.3) are selected using the weighted uniformly selection method mentioned in Chapter 3. The reduced  $\chi^2$  used later in the optimization is calculated with the values of surface deformation taken only on these investigation points.

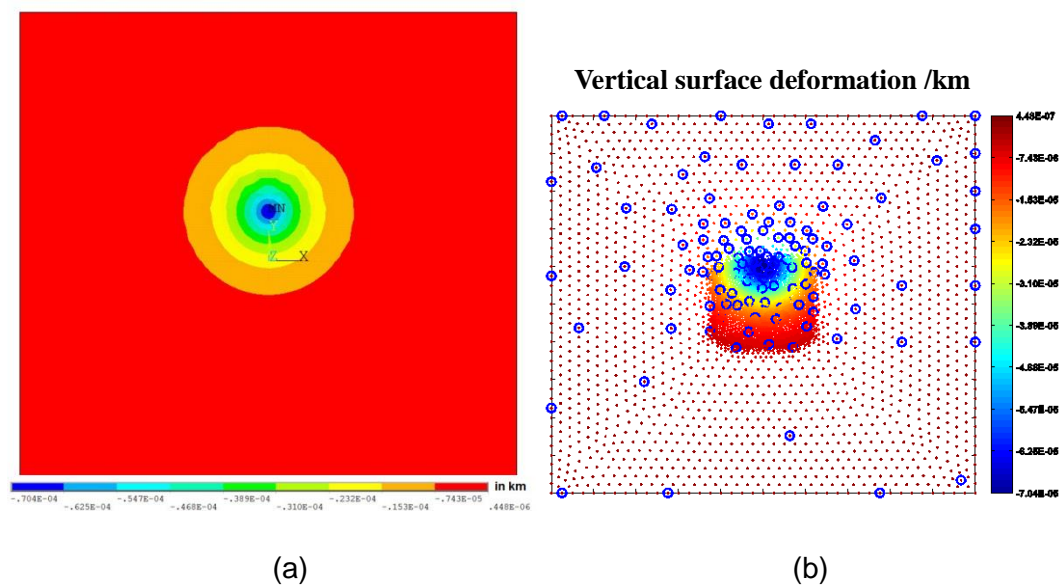


Figure 6.2 (a) Synthetic observed vertical surface deformation. (b) Nodal results of observed vertical surface deformation (dots) and the selected IPs (blue circles) for 4 parameters spherical source.

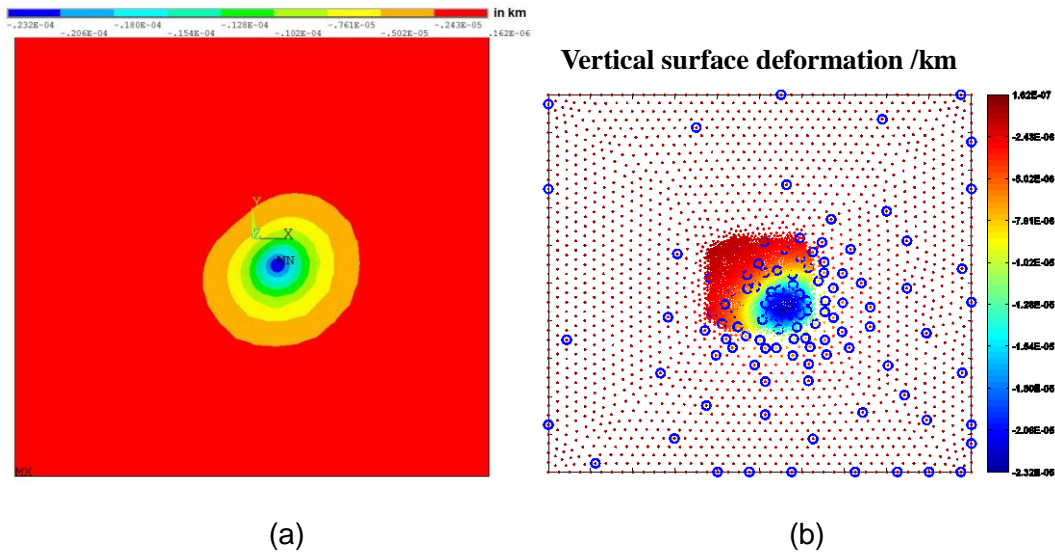


Figure 6.3 (a) Synthetic observed vertical surface deformation. (b) Nodal results of the observed vertical surface deformation (dots) and the selected IPs (blue circles) for 8 parameters Yang's model.

As mentioned in Chapter 5, the metamodel is an approximation of a simulation model, which indicates the functional relationship  $Y = f(\mathbf{X})$  between the input variables  $\mathbf{X}$  and output variable  $Y$  of the original model. Here in this example,  $\mathbf{X} = (\Delta P, x_0, y_0, d)$  for the spherical source case;  $\mathbf{X} = (a, b/a, \Delta P, x_0, y_0, d, \theta, \phi)$  for the spheroidal source case, and  $Y$  represents the reduced  $\chi^2$  calculated by

$$Y = \left( \sum_{k=1}^{N_{IP}} \frac{(U_k(\mathbf{X}) - U_k^{obs})^2}{\sigma^2} \right) / (N_{IP} - N_{par}) \quad (93)$$

where  $N_{IP}$  is the number of selected investigation points,  $U_k(\mathbf{X})$  is the surface deformation at the  $k^{th}$  investigation point calculated by FE model with the input variables  $\mathbf{X}$ ,  $U_k^{obs}$  is the observed surface deformation at the  $k^{th}$  investigation point,  $\sigma^2$  is the variance of the measured error contained in the observed data, and  $N_{par}$  is the number of parameters of the source model.

In order to create the metamodel, a set of sampling points is required. The whole set of sampling points  $\mathbf{X}$  used here consists of two different parts. One part of sampling points  $\mathbf{X}_i (i = 1, 2, \dots, 16 \text{ for 4-parameter case; } i = 1, 2, \dots, 100 \text{ for 8-parameter case})$  have been generated by applying space-filling Latin hypercube design on the corresponding source parameter space. The range of each parameter is listed in Table 6-2. The number of sampling points is related to the dimension of parameter space. In principle, higher dimensional parameter space requires more sampling points, and vice versa. The other part of sampling points  $\mathbf{X}_j (j = 1, 2, \dots, 16 \text{ for 4-parameter case; } j = 1, 2, \dots, 256 \text{ for 8-parameter case})$  are generated by full factorial design, which serves as the supplement of the LHD on the

boundaries of the source parameter space. An initial metamodel  $\hat{Y}$  (more precisely a Kriging model) is created based on these sampling points. Then an updating procedure described in Chapter 5 is applied to improve the quality of the Kriging model by continuously adding new sampling points at the position where it has the maximal expected improvement for the metamodel predictions. By doing so until the maximal expected improvement is smaller than the given threshold value, the minimum of the underlying function  $Y$  can be found, and the corresponding source parameter set is the solution of the inversion.

Table 6-2 Source parameters and their range.

(a) Spherical source:

Source parameter	Unit of Meas.	Range
$\Delta P$	Pa	$[-10^7, -10^6]$
$x_0$	km	$[-5, 5]$
$y_0$	km	$[-5, 5]$
$d$	km	$[1, 10]$

(b) Spheroidal source:

Source parameter	Unit of Meas.	Range
$a$	km	$[0.3, 0.7]$
$b/a$		$[0.1, 0.9]$
$\Delta P$	Pa	$[-10^7, -10^6]$
$x_0$	km	$[-5, 5]$
$y_0$	km	$[-5, 5]$
$d$	km	$[1, 10]$
$\theta$	°	$[0, 180]$
$\phi$	°	$[0, 180]$

The results of inversed source parameters which best fits the synthetic observed surface

deformation data are listed in Table 6-3. And they are compared with the reference values used to generate the synthetic data. It is obvious to see that the inaccuracies (i.e. absolute errors) for each inversed source parameter are different. For some parameters like coordinates  $x_0$ ,  $y_0$  and depth  $d$ , the inversion is quite accurate, while for other parameters such as dipping angle  $\theta$  and striking angle  $\phi$ , the absolute error is a little bit large, that is basically because of the nonuniqueness of the inversion and the trade-offs between parameters previously discussed in Chapter 4.

The surface deformation fields generated by FE model with the best suitable inversed source parameters are compared with the synthetic observed data, and their residuals are shown in Figure 6.4 and Figure 6.5. It can be seen that the results show very good agreements with the observed data, which proves the capability of the proposed approach in solving such nonlinear inversion problems.

In order to illustrate the efficiency advantage of the proposed approach, let's take the inversion of 4-parameter spherical source as an example. It takes on average 109 seconds to run a single FE model. And it takes about 36 seconds for the optimization algorithm to evaluate a new sampling point used for improving the quality of the metamodel. During the entire inversion process, 70 new sampling points has been added, and the FE model has been run 102 times in total (32 times for initial sampling points and 70 times for new added sampling points during updating procedure). So the whole inversion takes about 13638 seconds (i.e. ~3.8 hours) to get the solution. However, if we applied the same optimization algorithm without using metamodels, the FE model would need to be run 50000 times, which means that it would take 5450000 seconds (i.e. ~1514 hours) to get the solution. Through the comparison of calculation time, it is obvious that the proposed approach is very efficient in solving such FE-aided nonlinear inversion problems.

Table 6-3 Results of inversed source parameters.

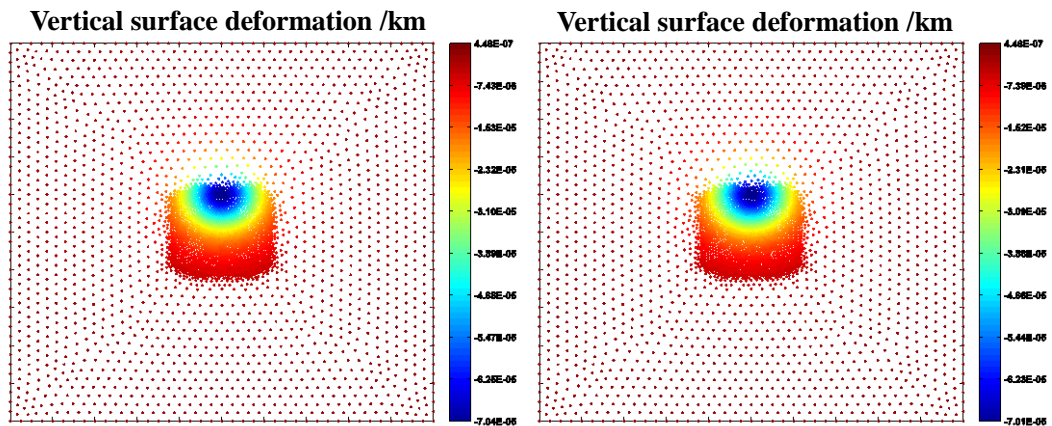
(a) Spherical source:

Parameter	$\Delta P (Pa)$	$x_0 (km)$	$y_0 (km)$	$d (km)$
Inversed value	$-2.982 \times 10^6$	0.0039	1.984	1.999
Reference value	$-3 \times 10^6$	0	2	2
Absolute error	$0.018 \times 10^6$	0.0039	-0.016	-0.001



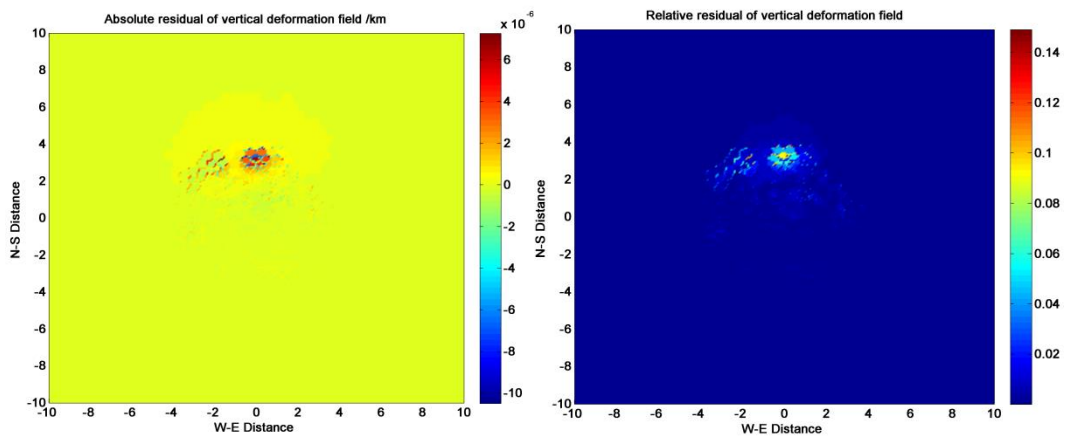
(b) Spheroidal source:

Parameter	$a$ (km)	$b/a$	$\Delta P$ (Pa)	$x_0$ (km)	$y_0$ (km)	$d$ (km)	$\theta$ ( $^\circ$ )	$\phi$ ( $^\circ$ )
Inversed value	0.539	0.612	$-2.092 \times 10^6$	1.003	-1.09	2.035	41.39	85.12
Reference value	0.6	0.4	$-3 \times 10^6$	1	-1	2	30	50
Absolute error	-0.061	0.212	$0.908 \times 10^6$	0.003	-0.09	0.035	11.39	35.12



(a)

(b)



(c)

(d)

Figure 6.4 (a) The synthetic observation data used for the spherical source case. (b) The vertical surface deformation generated by the FE model with the inversed parameters. (c) (d) Absolute and relative residual vertical surface deformation.

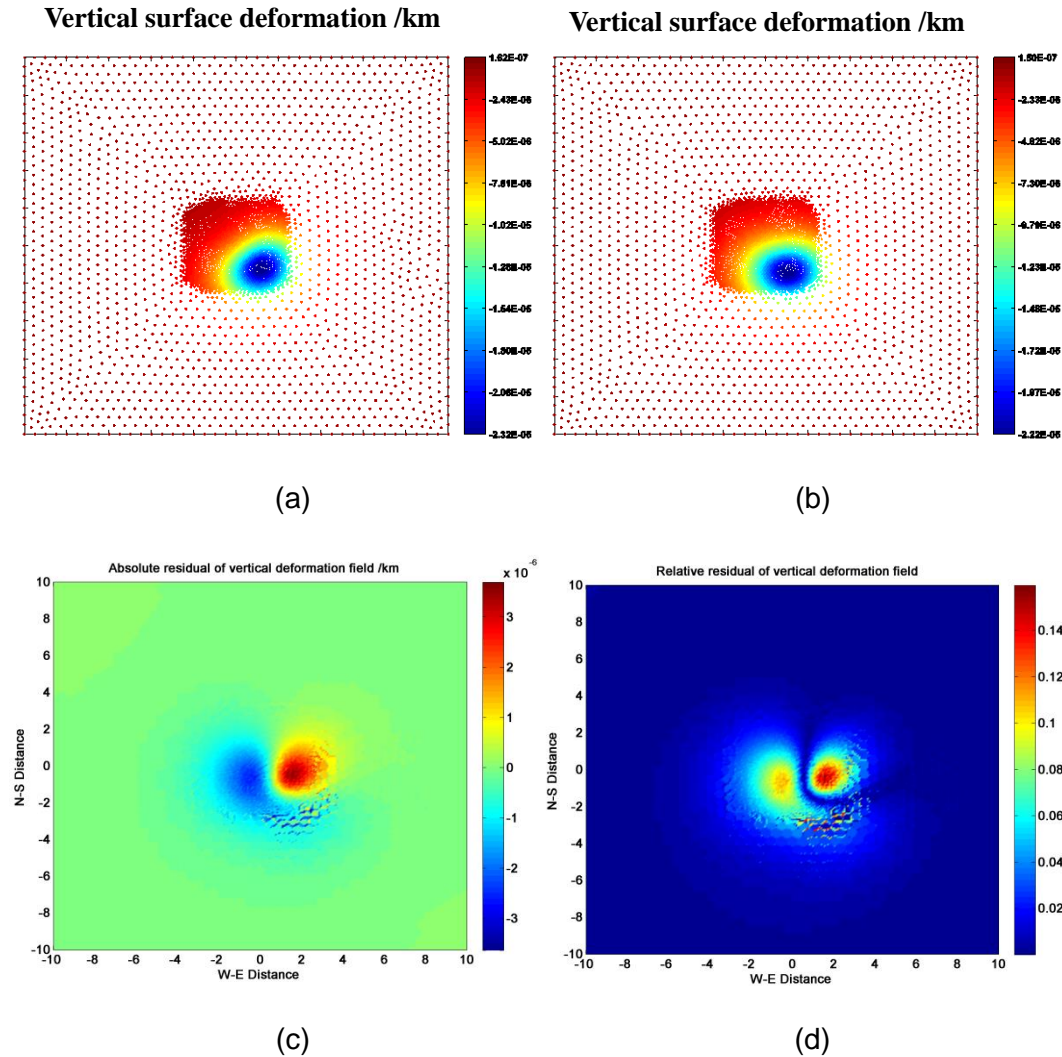


Figure 6.5 (a) The synthetic observation data used for the spheroidal source case. (b) The vertical surface deformation generated by the FE model with the inversed parameters. (c) (d) Absolute and relative residual vertical surface deformation.

### 6.1.2 FE model with topography of caldera

In this example, we will go a little further to consider a more complicated case, a FE model including simplified topography of a caldera and heterogeneous material.

Again, we consider a 3D cubic geometry that is 20 km long, 20 km wide and 15 km deep. In the middle of the top surface, there is a truncated cone-shaped volcano. The height of the volcanic cone is 1 km and the radii of the top and bottom base of the truncated cone are 2 km and 3 km, respectively. Inside the volcanic cone, there is a cylinder-shaped caldera, which has a radius of 1.5 km and a depth of 0.8 km. In order to obtain accurate results of the surface deformation in the interested area, a finer mesh is applied.

Right below the cylinder-shaped caldera, there is a small cylindrical part, which represents the pyroclastic debris layer and usually contains much softer material than other surrounding parts of the volcanic area. This debris layer has a thickness of 0.7 km and a radius of 1.5 km. Its upper surface is 0.2 km above the ground level i.e. the top surface of the cubic.

For the source, here we only took a 4-parameter Mogi source with constant radius of 0.5 km into account. And a constant inner pressure change  $\Delta P$  is considered as loading case. As boundary conditions, we again assume zero normal displacements for all the side and bottom faces of the model. For the material properties, we assume the pyroclastic debris layer consists of elastic material that has a Young's modulus of 30 GPa and Poisson's ratio of 0.25, while the other parts of the model have a Young's modulus of 70 GPa and Poisson's ratio of 0.25. The model is meshed with 3-D 10-node tetrahedral elements, and there are 36259 elements in total. The setup of the FE model can be seen in Figure 6.6.

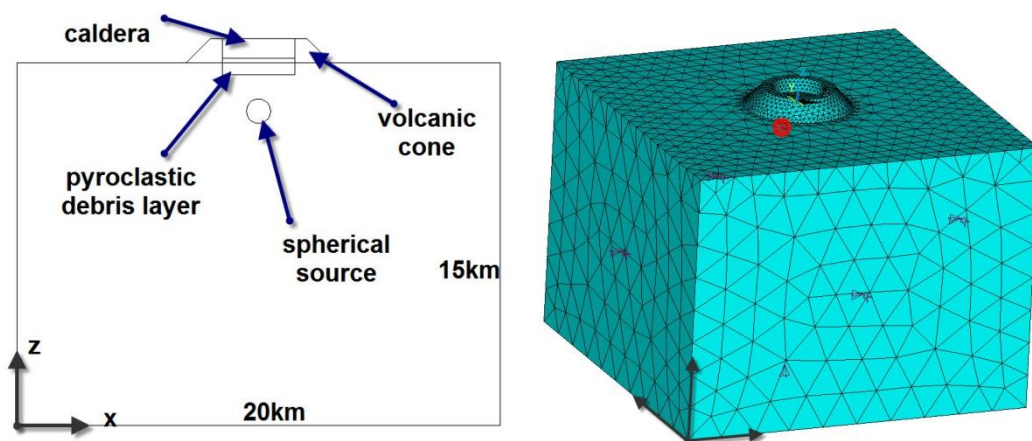


Figure 6.6 Setup of the FE model with topography of caldera.

A set of synthetic data of the observed surface deformation was generated with the parameter set listed in Table 6-4. Again, to be realistic, a random noise was added to the synthetic observed data. The same as in the previous example, in total of 120 investigation points (IPs) are selected based on the observed surface deformation fields. The synthetic data and corresponding selected investigation points (denoted by circles) are shown in Figure 6.7. Furthermore, the initial set of sampling points and related metamodel were created in the same way as previously described in the example for the 4-parameter Mogi source case. The range of all the parameters stays the same (see Table 6-2).

Table 6-4 Parameters used to generate the synthetic surface deformation data.

$\Delta P$ (Pa)	$x_0$ (km)	$y_0$ (km)	$d$ (km)
$-3 \times 10^6$	0	2	2

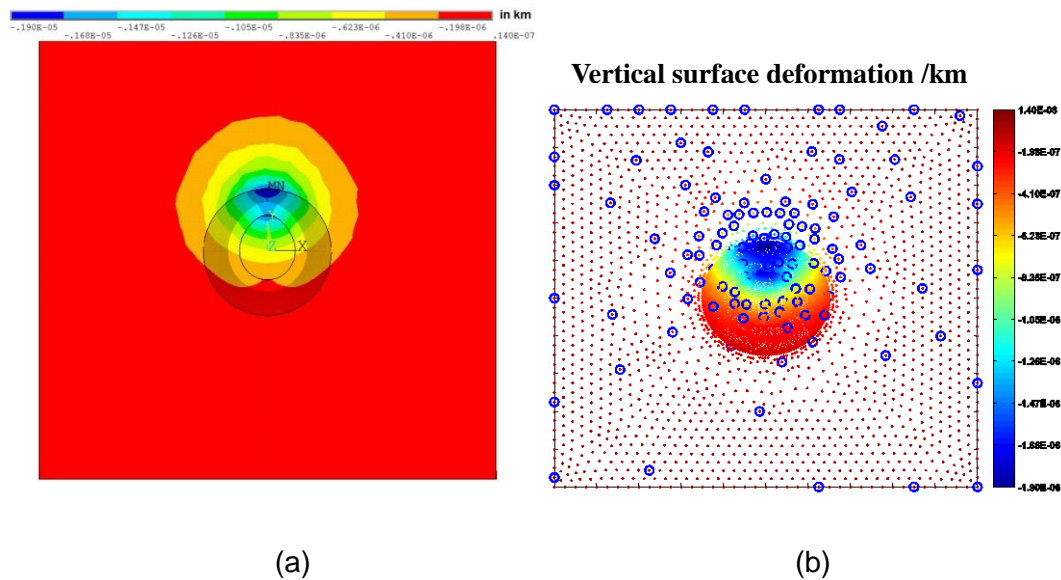


Figure 6.7 (a) Synthetic observed vertical surface deformation. (b) Nodal results of the observed vertical surface deformation (dots) and the selected IPs (blue circles) for 4D spherical source.

In Table 6-5, the inversed results of source parameters are listed and compared with the corresponding reference values. The comparison between surface deformation generated by the set of reference source parameters and the set of inversed ones can be seen in Figure 6.8, which shows quite a good agreement with each other.

Table 6-5 Results of inversed source parameters.

Parameter	$\Delta P$ (Pa)	$x_0$ (km)	$y_0$ (km)	$d$ (km)
Inversed value	$-3.083 \times 10^6$	-0.099	2.01	2.062
Reference value	$-3 \times 10^6$	0	2	2
Absolute error	$-0.083 \times 10^6$	-0.099	0.01	0.062

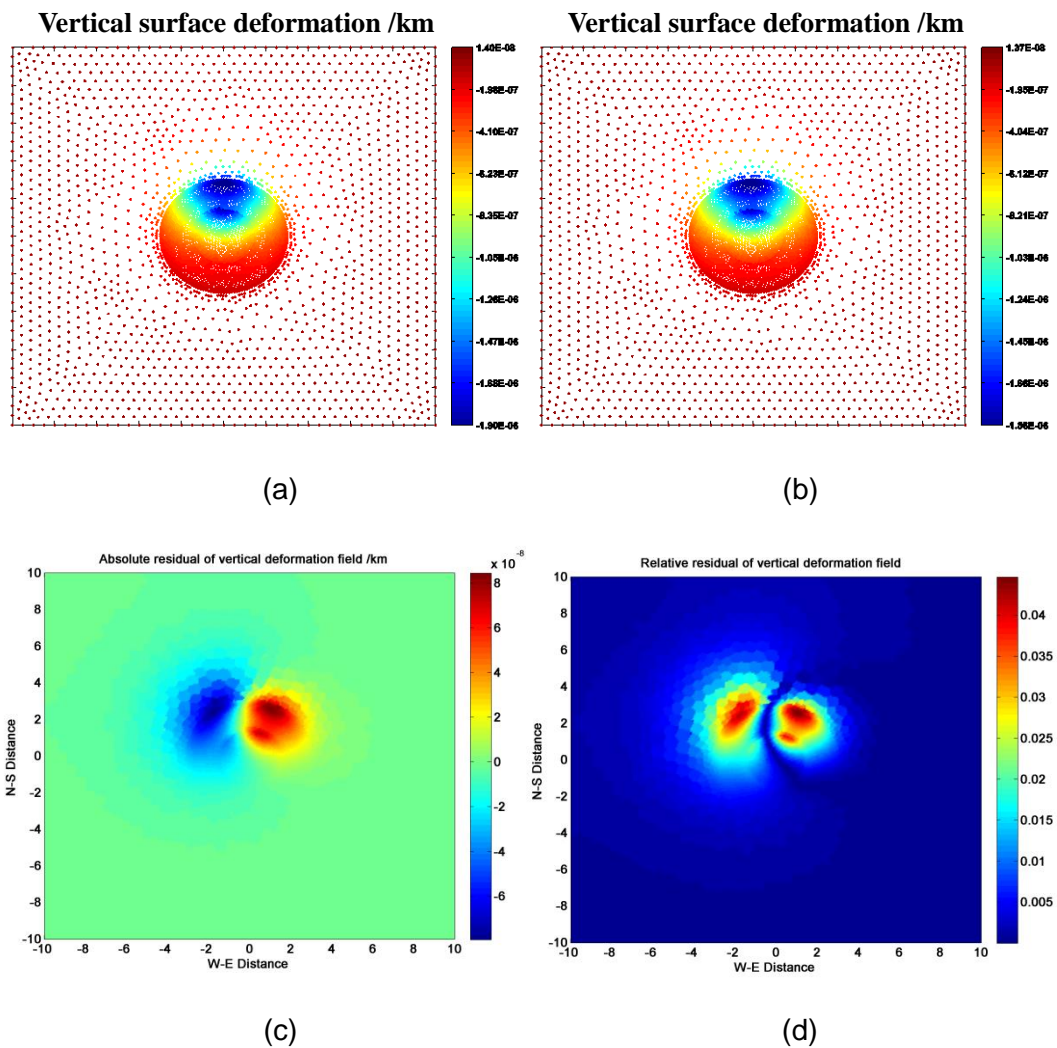


Figure 6.8 (a) The synthetic observation data with topography of caldera used for the spherical source case. (b) The vertical surface deformation generated by the FE model with the inversed parameters. (c) (d) Absolute and relative residual vertical surface deformation.

## 6.2 Long Valley Caldera in California

After seeing those synthetic examples, in this section, a real geophysical application example is used to test the proposed metamodel-based inversion approach. The task is to identify the most suitable set of geophysical parameters that indicate a possible magmatic source, which might cause the recent episodic uplift occurring between 2002 and 2003 at Long Valley Caldera in California.

## 6.2.1 Geological background

The Long Valley Caldera (LVC) locates in the eastern California, which is on the eastern edge of Sierra Nevada range, on the western edge of the Basin and Range province, and about 30 km south of the Mono Lake. The caldera has an elliptical shape, which covers an area of  $32 \times 17 \text{ km}^2$  and has an average height of 2200 m (see Figure 6.9). It was formed more than 700000 years ago as a result of the eruption of the Bishop Tuff. (Tiampo et al. 2000, Newman et al. 2006)

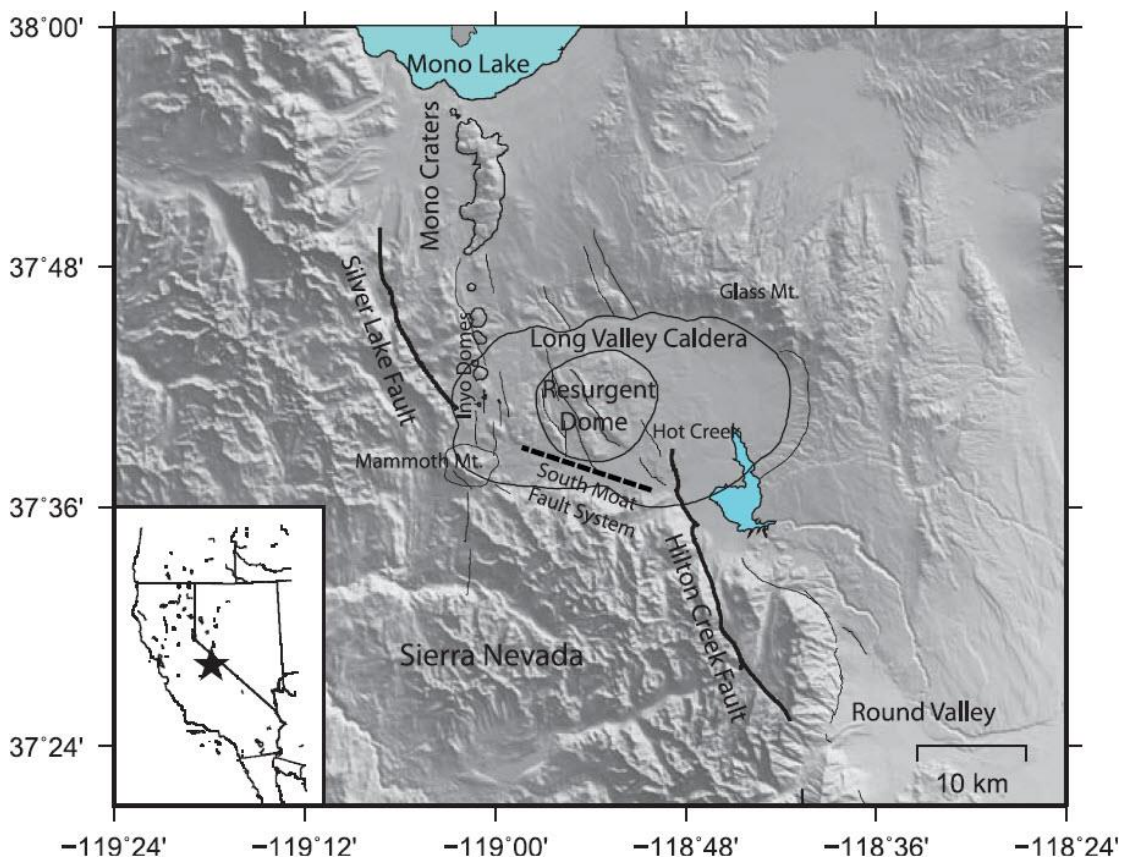


Figure 6.9 Map of Long Valley Caldera, eastern California. (Seccia et al. 2011)

In 2000, the United States Geological Survey (USGS) established a permanent continuous GPS network in and around Long Valley Caldera. As seen from Figure 6.10, the network includes in total 18 GPS stations and the locations of these GPS stations are well distributed. So during the uplift period of 2002-2003, the GPS network provided plenty of new and rich data set of the three-component surface deformation field. (Feng and Newman 2009) And that is why Long Valley Caldera is chosen as an illustrative example here.

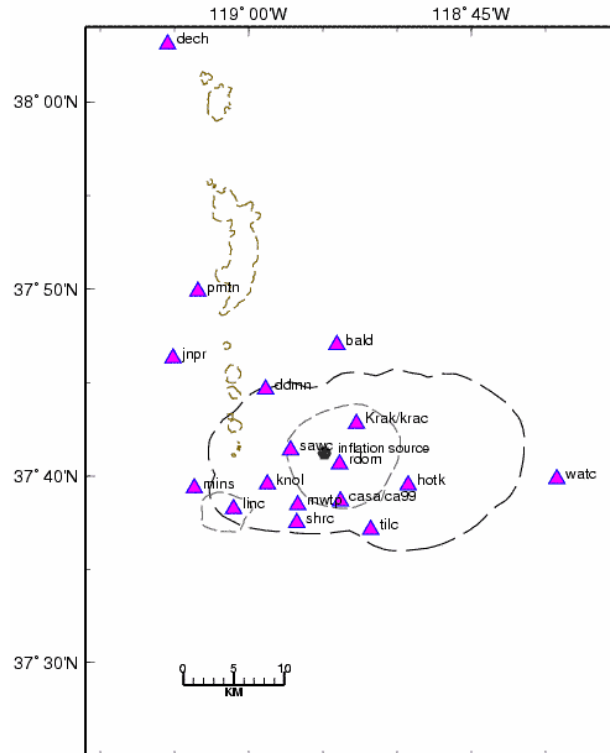


Figure 6.10 Continuous GPS network in and near the Long Valley Caldera<sup>2</sup>.

## 6.2.2 Metamodel based inversion

Again, we use the commercial code ANSYS® version 12.1 to establish the finite element models. This time we consider a 3D cuboid geometry that is 80 km long, 60 km wide and 50 km deep. The top surface of the cuboid stands for the ground, which centers at (340, 4175, 0) in Universal Transverse Mercator (UTM) coordinate system, and no topography is considered. The region we are interested in is a  $40 \times 30$  km<sup>2</sup> rectangular in the middle of the top surface, and to gain accurate results of surface deformation, a finer mesh is used. For the surrounding parts, a relative coarse mesh is applied, so as to reduce the number of elements and save the calculation time. The total dimension of the model is chosen to be large enough, in order to avoid the influences of the boundary conditions on the surface deformation results.

For the source, we only considered a 4-parameter spherical Mogi source with constant radius of 1 km. And a constant inner pressure change  $\Delta P$  is considered as loading case. For boundary conditions, we assume zero normal displacements for all the side and bottom faces of the model. For the material properties, a Young's modulus of 12.5 GPa in the whole domain and a Poisson's ratio of 0.25 (Newman et al. 2006). The setup of the FE model can be seen in Figure 6.11.

<sup>2</sup> <http://earthquake.usgs.gov/monitoring/edm/longvalley/continuous.php>

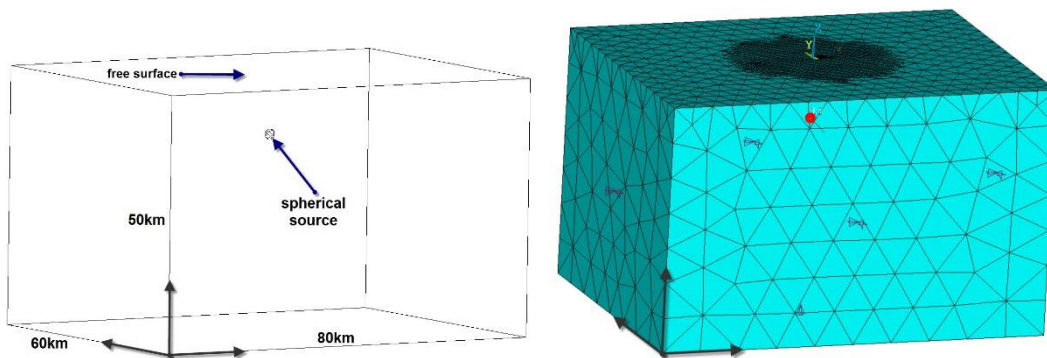


Figure 6.11 Setup of the FE model.

The observed continuous GPS data and the corresponding estimated total error are obtained from Feng and Newman (2009). It has to be mentioned that, since the station DECH is far from the Long Valley Caldera, so its data has been removed from the analysis. Furthermore, due to the influence of the stronger Sierra Nevada bedrocks on the deformation field, the data from station PMTN, JNPR, MINS and LINC are also removed. (Feng and Newman 2009) Thus, only the data of 13 GPS stations are used for inversion and each GPS station is considered as an investigation point (IP) (see Figure 6.12).

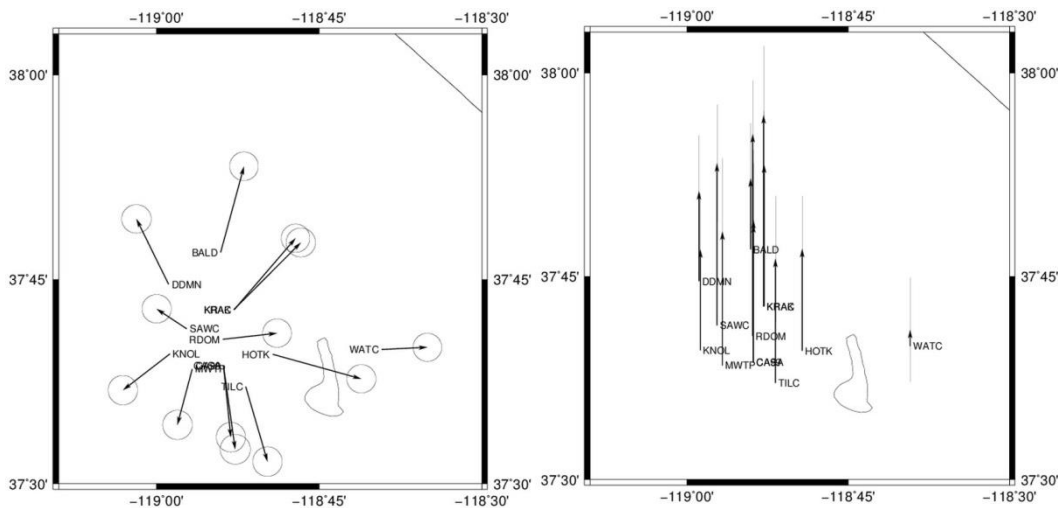


Figure 6.12 Observed horizontal (left) and vertical (right) deformation used in inversion. Ellipses and bars represent 95% confidence error.

An initial set of 32 sampling points is generated as described in section 6.1.1 for the 4-parameter spherical Mogi source case. Based on this, an initial Kriging model is created, and then the updating procedure is applied to improve the quality of the Kriging model until the optimum is found. The range of each source parameter used in inversion is listed in Ta-



ble 6-6.

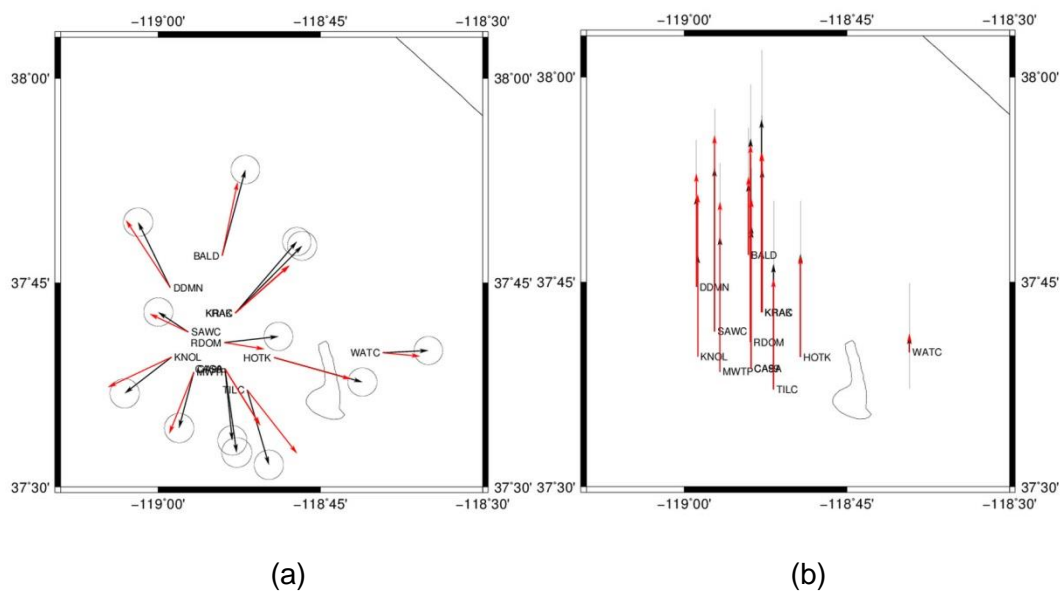
Table 6-6 Source parameters and their range.

Source parameter	Unit of Meas.	Range
$\Delta P$	Pa	$[10^6, 10^8]$
$x_0$	km	$[325, 355]$
$y_0$	km	$[4160, 4190]$
$d$	km	$[6, 20]$

The inversed results of source parameters are listed in Table 6-7. The comparison between the surface deformation generated by the set of inversed parameters and the observed data can be seen in Figure 6.13. It can be seen that, for most GPS stations, the surface deformation fields produced by the inversed parameters are reasonable.

Table 6-7 Results of inversed source parameters based on GPS data.

Parameter	$\Delta P$ (Pa)	$x_0$ (km)	$y_0$ (km)	$d$ (km)
Inversed value	$3.607 \times 10^7$	330.17	4172.1	12.05



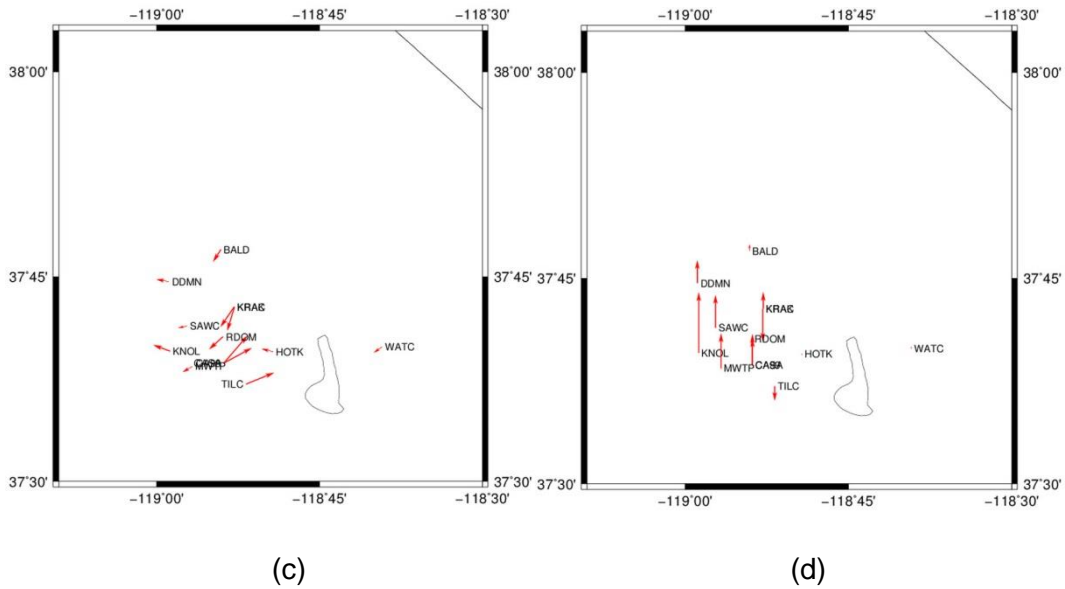


Figure 6.13 Observed (black arrows) and best fit model predicted (red arrows) (a) horizontal and (b) vertical surface deformation. (c) (d) Horizontal and vertical residuals of the best fit model.

Besides the observation data obtained from GPS networks, there are also InSAR data available which observes the 02-03 uplift at Long Valley Caldera (see Figure 6.14a). Here we will apply the proposed approach again to invert the InSAR data. Firstly, 120 investigation points (Figure 6.14b) are selected using the weighted uniformly selection method described in Chapter 3.

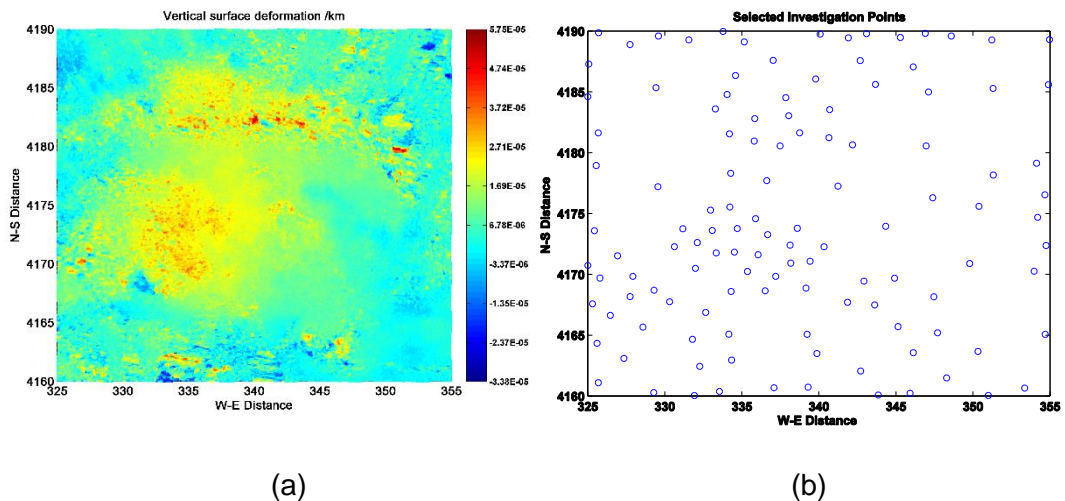


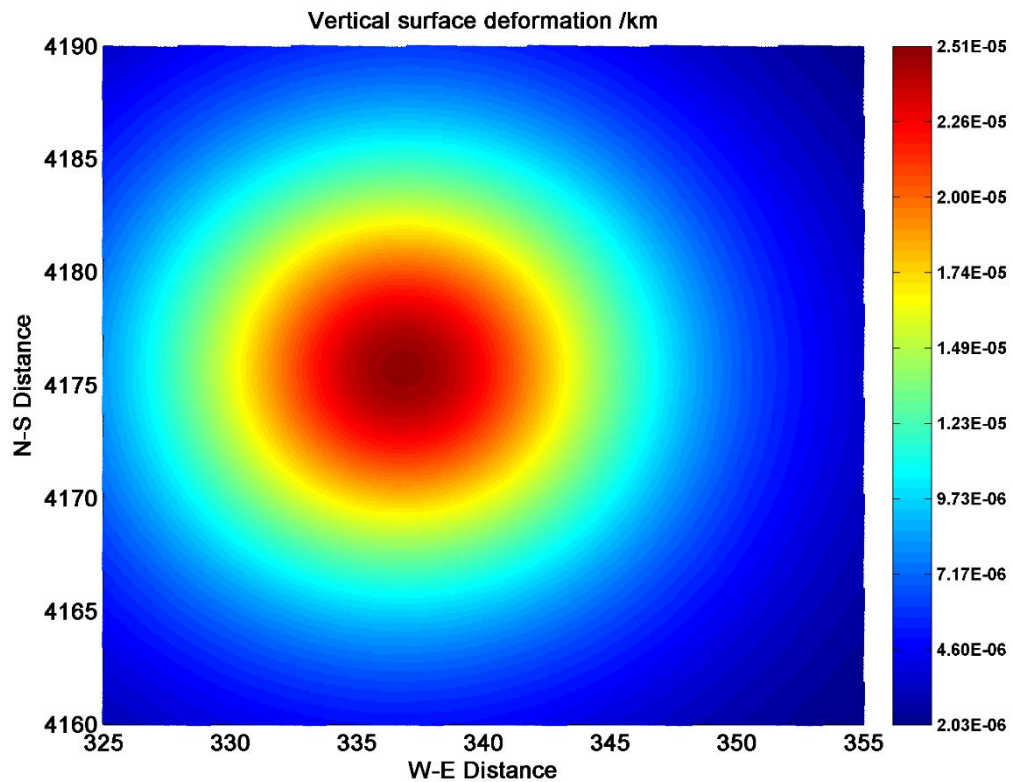
Figure 6.14(a) Observed vertical deformation acquired by InSAR technique (unwrapped). (b) Weighted uniformly selected investigation points (IPs).

Again we assume that the uplift was induced by a 4-parameter spherical Mogi source with constant radius of 1 km. The FE model is the same one shown in Figure 6.11. The material properties and boundary conditions remain the same too. The range of each source parameter used in inversion is listed in Table 6-6.

The inversed results of source parameters are listed in Table 6-8. The comparison between the surface deformation generated by the set of inversed parameters and the observed data are shown in Figure 6.15. It can be seen that, the model with the inversed source parameters is able to fit the InSAR data reasonably well.

Table 6-8 Results of inversed source parameters based on InSAR data.

Parameter	$\Delta P$ (Pa)	$x_0$ (km)	$y_0$ (km)	$d$ (km)
Inversed value	$2.217 \times 10^7$	336.81	4175.7	11.5



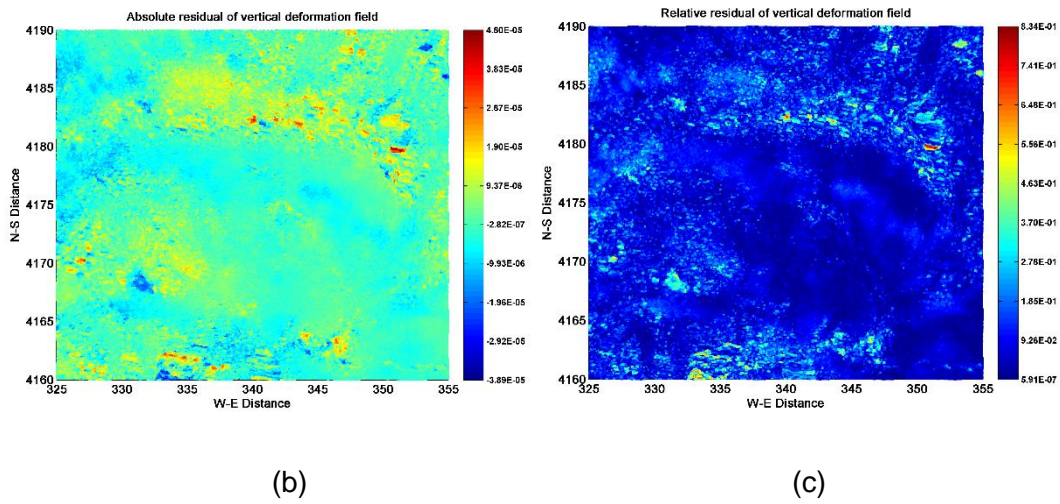


Figure 6.15(a) Vertical surface deformation generated by the FE model with the inverted parameters. (b) (c) Absolute and relative residual vertical surface deformation.

## Chapter 7

### Conclusions and Outlook

---

#### 7.1 Conclusions

In the present dissertation, an integrated method for solving the nonlinear inverse problem by combining metamodel technique together with the finite element technique is proposed and well discussed.

The inverse problem is quite common in scientific and engineering world, especially in the fields of geophysics and geology. The inverse problem is generally hard to solve due to the inexistence, nonuniqueness and instability of its solution.

To solve the inverse problem, a governing equation or model is needed to describe the underlying system. In the application of geophysics and geology, analytical models have been used to represent the complicated geophysical phenomena such as earthquakes, volcanic activities, etc. for many years. These analytical models have made great contributions; however, they are sometimes too simplified. Hence, in recent years, due to their powerful capability and flexibility, the computer simulation methods such as finite element technique have been employed to describe the geophysical system.

As a matter of fact, solving inverse problems is an optimization process, and during the process, the governing equation is required to be evaluated for hundreds or even thousands of times. However, depending on the complexity of a finite element model, it may take minutes to several hours or even days to get a solution. So as to reduce the computational cost, metamodel technique was used here to replace the original complex finite element model in the inversion procedure. Furthermore, in order to ensure the quality of the optimization result, a self-updating procedure was applied.

Generally, in the proposed approach, finite element modeling allows considering more realistic models to describe the geophysical problem and conveniently to simulate the related mechanical behavior; while with the help of metamodels, the efficiency of the whole procedure is greatly improved. Both strengths are essential for real-time applications.

To ensure the performance of the approach, it has been tested with synthetic examples and a real case of Long Valley Caldera in California. The metamodel-based inversion approach can gain relatively good results with reasonable degree of accuracy. However, it also indicates due to the trade-off between parameters, the sole use of one kind of data is not

sufficient to precisely determine all responses. The trade-offs between parameters may also lead to having non-unique solutions. Thus, the more independent types of geophysical data are involved, the better the inversion results will be.

## **7.2 Future work**

There is still a vast unexplored area in the research field of solving geophysical inverse problem, including the following several interesting points:

1. Considering more realistic factors into the finite element model, such as real topography, viscoelastic and/or plastic material, real heterogeneous structure, multiple sources, etc.
2. Using combination of different independent kinds of geophysical data in inversion, such as InSAR, GPS, seismic wave data, gravity field data, electromagnetic data, etc., in order to better constrain the source parameters.
3. Expanding the metamodel based inversion approach to other application fields, such as industrial applications and so on.

## Appendix 1. Further corrections to Yang et al. (1988)

In this appendix, a further correction based on the corrections given by Newman et al. (2006) to the analytical model for surface deformation induced by a dipping prolate spheroidal source embedded in an elastic half-space (Yang et al. 1988) is presented. The correction addressed here was tested by comparing analytical solutions with FEM results for different dipping angles.

Page 4251:

The original equation was

$$U_3^\uparrow = \frac{1}{8\mu(1-\nu)} \frac{ab^2}{c^3} P^\uparrow \{ \cos \theta [-A_1 r_2 + (3 - 4\nu) \bar{A}_1 q_2 + F_1 q_2] + \dots \} \quad (94)$$

And the corrected form should be

$$U_3^\uparrow = \frac{1}{8\mu(1-\nu)} \frac{ab^2}{c^3} P^\uparrow \{ -\cos \theta [A_1 r_2 + (3 - 4\nu) \bar{A}_1 q_2 + F_1 q_2] + \dots \} \quad (95)$$





## Bibliography

- ANDERSSOHN, J., M. MOTAGH, et al., 2009. Surface deformation time series and source modeling for a volcanic complex system based on satellite wide swath and image mode interferometry: The Lazufre system, central Andes. *Remote Sensing of Environment*, 113(10), 2062-2075.
- ANDERSSOHN, J., H.-U. WETZEL, et al., 2008. Land subsidence pattern controlled by old alpine basement faults in the Kashmar Valley, northeast Iran: results from InSAR and levelling. *Geophysical Journal International*, 174(1), 287-294.
- ANDRAE, R., T. SCHULZE-HARTUNG, et al., 2010. Dos and don'ts of reduced chi-squared. *Instrumentation and Methods for Astrophysics*, arXiv:1012.3754.
- APLEY, D. W., J. LIU, et al., 2006. Understanding the Effects of Model Uncertainty in Robust Design With Computer Experiments. *Journal of Mechanical Design*, 128(4), 945-958.
- APUANI, T., C. CORAZZATO, et al., 2005. Stability of a collapsing volcano (Stromboli, Italy): Limit equilibrium analysis and numerical modelling. *Journal of Volcanology and Geothermal Research*, 144(1-4), 191-210.
- APUANI, T., C. CORAZZATO, et al., 2005. Physical and mechanical properties of rock masses at Stromboli: a dataset for volcano instability evaluation. *Bulletin of Engineering Geology and the Environment*, 64(4), 419-431.
- ASTER, R. C., B. BORCHERS, et al., 2005. *Parameter Estimation and Inverse Problems*, Elsevier Academic Press.
- AUDZE, P. and V. EGLAIS, 1977. New approach for planning out of experiments, *Problems of Dynamics and Strengths*, 35, 104-107, Zinatne Publishing House, Riga.
- BAMLER, R. and P. HARTL, 1998. Synthetic Aperture Radar Interferometry. *Inverse Problems*, 14, R1-54.
- BATTAGLIA, J. and P. BACHÈLERY, 2003. Dynamic dyke propagation deduced from tilt variations preceding the March 9, 1998, eruption of the Piton de la Fournaise volcano. *Journal of Volcanology and Geothermal Research*, 120(3-4), 289-310.
- BATTAGLIA, M. and D. P. HILL, 2009. Analytical modeling of gravity changes and crustal deformation at volcanoes: The Long Valley caldera, California, case study. *Tectonophysics*, 471(1-2). 45-57.
- BONACCORSO, A. and P. M. DAVIS, 1999. Models of ground deformation from vertical volcanic conduits with application to eruptions of Mount St. Helens and Mount Etna. *J. Geophys. Res.*, 104(B5), 10531-10542.
- BONACCORSO, A., S. CIANETTI, et al., 2005. Analytical and 3-D numerical modeling of Mt. Etna (It-

- aly) volcano inflation. *Geophys. J. Int.*, 163, 852-862.
- BONACCORSO, A., A. BONFORTE, et al., 2009. Insight on recent Stromboli eruption inferred from terrestrial and satellite ground deformation measurements. *Journal of Volcanology and Geothermal Research*, 182(3-4): 172-181.
- BOOKER, A. J., A. R. CONN, et al., 1995. *Multilevel design optimization: Boeing/IBM/Rice collaborative project*. Final Report, ISSTECH-95-032, The Boeing Company, Seattle, WA
- BOX, G. E. P. and D. W. BEHNKEN, 1960. Some new three level designs for the study of quantitative variables, *Technometrics*, 2(4), 455-475.
- BOX, G. E. P. and N. R. DRAPER, 1987. *Empirical model building and response surfaces*, New York, Wiley.
- BURNHAM, K. P. and D. R. ANDERSON, 2002. *Model Selection and Multimodel Inference: A Practical Information-Theoretic Approach*, Springer-Verlag.
- BUROV, E. B. and A. B. WATTS, 2006. The long-term strength of continental lithosphere: "jelly sandwich" or "crème brûlée"? *GSA today*, 16(1), 4-10.
- CAILLEAU, B., T. R. WALTER, et al., 2003. Modeling volcanic deformation in a regional stress field: Implications for the formation of graben structures on Alba Patera, Mars. *J. Geophys. Res.*, 108.
- CAILLEAU, B., T. R. WALTER, et al., 2005. Unveiling the origin of radial grabens on Alba Patera volcano by finite element modeling. *Icarus*, 176(1), 44-56.
- CASAGLI, N., A. TIBALDI, et al., 2009. Deformation of Stromboli Volcano (Italy) during the 2007 eruption revealed by radar interferometry, numerical modeling and structural geological field data. *Journal of Volcanology and Geothermal Research*, 182(3-4), 182-200.
- CESCA, S., T. BRAUN, et al., 2007. Modeling of the April 5, 2003, Stromboli (Italy) paroxysmal eruption from the inversion of broadband seismic data. *Earth and Planetary Science Letters*, 261(1-2), 164-178.
- CHEN, J.-S. and J.-L. HOU, 2006. A Combination Genetic Algorithm with Applications on Portfolio Optimization. *Advances in Applied Artificial Intelligence*. M. Ali and R. Dapoigny, Springer Berlin Heidelberg. 4031, 197-206.
- CICCOTTI, M. and F. MULARGIA, 2004. Differences between static and dynamic elastic moduli of a typical seismogenic rock. *Geophysical Journal International*, 157(1), 474-477.
- COMMEND, S., F. GEISER, et al., 2004. 3D numerical modeling of a landslide in Switzerland. *NUMERICAL METHODS IN GEOMECHANICS*, 9, 595-602.
- CORAZZATO, C., L. FRANCALANCI, et al., 2008. What controls sheet intrusion in volcanoes? Structure and petrology of the Stromboli sheet complex, Italy. *Journal of Volcanology and Geothermal Research*, 173(1-2), 26-54.
- CORTÉS, J. A., M. WILSON, et al., 2005. The evolution of the magmatic system of Stromboli volcano during the Vancori period (26-13.8 ky). *Journal of Volcanology and Geothermal Research*,

- 147(1-2), 1-38.
- COWIE, P. A., J. R. UNDERHILL, et al., 2005. Spatio-temporal evolution of strain accumulation derived from multi-scale observations of Late Jurassic rifting in the northern North Sea: A critical test of models for lithospheric extension. *Earth and Planetary Science Letters*, 234(3-4), 401-419.
- CURRENTI, G., C. DEL NEGRO, et al., 2008. 3D numerical deformation model of the intrusive event forerunning the 2001 Etna eruption. *Physics of the Earth and Planetary Interiors*, 168(1-2), 88-96.
- CURRENTI, G., C. DEL NEGRO, et al., 2008. Automated procedure for InSAR data inversion using Finite Element Method. *Use of Remote Sensing Techniques for Monitoring Volcanoes and Seismogenic Areas 2008*, USEReST 2008.
- CURRIN, C., T. MITCHELL, et al., 1991. Bayesian predication of deterministic functions, with applications to the design and analysis of computer experiments. *Journal of the American Statistical Association*, 86(416), 953-963.
- DARCY, H., 1856. *Les Fontaines Publiques de la Ville de Dijon*, Dalmont, Paris.
- DAVIS, P. M., L. M. HASTIE, et al., 1974. Stresses within an active volcano – With particular reference to Kilauea. *Tectonophysics*, 22, 363-375.
- DAVIS, P. M., 1986. Surface deformation due to inflation of an arbitrarily oriented triaxial ellipsoidal cavity in an elastic half-space, with reference to Kilauea volcano, Hawaii. *J. Geophys. Res.*, 91, 7429-7438.
- DEL NEGRO, C., G. CURRENTI, et al., 2009. Temperature-dependent viscoelastic modeling of ground deformation: Application to Etna volcano during the 1993-1997 inflation period. *Physics of the Earth and Planetary Interiors*, 172(3-4), 299-309.
- DIXON, T. H., 1991. An introduction to the global positioning system and some geological applications. *Reviews of Geophysics*, 29, 249-276.
- DRAGONI, M. and C. MAGNANENSI, 1989. Displacement and stress produced by a pressurized, spherical magma chamber, surrounded by a viscoelastic shell. *Physics of the Earth and Planetary Interiors*, 56(3-4), 316-328.
- DYN, N., D. LEVIN, et al., 1986. Numerical procedures for surface fitting of scattered data by radial basis functions. *SIAM Journal of Scientific and Statistical Computing*, 7(2), 639-659.
- DZURISIN, D., 2007. *Volcano Deformation: Geodetic Monitoring Techniques*, Springer-Verlag.
- ELLIS, S., J. BEAVAN, et al., 2006. Simplified models of the Alpine Fault seismic cycle: stress transfer in the mid-crust, *Geophys. J. Int.* 166, 386-402.
- ESHELBY, J. D., 1959. The Elastic Field Outside an Ellipsoidal Inclusion. *Proceedings of the Royal Society of London. Series A, Mathematical and Physical Sciences*, 252(1271), 561-569.
- FALSAPERLA, S., G. LANZAFAME, et al., 1999. Regional stress field in the area of Stromboli (Italy): insights into structural data and crustal tectonic earthquakes. *Journal of Volcanology and*

- Geothermal Research*, 88(3), 147-166.
- FALSAPERLA, S. and S. SPAMPINATO, 1999. Tectonic seismicity at Stromboli volcano (Italy) from historical data and seismic records. *Earth and Planetary Science Letters*, 173(4), 425-437.
- FALSAPERLA, S. and S. SPAMPINATO, 2003. Seismic insight into explosive paroxysms at Stromboli volcano, Italy. *Journal of Volcanology and Geothermal Research*, 125(1-2), 137-150.
- FANG, K. T., C. X. MA, et al., 2000. Centered L2-discrepancy of random sampling and Latin hypercube design, and construction of uniform designs, *Mathematics of Computation*, 71(237), 275-296.
- FENG, L. and A. V. NEWMAN, 2009. Constraints on continued episodic inflation at Long Valley Caldera, based on seismic and geodetic observations. *Journal of Geophysical Research: Solid Earth*, 114(B6), B06403.
- FIALKO, Y. and M. SIMONS, 2000. Deformation and seismicity in the Coso geothermal area, Inyo County, California: Observations and modeling using satellite radar interferometry, *J. Geophys. Res.*, 105(B9), 21781-21793.
- FIALKO, Y., Y. KHAZAN, et al., 2001. Deformation due to a pressurized horizontal circular crack in an elastic half-space, with applications to volcano geodesy. *Geophysical Journal International*, 146(1), 181-190.
- FRANCALANCI, L., S. TOMMASINI, et al., 2004. The volcanic activity of Stromboli in the 1906-1998 AD period: mineralogical, geochemical and isotope data relevant to the understanding of the plumbing system. *Journal of Volcanology and Geothermal Research*, 131(1-2), 179-211.
- GIORDANO, G. and M. PORRECA, 2009. Field observations on the initial lava flow and the fracture system developed during the early days of the Stromboli 2007 eruption. *Journal of Volcanology and Geothermal Research*, 182(3-4), 145-154.
- HADAMARD, J., 1902. Sur les problèmes aux dérivées partielles et leur signification physique. *Princeton University Bulletin*, 49-52.
- HAINES, A. J. and W. E. HOLT, 1993. A Procedure for Obtaining the Complete Horizontal Motions Within Zones of Distributed Deformation From the Inversion of Strain Rate Data. *J. Geophys. Res.*, 98(B7), 12057-12082.
- HAMMOND W. C., C. KREEMER, et al., 2010. Effect of viscoelastic postseismic relaxation on estimates of interseismic crustal strain accumulation at Yucca Mountain, Nevada. *Geophysical Research Letters*, 37, L06307.
- HICKEY, J., J. GOTTMANN, et al., 2013. The large-scale surface uplift in the Altiplano-Puna region of Bolivia: A parametric study of source characteristics and crustal rheology using finite element analysis. *Geochem. Geophys. Geosyst.*, 14(3), 540-555.
- HICKEY, J., and J. GOTTMANN, 2014. Benchmarking and developing numerical finite element models of volcanic deformation. *J. Volcanol. Geotherm. Res.*, 280, 126-130.

- HICKEY, J., J. GOTTMANN, et al., 2015. Estimating volcanic deformation source parameters with a finite element inversion: The 2001–2002 unrest at Cotopaxi volcano, Ecuador. *J. Geophys. Res. Solid Earth*, 120, 1473–1486.
- HOFFMANN, J., H. A. ZEBKER, et al., 2001. Seasonal subsidence and rebound in Las Vegas Valley, Nevada, observed by synthetic aperture radar interferometry. *Water Resources Research*, 37(6), 1551-1566.
- HOFMANN-WELLENHOF, B., H. LICHTENEGGER, et al., 2001. *GPS: Theory and Practice (5th edition)*. Springer-Verlag, New York.
- IMAN, R. L. and W. J. CONOVER, 1980. Small sample sensitivity analysis techniques for computer models, with an application to risk assessment, *Communications in Statistics - Theory and Methods*, 9(17), 1749-1842.
- JAQUET, O. and R. CARNIEL, 2003. Multivariate stochastic modeling: towards forecasts of paroxysmal phases at Stromboli. *Journal of Volcanology and Geothermal Research*, 128(1-3), 261-271.
- JIN, R., W. CHEN, et al., 2003. An efficient algorithm for constructing optimal design of computer experiments, *DETC-DAC48760, 2003 ASME Design Automation Conference*, Chicago, IL, September 2-6.
- JOHNSON, M. E., L. M. MOORE, et al., 1990. Minimax and maximin distance designs, *Journal of Statistical Planning and Inference*, 26, 131-148.
- JONES, D. R., M. SCHONLAU, et al., 1998. Efficient global optimization of expensive black-box functions. *Journal of Global Optimization*, 13(4), 455-492.
- JORDAN, T. H., 1979. Structural Geology of the Earth's Interior. *Proceedings of the National Academy of Sciences*, 76(9), 4192–4200.
- JURECKA, F., 2007. *Robust Design Optimization Based on Metamodeling Techniques*. Lehrstuhl für Statik. Munich, Technische Universität München: xiii, 184p.
- KAMPES, B. M., 2006. *Radar interferometry: persistent scatterer technique*. Springer.
- KENNEDY, J. and R. C. EBERHART, 1995. Particle Swarm Optimization. *Proceedings IEEE International Conference on Neural Networks*, IV, 1942-1948. IEEE Service Center, Piscataway, NJ
- KLEIJNEN, J. P. C., 2009. Kriging metamodeling in simulation: A review. *European Journal of Operational Research*, 192(3), 707-716.
- KREEMER, C., J. HAINES, et al., 2000. On the determination of a global strain rate model. *Earth Planets Space*, 52, 765-770.
- KRIGE, D. G., 1951. *A statistical approach to some mine valuation and allied problems on the Witwatersrand*. Master's thesis, University of the Witwatersrand, South Africa.
- LANDI, P., R. A. CORSARO, et al., 2009. Magma dynamics during the 2007 Stromboli eruption (Aeolian Islands, Italy): Mineralogical, geochemical and isotopic data. *Journal of Volcanology*

- and *Geothermal Research*, 182(3-4), 255-268.
- LEE, D., J. R. BARBER, et al., 2009. Indentation of an elastic half space with material properties varying with depth. *Int. J. Eng. Sci.*, 47(11), 1274-1283.
- LIU, Z., D. DONG, et al., 2010. Monitoring time-dependent volcanic dynamics at Long Valley Caldera using InSAR and GPS measurements. *Geoscience and Remote Sensing Symposium (IGARSS)*, 2010 IEEE International, 665-668.
- LUNDGREN, P. and Z. LU, 2006. Inflation model of Uzon caldera, Kamchatka, constrained by satellite radar interferometry observations. *Geophys. Res. Lett.*, 33(6), L06301.
- LUNGARINI, L., C. TROISE, et al., 2005. Finite element modeling of topographic effects on elastic ground deformation at Mt. Etna. *Journal of Volcanology and Geothermal Research*, 144(1-4), 257-271.
- MANCONI, A., M.-A. LONGPRÉ, et al., 2009. The effects of flank collapses on volcano plumbing systems. *Geology*, 37(12), 1099-1102.
- MANCONI, A., T. R. WALTER, et al., 2007. Effects of mechanical layering on volcano deformation. *Geophysical Journal International*, 170(2), 952-958.
- MANCONI, A., T. R. WALTER, et al., 2010. On the effects of 3-D mechanical heterogeneities at Campi Flegrei caldera, southern Italy. *Journal of Geophysical Research*, 115, B08405.
- MANI, S. S., B. G. van BLOEMEN WAANDERS, et al., 2006. *Analysis of real-time reservoir monitoring : reservoirs, strategies, & modeling*, Medium: ED, Size: 84 p.
- MARCHETTI, E., R. GENCO, et al., 2009. Ground deformation and seismicity related to the propagation and drainage of the dyke feeding system during the 2007 effusive eruption at Stromboli volcano (Italy). *Journal of Volcanology and Geothermal Research*, 182(3-4), 155-161.
- MASSONNET, D. and K. L. FEIGL, 1998. Radar interferometry and its application to changes in the Earth's surface, *Rev. Geophys.*, 36(4), 441-500.
- MASSONNET, D., M. Rossi, et al., 1993. The displacement field of the Landers earthquake mapped by radar interferometry. *Nature*, 364, 138-142.
- MASTERLARK, T., K. L. FEIGL, et al., 2012. Nonlinear estimation of geometric parameters in FEMs of volcano deformation: Integrating tomography models and geodetic data for Okmok volcano, Alaska. *Journal of Geophysical Research*, 117, B02407.
- MATTIA, M., M. ALOISI, et al., 2008. Geophysical investigations of the plumbing system of Stromboli volcano (Aeolian Islands, Italy). *Journal of Volcanology and Geothermal Research*, 176(4), 529-540.
- MCKAY, M. D., R. J. BECKMAN, et al., 1979. A comparison of three methods for selecting values of input variables in the analysis of output from a computer code, *Technometrics*, vol. 21, No. 2., 239-245.
- MCTIGUE, D. F., 1987. Elastic stress and deformation near a finite spherical magma body: Resolution of the point source paradox. *J. Geophys. Res.*, 92, 12931-12940.

- MENKE, W., 1989. *Geophysical data analysis: discrete inverse theory*, Academic Press.
- MICHALEWICZ, Z., 1992. *Genetic algorithms + data structures = evolution programs*, Springer-Verlag.
- MISITI, V., F. VETERE, et al., 2009. Viscosity of high-K basalt from the 5th April 2003 Stromboli paroxysmal explosion. *Chemical Geology*, 260(3-4), 278-285.
- MOGI, K., 1958. Relations between the Eruptions of Various Volcanoes and the Deformations of the Ground Surfaces around them. *BULLETIN OF THE EARTHQUAKE RESEARCH INSTITUTE* Vol. 36, pp. 99-134.
- MORAN, S. C., O. KWOUN, et al., 2006. On the absence of InSAR-detected volcano deformation spanning the 1995-1996 and 1999 eruptions of Shishaldin Volcano, Alaska. *Journal of Volcanology and Geothermal Research*, 150(1-3), 119-131.
- MORRIS, M. D. and T. J. MITCHELL, 1995. Exploratory designs for computational experiments, *Journal of Statistical Planning and Inference*, 43(3), 381-402.
- MOTAGH, M., Y. DJAMOUR, et al., 2007. Land subsidence in Mashhad Valley, northeast Iran: results from InSAR, levelling and GPS. *Geophysical Journal International*, 168(2), 518-526.
- MOTAGH, M., T. R. WALTER, et al., 2008. Land subsidence in Iran caused by widespread water reservoir overexploitation. *Geophys. Res. Lett.* 35.
- MURASE, M., K. ONO, et al., 2007. Time-dependent model for volume changes in pressure sources at Asama volcano, central Japan due to vertical deformations detected by precise leveling during 1902-2005. *Journal of Volcanology and Geothermal Research*, 164(1-2), 54-75.
- MYERS, R.H., KHURI, A.I. et al., 1989. Response surface methodology: 1966-1988, *Technometrics*, 31(2), 137-157.
- NERI, M. and G. LANZAFAME, 2009. Structural features of the 2007 Stromboli eruption. *Journal of Volcanology and Geothermal Research*, 182(3-4), 137-144.
- NEWMAN, A. V., T. H. DIXON, et al., 2006. A four-dimensional viscoelastic deformation model for Long Valley Caldera, California, between 1995 and 2000. *Journal of Volcanology and Geothermal Research*, 150(1-3), 244-269.
- NUNNARI, G., L. BERTUCCO, et al., 2001. A neural approach to the integrated inversion of geophysical data of different types. *Geoscience and Remote Sensing, IEEE Transactions on* 39(4), 736-748.
- NUNNARI, G., G. PUGLISI, et al., 2006. Modeling ground deformations in volcanic areas by using SAR interferograms. *Quaderni di Geofisica*, 43.
- OBRIZZO, F., F. PINGUE, et al., 2004. Bayesian inversion of 1994-1998 vertical displacements at Mt Etna: evidence for magma intrusion. *Geophysical Journal International*, 157(11), 935-946.
- OKADA, Y., 1985. Surface deformation due to shear and tensile faults in a half-space. *BULLETIN OF THE SEISMOLOGICAL SOCIETY OF AMERICA*, 75(4), 1135-1154.

- OKADA, Y., 1992. Internal deformation due to shear and tensile faults in a half-space. *BULLETIN OF THE SEISMOLOGICAL SOCIETY OF AMERICA*, 82(2), 1018-1040.
- PALANO, M., G. PUGLISI, et al., 2008. Ground deformation patterns at Mt. Etna from 1993 to 2000 from joint use of InSAR and GPS techniques. *Journal of Volcanology and Geothermal Research*, 169(3-4), 99-120.
- PANICAUD, B., J. L. GROSSEAU-POUSSARD, et al., 2006. On the growth strain origin and stress evolution prediction during oxidation of metals. *Applied Surface Science*, 252(16), 5700-5713.
- PARK, J.-S., 1994. Optimal Latin-hypercube designs for computer experiments, *Journal of Statistical Planning and Inference*, 39, 95-111.
- PARK, J.-S. and J. JEON, 2002. Estimation of input parameters in complex simulation using a Gaussian process metamodel. *Probabilistic Engineering Mechanics*, 17(3), 219-225.
- PARKER, R. L., 1994. *Geophysical Inverse Theory*, Princeton University Press.
- PARSOPOULOS, K. E. and M. N. VRAHATIS, 2002. Recent approaches to global optimization problems through Particle Swarm Optimization, *Natural Computing*, 1, 235-306.
- PRESS, F. and R. SIEVER. 1994. *Understanding Earth*, W.H. Freeman and Company.
- POLAND, M., M. HAMBURGER, et al., 2006. The changing shapes of active volcanoes: History, evolution, and future challenges for volcano geodesy. *Journal of Volcanology and Geothermal Research*, 150, 1-13.
- PUGLISI, G., A. BONACCORSO, et al., 2005. New integrated geodetic monitoring system at Stromboli volcano (Italy). *Engineering Geology*, 79(1-2), 13-31.
- REGIS, R. G. and C. A. SHOEMAKER, 2005. Constrained global optimization of expensive black box functions using radial basis functions. *Journal of Global Optimization*, 31(1), 153-171.
- RIP, M. R. and J. M. HASIK, 2002. *The Precision Revolution: GPS and the Future of Aerial Warfare*. Naval Institute Press.
- ROSI, M., A. BERTAGNINI, et al., 2006. A case history of paroxysmal explosion at Stromboli: Timing and dynamics of the April 5, 2003 event. *Earth and Planetary Science Letters*, 243(3-4), 594-606.
- ROY, M., 1998. Evolution of fault systems at a strike-slip plate boundary: A viscoelastic model. *Geophysical Research Letters*, 25(15), 2881-2884.
- RUCH, J., J. ANDERSSOHN, et al., 2008. Caldera-scale inflation of the Lazufre volcanic area, South America: Evidence from InSAR. *Journal of Volcanology and Geothermal Research*, 174(4), 337-344.
- RUCH, J. and T. R. WALTER, 2010. Relationship between the InSAR-measured uplift, the structural framework, and the present-day stress field at Lazufre volcanic area, central Andes. *Tectonophysics*, 492, 133-140.
- SACKS, J., S. B. SCHILLER, et al., 1989. Designs for computer experiments, *Technometrics*, 31(1),



- 41-47.
- SACKS J., W. J. WELCH, et al., 1989. Design and analysis of computer experiments. *Statistical Science*, 4(4), 409–435.
- SAINATO, C. M. and M. C. POMPOSIELLO, 1997. Two-dimensional magnetotelluric and gravity models of the Tuzgle volcano zone (Jujuy province, Argentina). *Journal of South American Earth Sciences*, 10(3-4), 247-261.
- SASENA, M. J., P. PAPALAMBROS, et al., 2002. Exploration of metamodeling sampling criteria for constrained global optimization. *Engineering Optimization*, 34(3), 263-278.
- SCALES, J. A., M. L. SMITH, et al., 2001. *Introductory Geophysical Inverse Theory*. Samizdat Press.
- SCANDURA, D., G. CURRENTI, et al., 2008. Finite Element Models of Elasto-Plastic Deformation in Volcanic Areas. *COMSOL Conference 2008 Hannover*, Hannover.
- SCHONLAU, M., 1997. *Computer Experiments and Global Optimization*. PhD thesis, University of Waterloo, CA.
- SCHULTZ, R. A., 1995. Limits on Strength and Deformation Properties of Jointed Basaltic Rock Masses. *Rock Mechanics and Rock Engineering*, 28(1), 1-15.
- SECCIA, D., C. CHIARABBA, et al., 2011. Evidence for the contemporary magmatic system beneath Long Valley Caldera from local earthquake tomography and receiver function analysis. *J. Geophys. Res.*, 116, B12314.
- SEGALL, P., 2010. *Earthquake and Volcano Deformation*, Princeton University Press.
- SHEWRY, M. C. and H. P. WYNN, 1987. Maximum entropy sampling, *Journal of Applied Statistics*, 14(2), 165-170.
- SIMPSON, T. W., J. D. PEPLINSKI, et al., 2001. Metamodels for Computer-based Engineering Design: Survey and recommendations. *Engineering with Computers*, 17, 129-150.
- STRATTON, J. A., 1941. *Electromagnetic theory*, McGraw-Hill Book Company, New York and London.
- TAGUCHI, G., Y. YOKOYAMA, et al., 1993. *Taguchi methods: Design of experiments*, American Supplier Institute, Allen Park, Michigan.
- TANG, B., 1993. Orthogonal array-based Latin hypercubes, *Journal of the American Statistical Association*, 88(424), 1392-1397.
- TARANTOLA, A., 2005. *Inverse Problem Theory and Methods for Model Parameter Estimation*, Society for Industrial and Applied Mathematics.
- TIAMPO, K. F., J. B. RUNDLE, et al., 2000. Spherical and ellipsoidal volcanic sources at Long Valley caldera, California, using a genetic algorithm inversion technique. *Journal of Volcanology and Geothermal Research*, 102(3-4), 189-206.
- TOROPOV, V. V., S. J. BATES, et al., 2007. Generation of extended uniform Latin hypercube designs of experiments, *Proceedings of the Ninth International Conference on the Application of*

- Artificial Intelligence to Civil, Structural and Environmental Engineering*, Civil-Comp Press.
- TRASATTI, E., C. GIUNCHI, et al., 2003. Effects of topography and rheological layering on ground deformation in volcanic regions. *Journal of Volcanology and Geothermal Research*, 122(1-2), 89-110.
- UKAWA, M., 1993. Excitation mechanism of large-amplitude volcanic tremor associated with the 1989 Ito-oki submarine eruption, central Japan. *Journal of Volcanology and Geothermal Research*, 55(1-2), 33-50.
- UNAL, R., R. A. LEPSCH et al., 1998. Response surface model building and multidisciplinary optimization using D-optimal designs, *AIAA-98-4759*.
- WANG, G. G., 2003. Adaptive response surface method using inherited Latin hypercube design points, *Transactions of the ASME, Journal of Mechanical Design*, 125, 210-220.
- WALZER, U., R. HENDEL, et al., 2003. Viscosity Stratification and a 3-D Compressible Spherical Shell Model of Mantle Evolution. *High Performance Computing in Science and Engineering '03*. E. Krause, W. Jäger and M. Resch, Springer Berlin Heidelberg, 27-67.
- WASSERMANN, J., 1997. Locating the sources of volcanic explosions and volcanic tremor at Stromboli volcano (Italy) using beam-forming on diffraction hyperboloids. *Physics of the Earth and Planetary Interiors*, 104(1-3), 271-281.
- WHITE, N., 1994. An inverse method for determining lithospheric strain rate variation on geological timescales. *Earth and Planetary Science Letters*, 122(3-4), 351-371.
- WILLIAMS, C. A. and G. WADGE, 1998. The Effects of Topography on Magma Chamber Deformation Models: Application to Mt. Etna and Radar Interferometry. *Geophys. Res. Lett.*, 25, 1549-1552.
- WILLIAMS, C. A. and G. WADGE, 2000. An accurate and efficient method for including the effects of topography in three-dimensional elastic models of ground deformation with applications to radar interferometry. *J. Geophys. Res.*, 105, 8103-8120.
- YAMAJI, A., 2000. The multiple inverse method: a new technique to separate stresses from heterogeneous fault-slip data. *Journal of Structural Geology*, 22(4), 441-452.
- YANG, B., 2009. *Modified Particle Swarm Optimizers and their Application to Robust Design and Structural Optimization*. Lehrstuhl für Statik. Munich, Technische Universität München
- YANG, X.-M., P. M. DAVIS, et al., 1988. Deformation from Inflation of a Dipping Finite Prolate Spheroid in an Elastic Half-Space as a Model for Volcanic Stressing. *J. Geophys. Res.*, 93(B5), 4249-4257.
- YE, K. Q., W. LI, et al., 2000. Algorithmic construction of optimal symmetric Latin hypercube designs, *Journal of Statistical Planning and Inference*, 90, 145-159.
- ZHANG, H., X. CONG, et al., 2010. An integrated approach to determine parameters of a 3D volcano model by using InSAR data with metamodel technique. *Geoscience and Remote Sensing*

*Symposium (IGARSS)*, 2010 IEEE International, 1648-1651.

ZHDANOV, M. S., 2002. *Geophysical Inverse Theory and Regularization Problems*, Elsevier.

ZHU, X. and R. BAMLER, 2011. Let's Do the Time Warp: Multicomponent Nonlinear Motion Estimation in Differential SAR Tomography. *IEEE Geoscience and Remote Sensing Letters*, 8(4), 735-739.

ZUPANSKI, D. and M. ZUPANSKI, 2005. *MODEL ERROR ESTIMATION EMPLOYING ENSEMBLE DATA ASSIMILATION APPROACH*: 53.



## Acknowledgements

I thank Prof. Dr.-Ing. Kai-Uwe Bletzinger for his excellent mentoring. He encouraged my research work and gave me much appreciated freedom in research. Although he was very busy, he always managed to discuss emerging research questions and read drafts.

Hereby I would also like to express my sincere thanks to Prof. Rocco Malservisi for reviewing this thesis and acting as co-supervisor. He helped me quite a lot to broaden my knowledge in Geophysics and improve my English skills both in speaking and in writing.

At the beginning of my research work, Prof. Dr. Anke M. Friedrich was one of my first contact persons for any problems related to geoscience. She and her warm-hearted colleagues gave me many valuable advices.

Prof. Dr. Timothy Dixon from School of Geosciences at University of South Florida shared his research experiences and gave me a lot of invaluable suggestions and comments during my aboard stay, which had much influence on my research.

Many thanks to my colleagues and dear friends Dr.-Ing. Hongchao Fan, Dr.-Ing. Weiyong Yi, Dr.-Ing. Wei Yao and Dr.-Ing. Lu Liu, with whom I had over hundreds discussions about my research. Their open minds and professional advices help me a lot in my research.

For the most part, my dissertation presents results of the project “Dynamic Earth”, which was funded by the International Graduate School of Science and Engineering (IGSSE). I admiringly acknowledge this support.

I am truly grateful to work at the chair of structural analysis of Technische Universität München and do enjoy being a member of the research team “Dynamic Earth”. Many thanks to Prof. Dr.-Ing. Richard Bamler, Prof. Dr. Michael Eineder, Prof. Dr.-Ing. Xiaoxiang Zhu and Dr.-Ing. Xiaoying Cong for their supports and collaborations. Thanks all the colleagues of the chair for always offering a friendly and inspiring atmosphere in the department.

Last but not least, I would like to thank my wife and soulmate Zheng Mei for her endless support and understanding. Besides, I also want to thank my parents for their encouragement and always being supportive. This dissertation is dedicated to my family that has constantly supported me.



# Curriculum Vitae

## Fundamental Information

Name: Hao ZHANG  
Nationality: P.R. China  
Date of Birth: 29 December 1982  
Place of Birth: Beijing, P.R. China

## Education

1989/09-1995/07 Huang Cheng Gen elementary school, Beijing  
1995/09-1998/07 Beijing No. 39 middle school, Beijing  
1998/09-2001/07 Beijing No. 4 high school, Beijing  
2001/09-2005/07 Automotive Engineering at Tsinghua University, Beijing  
(Bachelor of Engineering)  
2005/10-2008/03 Computational Mechanics at Technische Universität München  
(Master of Science). Master thesis: Successive Latin Hypercube  
Designs for Global Metamodeling Techniques.  
2008/06-2012/07 PhD student at the chair of structural analysis, Technische Uni-  
versität München

## Experiences

2008/06-2012/07 Scientific assistant at the chair of structural analysis, Technische  
Universität München  
2012/08- Validation engineer at Schaeffler Technologies AG & Co. KG

## Scholar exchange

2011/03-2011/06 School of Geosciences at University of South Florida, USA